



저작자표시-비영리-변경금지 2.0 대한민국

이용자는 아래의 조건을 따르는 경우에 한하여 자유롭게

- 이 저작물을 복제, 배포, 전송, 전시, 공연 및 방송할 수 있습니다.

다음과 같은 조건을 따라야 합니다:



저작자표시. 귀하는 원저작자를 표시하여야 합니다.



비영리. 귀하는 이 저작물을 영리 목적으로 이용할 수 없습니다.



변경금지. 귀하는 이 저작물을 개작, 변형 또는 가공할 수 없습니다.

- 귀하는, 이 저작물의 재이용이나 배포의 경우, 이 저작물에 적용된 이용허락조건을 명확하게 나타내어야 합니다.
- 저작권자로부터 별도의 허가를 받으면 이러한 조건들은 적용되지 않습니다.

저작권법에 따른 이용자의 권리는 위의 내용에 의하여 영향을 받지 않습니다.

이것은 [이용허락규약\(Legal Code\)](#)을 이해하기 쉽게 요약한 것입니다.

[Disclaimer](#)

**INVESTIGATION OF SURFACE DAMAGE  
AND FRICTION CHARACTERISTICS  
OF 2D MATERIALS**

Bien-Cuong Tran Khac

The Graduate School  
University of Ulsan  
School of Mechanical Engineering

**INVESTIGATION OF SURFACE DAMAGE  
AND FRICTION CHARACTERISTICS  
OF 2D MATERIALS**

Supervisor: Prof. Koo-Hyun Chung

A Dissertation

Submitted to

the Graduate School of the University of Ulsan

In partial Fulfillment of the Requirements

for the Degree of

Doctor of Philosophy

by

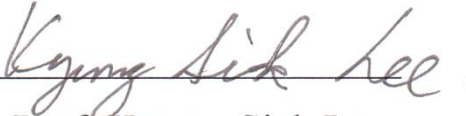
Bien-Cuong Tran Khac

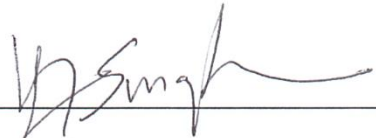
School of Mechanical Engineering


Ulsan, Korea


November 2017


This certifies that the dissertation of  
Bien-Cuong Tran Khac is approved

  
\_\_\_\_\_  
Thesis committee Chairman : Prof. Kyung-Sick Lee

  
\_\_\_\_\_  
Thesis Committee Member : Prof. Sung-Tae Hong

  
\_\_\_\_\_  
Thesis Committee Member : Prof. Koo-Hyun Chung

  
\_\_\_\_\_  
Thesis Committee Member : Prof. Doo-Man Chun

  
\_\_\_\_\_  
Thesis Committee Member : Prof. Hyun-Joon Kim

The Graduate School  
University of Ulsan  
November 2017

# TABLE OF CONTENTS

<b>TABLE OF CONTENTS .....</b>	<b>i</b>
<b>LIST OF TABLES .....</b>	<b>iii</b>
<b>LIST OF FIGURES .....</b>	<b>iv</b>
<b>ABSTRACT.....</b>	<b>xvii</b>
<b>Chapter 1</b>	
<b>Introduction.....</b>	<b>1</b>
1.1 Background and Motivation .....	1
1.2 Objectives of the Research.....	4
1.3 Organization of the Research .....	4
<b>Chapter 2</b>	
<b>Tribology of 2D materials: Literature review .....</b>	<b>7</b>
2.1 Synthesis of 2D materials.....	8
2.1 Wear resistance and surface damage characteristics of 2D materials.....	10
2.2 Friction force characteristics of 2D materials .....	19
<b>Chapter 3</b>	
<b>Surface damage characteristic of 2D materials.....</b>	<b>27</b>
3.1 Experimental section.....	28
3.2 Thickness determination of 2D materials.....	30
3.3 Adhesion strength to substrate of single-layer materials .....	34
3.4 Surface damage characteristic of single-layer material.....	38
3.4.1 Surface damage characteristics of single-layer h-BN.....	38
3.4.2 Surface damage characteristics of single-layer MoS <sub>2</sub> .....	42
3.4.3 Surface damage characteristics of single-layer graphene.....	49

3.5 Effect of number of layers on surface damage characteristics .....	57
3.5.1 Adhesion strength to the substrate of multi-layer .....	58
3.5.2 Surface damage characteristics of multi-layer .....	67
3.5.3 Frictional behaviors during scratch tests. ....	68
3.6 Summary .....	71
<b>Chapter 4</b>	
<b>Friction characteristic of 2D materials .....</b>	<b>73</b>
4.1 Experimental section .....	74
4.2 Thickness characterization of single-layer materials .....	76
4.3 Effect of test conditions: normal force and sliding speed .....	78
4.3.1 Effect of topography .....	78
4.3.2 Effect of normal force .....	90
4.3.3 Effect of sliding speed .....	96
4.4 Effect of environmental conditions .....	101
4.4.1 Effect of relative humidity .....	101
4.4.2 Effect of thermal annealing .....	108
4.4.3 Effect of temperature .....	110
4.5 Summary .....	111
<b>Chapter 5</b>	
<b>Conclusions and Recommendations .....</b>	<b>114</b>
5.1 Conclusions of the Research .....	114
5.2 Recommendations for future work .....	119
<b>References .....</b>	<b>121</b>

## LIST OF TABLES

Table 2.1. Summary of mechanical properties of layered materials h-BN, MoS <sub>2</sub> , and graphene .....	11
--------------------------------------------------------------------------------------------------------------	----

## LIST OF FIGURES

Fig. 1.1 Schematic structure of atomically thin (a) h-BN, <sup>1</sup> (b) MoS <sub>2</sub> , <sup>3</sup> and (c) graphene. <sup>2</sup> .....	1
Fig. 1.2 Objective and scope of this research .....	6
Fig. 2.1. (a) Schematic image and microstructural evidence of the toughening mechanisms in the ceramic matrix including (b) nanoplatelet pull-out, (c) crack branching, (d) crack bridging, and (e) crack blunting. <sup>56</sup> .....	12
Fig. 2.2. Topographic images of SiO <sub>2</sub> substrate and multilayer graphene (~ 4.5 nm thickness) after scratch tests under various normal forces. Normal forces were noted in the images. <sup>69</sup> .....	13
Fig. 2.3. (a) Coefficient of friction and (b) wear rate for steel against steel sliding tribo-pairs in absence of graphene and in presence of single layer and few-layer graphene in hydrogen environment. <sup>75</sup> .....	14
Fig. 2.4. Normal force and lateral force with respect to time on single layer (a and b) and bilayer (c) graphene. (d) Normal displacement of probe versus time of the sample in (c). All the scratched specimens were exfoliated and pristine graphene. <sup>70</sup> .....	15
Fig. 2.5. 3D topographic AFM images of atomically thin graphene obtained using contact mode under increasing normal force: (a) 10 nN, (b) 195 nN, and (c) 391 nN. (d) cross-sectional height profiles taken from the images in (a), (b), and (c) demonstrating the negative strain of atomically thin graphene (expansion upon shear and compression). (e) Schematic illustrating the dynamic wrinkling mechanism of atomically thin materials. <sup>77</sup> .....	16
Fig. 2.6. Scratching graphene with (a-c) line scratching and (d-f) areas scratching. (a and d) Topographic and (b and e) phase images of scratches areas. (c and f) Cross-sectional height profiles obtained from the corresponding topographic images. In panel a, the normal force was gradually increased from 1.41 mN to 17.48 mN (line 1 <sup>st</sup> to line 12 <sup>th</sup> ) and in panel d, the normal	



force was gradually increased from 1.41 mN to 11.45 mN (area 1<sup>st</sup> to area 6<sup>th</sup>), with respect to the increasing noted number.<sup>69</sup> ..... 17

Fig. 2.7. Scratching single-layer graphene with (a-c) amorphous and (d-f) smooth tips. At low normal forces the Pt substrates deform elastically, the lateral forces  $F_L$  are low and show clearly visible stick–slip (a, d). When the substrates deform plastically under the intact graphene layer, the lateral forces increase and the stick–slip pattern disappears (c, e). Single-layer graphene rupture causes strong plastic deformation and formation of wear tracks (d, f).<sup>79</sup> ..... 18

Fig. 2.8. (a) Friction loop and (b) load-dependent friction of the bare Cu substrate and single-layer h-BN growth on Cu.<sup>80</sup> (c) Friction force variation of mechanical exfoliated single-layer MoS<sub>2</sub> and graphene with respect to normal force.<sup>81</sup> (d) Friction force variation of thermal decomposition single- and bi-layer graphene with respect to normal force.<sup>16</sup> In panel a, the normal force was 40 nN. In panel a and c, friction force measurements were conducted in ambient condition using Si tip. In panel d, friction force was obtained in ultra-high vacuum environment..... 20

Fig. 2.9. (a) Thickness-dependent friction of atomically thin graphene, MoS<sub>2</sub>, NbSe<sub>2</sub>, and h-BN obtained using FFM measurements. (b) Schematic illustrating the puckering effect, in which the adhesion to the sliding AFM tip induced out-of-plane deformation of atomically thin graphene, resulting in the increased contact area and friction. (c) Thickness-dependent friction of atomically thin materials using FEM simulation. In panel a, the out-of-plane deformation was indicated by the color scale. In panel a and c, friction force was normalized by the value obtained for single-layer materials. The inset in c depicted the local out-of-plane deformation of the atomically thin materials around the contact areas for sliding over a single-layer and four-layer material.<sup>83</sup> ..... 22

Fig. 2.10. (a) Topographic and FFM images of single-layer graphene on SiO<sub>2</sub> substrate along with friction loop. Schematic illustrating the (b) three ripple domains, (c) the relative angle between the ripple lines and scan direction, and (d) the puckering effect during the tip scanning across the surface of graphene under low and high normal force. In panel b, the forward scan direction was indicated by the red dashed arrow, and the back dashed line indicates the location where the friction loop was taken.<sup>88</sup> ..... 23

Fig. 2.11. (a) Topographic and (b) FFM images of single- and bi-layer MoS<sub>2</sub> obtained by intermittent contact and contact mode, respectively, after laser treatment with 1 mW, 5 mW, and 10 mW for 60 s. The red dashed lines indicate the locations where the cross-sectional height profiles and friction loop were taken.<sup>89</sup> ..... 24

Fig. 2.12. Plot of (a) normal force-dependent friction force and (b) representative friction loops of fluorinated single-layer graphene and pristine single-layer graphene. (c) Schematic illustrating FFM measurements with the out-of-plane bending deformation. (d) Representative friction loops obtained from graphene, hydrogenated graphene, oxidized graphene, and SiO<sub>2</sub> substrate.<sup>90,95</sup> ..... 25

Fig. 2.13. The Green-Kubo estimate of friction coefficients of liquid water on (a) MoS<sub>2</sub>, and (b) graphene and h-BN. The friction coefficients  $\lambda$  was obtained by the plateau value for long time. The shaded areas represent the error bars. The inset in panel a is the time-dependency of force correlation function and the fit of solid line indicates an exponential decay.<sup>100,101</sup> ..... 26

Fig. 3.1. (a) Optical microscopy images and (b) AFM topographic images of single- and a few layer h-BN, MoS<sub>2</sub>, and graphene. The topographic images were obtained from the intermittent contact mode of AFM. In panel b, the cross-sectional profiles are included and the red dashed lines indicate the location where the cross-sectional profile are taken. .... 31

Fig. 3.2. Variation of (a) thickness and (b) surface roughness of atomically thin h-BN, MoS<sub>2</sub> and graphene with respect to number of layers. Error bar represents one standard deviation..... 32

Fig. 3.3. Raman spectra of single- and a few layer h-BN, MoS<sub>2</sub>, and graphene. Frequency of the characteristic peak of single layer h-BN, MoS<sub>2</sub>, and graphene are denoted as dashed lines for comparison. Raman 2D peaks of graphene were fitted using Lorentzian function. .... 33

Fig. 3.4. Progressive force scratch test results of single-layer (from left to right) h-BN, MoS<sub>2</sub>, and graphene. (a) Lateral force variation with respect to normal force during progressive force scratch tests. The normal force was progressively increased from 400 nN to 4000 nN with a scratch distance of 2 μm. (b) FFM images (forward scans), and (c) topographic images of scratch tracks from single-layer h-BN, MoS<sub>2</sub> and graphene after progressive force scratch tests. Critical force of single-layer materials were determined by the abruptly change in lateral force during scratch test, where the failure of these single-layer materials occurred and the substrate was exposed. .... 36

Fig. 3.5. High resolution (a) topographic and (b) FFM (forward scan) images of single layer h-BN after a constant force scratch test under 500 nN; 800 nN; 1,200 nN; and 1,500 nN normal force. Single-layer h-BN was scratched under a constant normal force at area of 1 μm × 1 μm as indicated by white dashed square in panel a and b. The cross-sectional profiles and friction loops are included in panel a and b, which demonstrate the change in friction and topography of single layer h-BN due to the constant force scratch test..... 40

Fig. 3.6. (a) Topographic image, (b) FFM image (forward scan), and (c) Raman mapping image with the G peak intensity of single layer h-BN after a constant force scratch test under various normal force ranging from 500 nN to 1200 nN. (d) Raman spectra and (e) summary of frequency of G peak of scratched single-layer h-BN with respect to normal force. Single-layer h-BN was

scratched under a constant normal force at the area of  $1\ \mu\text{m} \times 1\ \mu\text{m}$  as indicated by white dashed square in panel a. The Raman spectra were fitted using Lorentzian function and the frequency of G peak from as-exfoliated single-layer h-BN are also denoted as dashed lines for comparison in the panel d and e. Error bar represents one standard deviation..... 42

Fig. 3.7. High resolution (a) topographic and (b) FFM (forward scan) images of single layer MoS<sub>2</sub> after a constant force scratch test under 1,000 nN, 1,500 nN, 2,000 nN, and 2,500 nN normal force. Single-layer MoS<sub>2</sub> was scratched under a constant normal force at the area of  $1\ \mu\text{m} \times 1\ \mu\text{m}$  as indicated by white dashed square in panel a and b. Cross-sectional height profiles and friction loops are included in panel a and b, which demonstrate the change in friction and topography of single layer MoS<sub>2</sub> due to the constant force scratch test. .... 44

Fig. 3.8. (a) Topographic image, (b) FFM image (forward scan), and Raman mapping images with (c)  $E_{2g}^1$  and (d)  $A_{1g}$  peaks intensity of single layer MoS<sub>2</sub> after a constant force scratch test under 2,000 nN normal force. (e) Raman spectra, and summary of (f) intensity, and (g) frequency of  $E_{2g}^1$  and  $A_{1g}$  peaks of scratched single-layer MoS<sub>2</sub> with respect to normal force. Single-layer MoS<sub>2</sub> was scratched under a constant normal force at the area of  $1\ \mu\text{m} \times 1\ \mu\text{m}$  as indicated by white dashed square in panel a. Raman spectra were fitted using Gaussian function. In panel e, f, and g, the frequency and intensity of the  $E_{2g}^1$  and  $A_{1g}$  peaks from the as-exfoliated single layer MoS<sub>2</sub> are also denoted as dashed lines for comparison. Error bar represents one standard deviation. .... 46

Fig. 3.9. The Raman  $E_{2g}^1$  peak FWHM of scratched single-layer MoS<sub>2</sub> with respect to normal force. The  $E_{2g}^1$  peak FWHM from the as-exfoliated single layer MoS<sub>2</sub> is denoted as dashed lines for comparison. Error bar represents one standard. .... 47

Fig. 3.10. (a) Photoluminescence (PL) intensity image of single layer MoS<sub>2</sub> after constant force scratch test under 2,000 nN normal force. (b) PL spectra of scratched single-layer MoS<sub>2</sub> with respect to normal force. In panel b, the energy of the A exciton of as-exfoliated single layer MoS<sub>2</sub> was noted as dashed line for comparison. .... 49

Fig. 3.11. High resolution (a) topographic and (b) FFM (forward scan) images of single layer graphene after a constant force scratch test under (from left to right) 1,000 nN, 3,000 nN, 4,000 nN, and 5,000 nN normal force. Single-layer graphene was scratched under a constant normal force at the area of 1 μm × 1 μm as indicated by white dashed square in panel a and b. Cross-sectional height profile and friction loop are included in panel a and b, which demonstrate the change in friction and topography of single-layer graphene due to the constant force scratch test. .... 50

Fig. 3.12. Topographic image, FFM image (forward scan), and Raman mapping images with the D and 2D peaks intensity of single layer graphene after a constant force scratch test under various normal force ranging (a) from 800 nN to 2,400 nN and (b) from 3,000 nN to 5,000 nN. Single-layer graphene were scratched under a constant normal force at the area of 1 μm × 1 μm as indicated by white dashed square in panel a and b. .... 52

Fig. 3.13. (a) Raman spectra, and summary of (a) frequency and (c) intensity of G, and 2D peaks of scratched single-layer graphene with respect with respect to normal force. The Raman spectra in panel a were fitted using Lorentzian function. The frequency and the intensity of the D, G and 2D peaks from the as-exfoliated single layer graphene are also denoted as dashed lines for comparison in the panel a, b, and c. Error bar represents one standard deviation. .... 54

Fig. 3.14. Schematic illustrating the buckling region in front of the sliding AFM tip from (a) side view and (b) plane view during scratch test. .... 57

Fig. 3.15. Progressive force scratch test results of bi-, tri-, and multi-layer h-BN. (a) Lateral force variation with respect to normal force during progressive force scratch tests. (b) FFM images (forward scans), and (c) topographic images of scratch tracks after progressive force scratch tests. High resolution (d) FFM images (forward scans) and (e) topographic images of scratch tracks formed at single- and multi-layer h-BN after progressive force scratch tests. In panel b, the scratch distance of about 2  $\mu\text{m}$  was also noted. In panel b and c, scale bars: 500 nm. Friction loops and cross-sectional profiles are included in panel d and e, respectively. Red dashed lines indicate the location and the corresponding normal force during scratch test, where friction loops and cross-sectional profile are taken. .... 60

Fig. 3.16. Progressive force scratch test results of bi-, tri-, and multi-layer MoS<sub>2</sub>. (a) Lateral force variation with respect to normal force during progressive force scratch tests. (b) FFM images (forward scans), and (c) topographic images of scratch tracks after progressive force scratch tests. High resolution (d) FFM images (forward scans) and (e) topographic images of scratch tracks formed at single- and a multi-layer MoS<sub>2</sub> after progressive force scratch tests. In panel b, the scratch distance of about 2  $\mu\text{m}$  was also noted. In panel b and c, scale bars: 500 nm. Friction loops and cross-sectional profiles are included in panel d and e, respectively. Red dashed lines indicate the location and the corresponding normal force during scratch test, where friction loops and cross-sectional profile are taken. .... 61

Fig. 3.17. Progressive force scratch test results of bi-, tri-, and multi-layer graphene. (a) Lateral force variation with respect to normal force during progressive force scratch tests. (b) FFM images (forward scans), and (c) topographic images of scratch tracks after progressive force scratch tests. High resolution (d) FFM images (forward scans) and (e) topographic images of scratch tracks formed at single- and multi-layer graphene after progressive force scratch tests.

In panel b, the scratch distance of about 2  $\mu\text{m}$  was also noted. In panel b and c, scale bars: 500 nm. Friction loops and cross-sectional profiles are included in panel d and e, respectively. Red dashed lines indicate the location and the corresponding normal force during scratch test, where friction loops and cross-sectional profile are taken..... 63

Fig. 3.18. Variation of the (a) critical force,  $F_c$ , and (b) normal force that induced surface damages,  $F_d$ , of h-BN,  $\text{MoS}_2$ , and graphene with respect to number of layers. (c) Schematic of total van der Waals interactions between substrate and atomically thin films, which demonstrates that the total interactions between the atomically thin film and substrate gradually increased as the number of layers increased. The error bar in panel a and b represents one standard deviation. .... 66

Fig. 3.19. High resolution topographic and FFM (forward scan) images of tri-layer (a) h-BN, (b)  $\text{MoS}_2$ , and (c) graphene after a constant force scratch test under various normal force. The atomically thin materials were scratched under a constant normal force at the area of  $1 \mu\text{m} \times 1 \mu\text{m}$  as indicated by white dashed square. The cross-sectional height profile and friction loop are also included in the images ..... 67

Fig. 3.20. Variation of friction force of single- and a few-layer h-BN,  $\text{MoS}_2$ , and graphene during constant force scratch tests. The friction data was fitted by linear and exponential relationships with normal force. Error bar in panel a corresponds to one standard deviation. (b) AFM topographic images of tri- and multi-layer h-BN,  $\text{MoS}_2$ , and graphene after constant force scratch test. In panel b, the topographic images were obtained from the intermittent contact mode of AFM. Cross-sectional profiles are included and the red dashed lines indicate the location where the cross-sectional profile are taken. These atomically thin materials were

scratched under a constant normal force at the area of  $1 \mu\text{m} \times 1 \mu\text{m}$  as indicated by white dashed square in panel b..... 69

Fig. 4.1. (a) AFM topographic images and (b) Raman spectra of single-layer h-BN, MoS<sub>2</sub> and graphene. Topographic images were obtained from intermittent contact mode of AFM, the cross-sectional profiles are included in panels a. Red-dashed lines indicate the locations where the cross-sectional profiles are taken. In panels b, frequency of the characteristic Raman peaks of single-layer h-BN, MoS<sub>2</sub>, and graphene are denoted as dashed lines..... 77

Fig. 4.2. (a) Friction loops consisting of friction forces measured in both trace (forward scanning) and retrace (backward scanning) directions of single-layer h-BN, MoS<sub>2</sub>, and graphene, under 5 nN and 50 nN normal force. (b) Variation of friction force fluctuation in friction loop with respect to normal force..... 78

Fig. 4.3. (a) Topographic and (b) FFM images of single-layer h-BN obtained simultaneously from the contact mode of AFM under normal force of 20 nN and 50 nN. (c) Cross-sectional height profiles, (d) derivative cross-sectional height profile, (e) friction loops and (f) half subtracted friction are also included. The red dashed lines indicate the locations where the cross-sectional height profiles, height derivatives and friction loops were taken. .... 80

Fig. 4.4. (a) Topographic and (b) FFM images of single-layer MoS<sub>2</sub> obtained simultaneously from the contact mode of AFM under normal force of 20 nN and 50 nN. (c) Cross-sectional height profiles, (d) derivative cross-sectional height profile, (e) friction loops and (f) half subtracted friction are also included. The red dashed lines indicate the locations where the cross-sectional height profiles, height derivatives and friction loops were taken. .... 81

Fig. 4.5. (a) Topographic and (b) FFM images of single-layer graphene obtained simultaneously from the contact mode of AFM under normal force of 20 nN, and 50 nN. (c) Cross-sectional



height profiles, (d) derivative cross-sectional height, (e) friction loops and (f) half subtracted friction are also included. The red dashed lines indicate the locations where the cross-sectional height profiles, height derivatives and friction loops were taken. .... 82

Fig. 4.6. (a) Schematic diagram of the scanning (a) sharp tip and (b) flat-ended tip on surface of single-layer materials with these relevant force vectors. Due to the local slope of topography, normal force ( $F_N$ ) causes a component of the lateral force. In panel a and b, SEM images of the nano-crystalline diamond tips were also included. .... 84

Fig. 4.7. (a) Friction loops consisting of friction forces measured in both trace (forward scanning) and retrace (backward scanning) directions of single-layer h-BN, MoS<sub>2</sub>, and graphene, under - 100 nN and 50 nN normal force. Variation of friction fluctuation in friction loop with respect to normal force. The error bar corresponds to one standard deviation. .... 85

Fig. 4.8. (a) Topographic and (b) FFM images of single-layer h-BN obtained simultaneously from the contact mode of AFM under normal force of - 100 nN, - 50 nN, and 50 nN. (c) Cross-sectional height profiles, (d) derivative cross-sectional height profile and, (e) friction loops and (f) half subtracted friction are also included. Red dashed lines indicate the locations where cross-sectional height profiles, height derivatives and friction loops were taken..... 87

Fig. 4.9. (a) Topographic and (b) FFM images of single-layer MoS<sub>2</sub> obtained simultaneously from the contact mode of AFM under normal force of - 100 nN, - 50 nN, and 50 nN. (c) Cross-sectional height profiles, (d) derivative cross-sectional height profile and, (e) friction loops and (f) half subtracted friction are also included. Red dashed lines indicate the locations where cross-sectional height profiles, height derivatives and friction loops were taken..... 88

Fig. 4.10. (a) Topographic and (b) FFM images of single-layer graphene obtained simultaneously from the contact mode of AFM under normal force of - 100 nN, - 50 nN, and 50 nN. (c) Cross-

sectional height profiles, (d) derivative cross-sectional height profile, (e) friction loops and (f) half subtracted friction are also included. Red dashed lines indicate the locations where the cross-sectional height profiles, height derivatives and friction loops were taken..... 89

Fig. 4.11. (a) Variation of friction force as a function of normal force of single layer h-BN, MoS<sub>2</sub> and graphene. (b) Variation of adhesion force between tip and single-layer h-BN, MoS<sub>2</sub>, and graphene obtained before and after FFM measurements. In panel a, friction force data were fitted to Hertz-plus-offset (HPO) model using Eq. 4.1. The error bar corresponds to one standard deviation. .... 91

Fig. 4.12. (a) Variation of friction force as a function of normal force of single layer h-BN, MoS<sub>2</sub> and graphene obtained using flat-ended tip. (b) Variation of adhesion between tip and single-layer h-BN, MoS<sub>2</sub>, and graphene obtained before and after FFM measurements. The error bar corresponds to one standard deviation. .... 95

Fig. 4.13. (a) Variation of friction force as a function of sliding speed for single layer h-BN, MoS<sub>2</sub> and graphene under various normal forces. Friction force data was fitted to the thermally activated Prandtl-Tomlinson (PTT) model using Eq. 4.3. Error bar corresponds to one standard deviation. .... 96

Fig. 4.14. Plot of (a)  $\beta$ , (b)  $\beta_{\text{sin}}$ , (c)  $F_c$ , and  $E_0$  as a function of normal force.  $\beta$  is the parameter related to the shape of the lateral interaction potential that govern the rate of increase of friction with sliding speed at low speeds.  $F_c$  is friction force at 0 K.  $\beta$  and  $F_c$  are the results of fitting the sliding speed-dependent friction of single-layer h-BN, MoS<sub>2</sub>, and graphene to PTT model using Eq. 4.3. Assuming the lateral interaction potential exhibit a sinusoidal shape, in which the shape-related parameter  $\beta_{\text{sin}}$  and the corrugation amplitude of the interaction potential  $E_0$  are estimated using Eqs. 4.4 and 4.5, respectively..... 99

Fig. 4.15. Variation of friction as a function of (a) normal force and (b) sliding speed under different relative humidity (5% RH, 25% RH, 45% Rh and 75% RH) for single-layer h-BN, MoS<sub>2</sub> and graphene. In panel a, the sliding speed was set to 375 nm/s and the friction force data was fitted to HPO model using Eq. 4.1. In panel b, the normal force was set to 7 nN and friction force data were fitted to PTT model using Eq. 4.3. The error bar corresponds to one standard deviation. .... 102

Fig. 4.16. Variation of (a) interfacial shear strength, (b)  $F_c$ , and (c)  $\beta$  as a function of relative humidity for single-layer h-BN, MoS<sub>2</sub>, and graphene. Interfacial shear strength was estimated by fitting the normal force-dependent friction data to the HPO model using 4.1.  $F_c$  and  $\beta$  were estimated by fitting the sliding speed-dependent friction data to the PTT model using Eq. 4.3. The dashed line is the guide to eye. .... 104

Fig. 4.17. Variation of adhesion forces between AFM tip and the single-layer h-BN, MoS<sub>2</sub> and graphene materials obtained before and after friction force measurement under various relative humidity. .... 105

Fig. 4.18. (a) Topographic images of single-layer h-BN, MoS<sub>2</sub> and graphene after FFM under 75% RH. (b) Estimated thickness of single-layer materials before and after FFM measurements. (c) Schematic of the water diffusion into the interface between the atomically thin material and its underlying substrate. The topographic images were obtained from the intermittent –contact mode AFM, the cross-sectional profiles are included in panels a. The red-dashed lines indicate the location where the cross-sectional profiles are taken. .... 106

Fig. 4.19. Variation of friction force as a function of (a) normal force and (b) sliding speed for single-layer h-BN, MoS<sub>2</sub> and graphene, before and after thermal annealing process. In panel a

and b, friction force data was fitted to the HPO model using Eq. 4.1 and the PTT model using Eq. 4.3, respectively. The error bar corresponds to one standard deviation. .... 109

Fig. 4.20. Variation of friction force as a function of normal force under different temperature (50 °C, 75 °C, and 100 °C) for single-layer h-BN, MoS<sub>2</sub> and graphene. The sliding speed was set to 375 nm/s. The error bars correspond to one standard deviation. .... 110

## ABSTRACT

Two-dimensional (2D) materials such as single-layer hexagonal boron nitride (h-BN), molybdenum disulfide ( $\text{MoS}_2$ ), and graphene have great potential for use as protective and solid lubricant coating layers for nanoscale devices. These coating layers are used to primarily reduce surface damage and friction generated at contacting interfaces between mechanical moving parts, which is the main source of energy dissipation and severe damage in the systems. Therefore, comprehensive understanding of surface damage characteristics and frictional behaviors of single layer h-BN,  $\text{MoS}_2$ , and graphene is essential.

In this work, surface damage characteristics of these single-layer materials were systematically investigated using atomic force microscopy (AFM)-based progressive force and constant force scratch tests. The adhesion strengths to substrate of these atomically thin materials were carefully evaluated based on their critical forces determined using progressive force scratch test. The evolutions of surface damages with respect to normal force were further investigated using constant force scratch test. The results show that single-layer h-BN,  $\text{MoS}_2$ , and graphene strongly adhered to the substrate, which may in turn significantly improve their tribological performances. Furthermore, the defect formation induced by scratch test was found to differently affect the topography and friction force of these atomically thin materials, prior to the failure, which indicates their distinctive surface damage characteristics. Interestingly, the residual strains commonly observed at scratched areas may suggest the scratch tests-induced in-plane compressive strains were dominant over tensile strains, thereby leading to the buckling formation of these atomically thin materials mostly in front of the scratching tip and eventually failure with sufficient strains. These behaviors could be considered as the general failure mechanism of these atomically thin materials due to scratch test. As the number of layer increased, the tribological performance

of atomically thin h-BN, MoS<sub>2</sub>, and graphene were found to significantly improve because of the increase in adhesion strength to the substrate and decrease in surface damage and friction force.

Friction characteristics of these single-layer materials were further investigated under various conditions using friction force microscopy (FFM). The low friction characteristics of these single-layer materials could be clearly observed from their normal force-dependent friction results, and by fitting to Hertz-plus-offset model the interfacial shear strengths could be further estimated. We also found the logarithmic increase in friction with increasing sliding speed, and based on the thermally activated Prandtl-Tomlinson model, some fundamental parameters which governed nanoscale friction such as the effective energy barrier and the effective shape of the interaction potential could be determined. In addition, friction was found to generally increase with increasing relative humidity, which was attributed to the water diffusion-induced increase in puckering effect on frictional behaviors of these single-layer materials as relative humidity increased. Furthermore, friction of the thermally annealed single-layer materials was found to be significantly lower than those of the as-exfoliated ones.

Overall, these findings in this work, including distinctive surface damage characteristics or general failure mechanism of atomically thin h-BN, MoS<sub>2</sub>, and graphene would be useful for the design of effective and reliable nanoscale protective and solid lubricant coating layers based on these materials. In addition, the results also suggest that these single-layer materials used as coating layers should be operated under dry environment and reasonably low speed to achieve low friction and prolong the lifetime of devices. The simple thermal annealing could be useful for many practical applications such as stabilization, packaging, and storage of the nanoscale devices-based on these single-layer materials.

**Key works:** Atomic force microscopy, graphene, h-BN, MoS<sub>2</sub>, nanoscale tribology.

# Chapter 1

## Introduction

### 1.1 Background and Motivation

Layered materials such as hexagonal boron nitride (h-BN), molybdenum disulfide ( $\text{MoS}_2$ ), and graphite are conventionally used as solid lubricants for number of critical engineering applications based on their low friction characteristics. Single sheet of h-BN or graphene is one atom thick, which consists of  $\text{sp}^2$ -bonded hexagonal honeycomb arrangement of alternating boron and nitride atoms or carbon atoms, respectively, as depicted in Figs. 1.1 (a) and (c).<sup>1,2</sup> While a single sheet of  $\text{MoS}_2$  is three atoms thick with one layer of molybdenum atoms surrounded by two layers of sulfur atoms bonded by the strong covalent bond, as shown in Fig. 1.1 (b).<sup>3</sup> These single sheets h-BN,  $\text{MoS}_2$ , and graphene were connected in their bulk form by the relatively weak Van der Waals forces. This characteristically weak interlayer bonding in the structure was found to be responsible for the remarkably low shear strength at the contacting interface of these layered materials.<sup>4,5</sup>

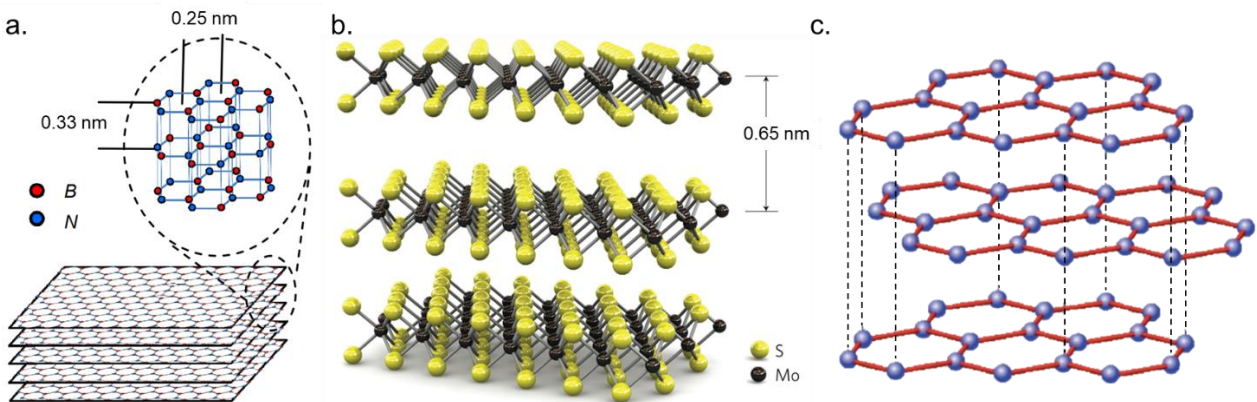


**Fig. 1.1 Schematic structure of atomically thin (a) h-BN,<sup>1</sup> (b)  $\text{MoS}_2$ ,<sup>3</sup> and (c) graphene.<sup>2</sup>**

Interestingly, based on this weak bonding between adjacent layers in the structures, single-layer h-BN, MoS<sub>2</sub>, and graphene could be exfoliated from their bulk forms, and have been extensively studied due to their notable material properties. For instance, superior mechanical properties of these atomically thin materials were reported, in which the in-plane elastic moduli of single-layer h-BN, MoS<sub>2</sub> and graphene were determined to be about 865 GPa,<sup>6</sup> 270 GPa,<sup>7</sup> and 1000 GPa,<sup>8</sup> respectively. Atomically thin h-BN, MoS<sub>2</sub> and graphene also exhibited an outstanding thermal stability up to more than 1,000 °C<sup>3,9,10</sup> as well as phenomenal oxidation resistance.<sup>11-13</sup> In addition, low friction characteristics of these atomically thin materials were observed from the literature with the friction coefficients estimated ranging from 0.001 to 0.1, which clearly demonstrated their ability to effectively reduce friction generated at the contacting interfaces.<sup>14-17</sup>

Apart from material properties, the sub-nanometer thickness of single-layer h-BN, MoS<sub>2</sub> and graphene have made these materials of considerable interest for high-performance nano-scale systems devices, where the spacing between mechanical parts was extremely miniaturized. Therefore, based on the atomic thickness and aforementioned outstanding material properties, atomically thin h-BN, MoS<sub>2</sub> and graphene have been proposed as a protective and solid lubricant coating layers for micro- and nano-electromechanical systems (MEMS and NEMS) devices.<sup>18</sup> Where these coating layers are primarily used to improve tribological performances including friction force reduction, wear protection and surface damage resistance at the contacting interfaces of the mechanical moving part in the systems. Therefore, to prolong the lifetime of high-performance mechanical systems, investigations of the nanoscale surface damage characteristics and frictional behaviors of these atomically thin materials as the protective and solid lubricant coating layers are essential.



In this regard, several studies have been conducted to investigate the nanoscale tribological performances of atomically thin h-BN, MoS<sub>2</sub>, and graphene. Although these studies generally demonstrated the great potential of these atomically thin materials in significantly reducing friction force and surface damage in mechanical systems, the nanoscale surface damage characteristics and frictional behaviors of these atomically thin materials have not been fully explored. Particularly, considering adhesion strengths to the underlying substrates of these atomically thin materials significantly affect their tribological performances, in which strong adhesion strengths often effectively enhance their performances as protective and solid lubricant coating layers. However, determination and characterization of adhesion strength to substrate of these atomically thin materials remain challenged. In addition, surface damages, such as defect formation or plastic deformation, of these atomically thin material may be induced during contact sliding, which could significantly degrade their durability. However, comprehensive understanding of the surface damage characteristics and failure mechanisms of these atomically thin materials induced by contact sliding is still lacking. Furthermore, although intensive efforts have been made to study friction characteristics of single-layer h-BN, MoS<sub>2</sub>, and graphene, number of factors, which could considerably affect their nanoscale frictional behaviors, has not been fully investigated. The motivation of this research is to gain better understanding of nanoscale surface damage and friction characteristics atomically thin h-BN, MoS<sub>2</sub>, and graphene. Such understanding is essential to further elucidate the implementation of these atomically thin materials as nanoscale protective and solid lubricant coating layers.

## **1.2 Objectives of the Research**

In this research, the objective is to gain better understanding of nanoscale surface damage and friction characteristics of atomically thin h-BN, MoS<sub>2</sub>, and graphene. To do so, several AFM-based scratch tests and friction force microscopy (FFM) measurements under various conditions were systematically conducted on these atomically thin materials. Particularly, adhesion strengths to substrate of these atomically thin materials were carefully evaluated based on their critical forces determined using progressive force scratch test. The evolutions of surface damages of single-layer h-BN, MoS<sub>2</sub>, and graphene with respect to normal force were further investigated using constant force scratch test. In addition, the effect of various conditions including normal force, sliding speed, relative humidity and thermal annealing, on frictional behaviors of these atomically thin materials were carefully investigated using FFM.

## **1.3 Organization of the Research**

Following the introductory remarks of this chapter, Chapter 2 presents the literature review about the use of atomically thin h-BN, MoS<sub>2</sub>, and graphene as the protective and solid lubricant coating layers along with their surface damage phenomena at nanoscale. The frictional behaviors of these atomically thin materials associated with nanoscale friction laws is also presented in Chapter 2. In addition, the experimental methods to quantify the nanoscale surface damage and friction force of single- and a few-layer h-BN, MoS<sub>2</sub>, and graphene are included. Fig. 1.2 shows the objective and scope of this research.

The highlight of this research is the comprehensive investigation of the nanoscale surface damage characteristics of atomically thin h-BN, MoS<sub>2</sub>, and graphene, as presented in Chapter 3. In this chapter, the adhesion strength to substrate of these atomically thin materials were carefully obtained. The evolutions of surface damage of single-layer h-BN, MoS<sub>2</sub>, and graphene with respect

to normal force, ranging from elastic deformation to plastic deformation along with defect formation, and eventually to total failure when the applied normal force reached to the critical force, were also clearly observed. The surface damages induced by scratch test differently affected the topography, friction force, as well as crystalline quality of these atomically thin materials, those distinct surface damage characteristics are carefully presented in this chapter. In addition, the general failure mechanism of single-layer h-BN, MoS<sub>2</sub>, and graphene is proposed.

Chapter 4 presents the investigation of frictional behaviors of single-layer h-BN, MoS<sub>2</sub>, and graphene under various conditions. Effects of normal force, tip shape, sliding speed, relative humidity, and thermal annealing on friction force characteristics of these single-materials using FFM measurements are carefully presented in this chapter. Essentially, these single-layer materials all exhibited the low friction force characteristics. Despite the simplicity of the tribological system consisting single-layer material physically deposited on substrate, its frictional behaviors were found to be significantly affected by those number of aforementioned factors. Particularly, the effect of surface slope on friction force fluctuation, and the friction force variation with respect to normal force obtained from the sharp tip and flat-ended tip are carefully presented. By continue using the sharp tip for FFM measurements, the dependences of friction force of these single-layer materials on sliding speed, relative humidity, and thermal annealing are also included in this chapter. The speed-dependent friction characteristics suggest the effect of thermal activation on sliding friction of these single-layer materials. While the dependences of friction force on relative humidity and thermal annealing highlight the importance role of the water interaction and frictional behaviors of these single-layer materials.

Chapter 5 presents the major conclusions of this research along with a few recommendations of future works. Despite significant amount of work on tribological properties of atomically thin

h-BN, MoS<sub>2</sub>, and graphene has been done in this research, to realize the huge potential of these atomically thin materials for use as nanoscale protective and solid lubricant coating layers, interesting and importance works remain. Most importantly, future works should focus on the optimization of the large-scale synthesis of these atomically thin materials by using these tribological characteristics of high quality atomically thin materials presented in this research as references.

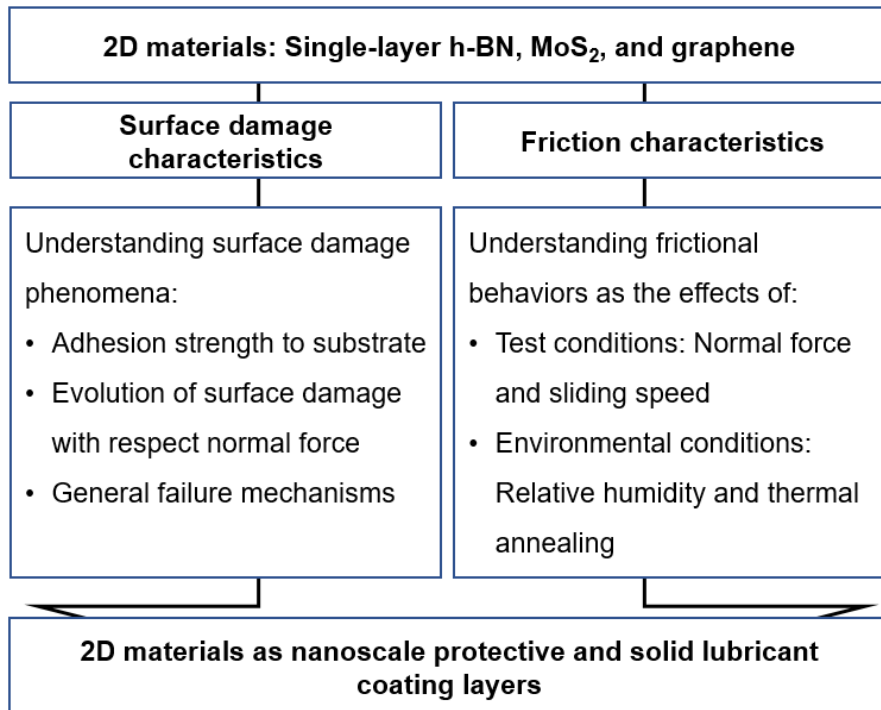


**Fig. 1.2 Objective and scope of this research**

## Chapter 2

### Tribology of 2D materials: Literature review

Tribology is the multidisciplinary study of friction, lubrication, and wear, which often occur at the interfaces between mechanical moving parts in the systems. Friction and wear are the primary sources of energy dissipation and severe mechanical damage, which were proved to have a huge impact on the economy.<sup>19</sup> Therefore, with an aim to effectively improve energy conservation, comprehensive understating corelated tribological phenomena is essential for most mechanical devices. In this regard, protective and solid lubricant coating layers have been developed to improve the tribological performances of mechanical devices including surface damage resistance, friction reduction, which resulting in extending lifetime of devices.

With the development of the micro- and nanoscale technology in recent decades, the mechanical components in micro- and nano-electromechanical system (MEMS and NEMS) devices tend to stick together because of large surface forces. Such “stiction” behaviors have posed several tribological problems that may primarily slow the development of MEMS and NEMS divices.<sup>20,21</sup> 2D materials, such as single- and a few-layer h-BN, MoS<sub>2</sub>, and graphene, with the atomically thin thickness and remarkable material properties have a great potential for use as protective and solid lubricant coating layers for nanoscale devices.<sup>22</sup> Considering the fundamental difference between the macroscale tribology and micro/nanoscale tribology, in which the macroscale lubricant often depends on the formation of liquid or solid interfaces where the lubricant slides against itself, while the micro/nanoscale tribology most likely depends on surface interactions at the original interfaces.<sup>21</sup> Therefore, comprehensive understanding of tribological principles applicable to micro- and nanoscale devices, or nanotribology, of these atomically thin materials is essential. To prolong the lifetime of high-performance nanoscale mechanical systems, extensive efforts have

been made to investigate the wear resistance, surface damage characteristic, friction reduction of these atomically thin h-BN, MoS<sub>2</sub>, and graphene. In the following section, the review of nanoscale tribological characteristics of atomically thin materials is presented.

## 2.1 Synthesis of 2D materials

The first successful separation of single- and a few-layer graphene from graphite was done using mechanical exfoliation method by Novoselov *et al.* in 2004.<sup>2</sup> Since then, this simple yet effective method has enabled fabrication of many other atomically thin materials such as h-BN,<sup>23</sup> MoS<sub>2</sub>,<sup>24</sup> and so on with high crystalline quality, which led to number of exciting discoveries regarding to their fundamental materials properties. In mechanical exfoliation process, graphene layers were repeatedly peeled off using the adhesive tape, and were then transferred to the desire substrate by gently pressing the tape with a few atomically thin materials against the substrate surface. Atomically thin materials were completely deposited to the substrate when the adhesion of these atomically thin materials to substrate was stronger than that between the layers of these materials. Although the mechanical exfoliation method could yield high quality structure of these atomically thin materials, the low production efficiency of this method makes it only suitable for fundamental study of these materials. Modification of mechanical exfoliation method, such as intercalation-assisted exfoliation<sup>25,26</sup> or liquid-based exfoliation,<sup>27,28</sup> have also been developed. Although the synthesized products were found to have some amount of contamination in the structure, these methods were demonstrated to have a good potential for large-scale production of atomically thin materials.

In addition to the exfoliation method, thermal chemical vapor deposition (CVD) techniques were also able to synthesize large-scale atomically thin materials. In the CVD process, number of factors such as materials sources, gas precursors, time, pressure, temperature, and contaminations

could significantly affect to the growth of these atomically thin materials. The optimized CVD-growth conditions should produce the materials that have large-scale, atomically thin, and high crystalline quality. These following CVD procedures were found to be able to synthesize the relatively good quality single-layer h-BN,<sup>29</sup> MoS<sub>2</sub>,<sup>30</sup> and graphene.<sup>31</sup> The CVD synthesis of atomically thin h-BN was done in the quartz tube, the Cu foil (25 μm thick) used as substrate was placed in the center of the furnace and heated at 600 °C in Ar/H<sub>2</sub> (500 sccm) gas flow for about 20 min. Then, the temperature was gradually increased to 1000 °C in 40 min. For the growth of atomically thin h-BN, the ammonia borane (NH<sub>3</sub>-BH<sub>3</sub>) was carried to the reaction region by Ar/H<sub>2</sub> (200 sccm) gas flow. After the growth time of about 30-60 min, the temperature was quickly dropped down to room temperature. In the CVD-growth process of single-layer MoS<sub>2</sub>, crucibles containing MoO<sub>3</sub> and sulfur powder were placed in the center of the furnace and in the upstream zone in the quartz tube, and the target substrates were placed face down with the crucible containing MoO<sub>3</sub>. While the quartz tube was pumped down to a pressure of about 60 mTorr, high-purity N<sub>2</sub> gas was flowed to clean O<sub>2</sub>. The N<sub>2</sub> (100 sccm) gas was then flowed when the furnace was gradually heated to 400 °C with the pressure was about 700 mTorr. For the growth of single-layer MoS<sub>2</sub>, the pressure was reduced to the atmospheric level using a N<sub>2</sub> (10 sccm) gas flow, and the temperature in the furnace was then increased in the range of about 800 °C to 900 °C for 5 min before cooling to room temperature. As for CVD-growth single-layer graphene, the contamination in the quartz tube furnace was cleaned by the H<sub>2</sub> (8 sccm) gas flow with the temperature of about 1000 °C. The CH<sub>4</sub> (24 sccm) was then flowed for about 30 mins at 1000 °C to generate a carbon source. Power and input gases were then turned off, except for H<sub>2</sub>, while the temperature was dropped to room temperature for the growth of graphene. After growth, these atomically thin materials were transfer to desire substrate using wet transfer process.<sup>32</sup> Although large-scale

atomically thin materials could be synthesized by CVD methods, their crystalline qualities were often found to be relatively lower than that of mechanical exfoliated ones.<sup>30,33</sup> Nonetheless, among many other techniques, such as epitaxial growth,<sup>34,35</sup> laser thinning,<sup>36-39</sup> physical vapor deposition (PVD),<sup>40,41</sup> CVD methods were proposed to be the most promising for large-scale growth of atomically thin materials.<sup>42</sup>

## **2.1 Wear resistance and surface damage characteristics of 2D materials**

The remarkable mechanical properties of atomically thin h-BN, MoS<sub>2</sub>, and graphene could probably be the one of the major reasons that attracted tremendous interests for use in various nanoscale applications. Therefore, intensive efforts have been made to study the mechanical characteristics of these atomically thin materials. For example, the in-plane elastic stiffness, out-of-plane bending stiffness of single-layer h-BN, MoS<sub>2</sub>, and graphene were studied theoretically or experimentally. The breaking strength of these single-layer materials were also determined by using the AFM-based nano indentation measurements. Some of these mechanical properties are summarized in Table 2.1. In addition, it was found that the amount of defect in structure of graphene could significantly deteriorate its mechanical strength.<sup>43-47</sup> This behavior was similar to proposed effect of defects and grain boundaries on mechanical behaviors of single-layer h-BN.<sup>29,48,49</sup> Overall, these studies clearly demonstrated the superior in-plane elastic stiffness, and large out-of-plane flexibility of these atomically thin materials, which make them ideally suited for many nanoscale applications such as protective and solid lubricant coating layers.<sup>18</sup>



**Table 2.1. Summary of mechanical properties of layered materials h-BN, MoS<sub>2</sub>, and graphene**

Material	Mechanical properties	Unit	Value	Measurements method	Sample preparation method	Reference
h-BN	In-plane elastic modulus ( $C_{11}$ )	GPa	811.0	Inelastic X-ray scattering	Single-crystalline bulk h-BN	Bosak <i>et al.</i> <sup>50</sup>
	Out-of-plane elastic modulus ( $C_{33}$ )	GPa	27.0			
	Shear modulus ( $C_{44}$ )	GPa	7.7			
	In-plane elastic modulus	GPa	780.0	DFT calculation	Single-layer h-BN	Wu <i>et al.</i> <sup>51</sup>
	Bending rigidity	eV	1.0			
	Breaking strength	GPa	70.5	AFM indentation		Falin <i>et al.</i> <sup>6</sup>
MoS <sub>2</sub>	In-plane elastic modulus ( $C_{11}$ )	GPa	238.0	Hybrid DFT calculation	Single-crystalline bulk MoS <sub>2</sub>	Peelaers <i>et al.</i> <sup>52</sup>
	Out-of-plane elastic modulus ( $C_{33}$ )	GPa	57.0			
	Shear modulus ( $C_{44}$ )	GPa	18.0			
	In-plane elastic modulus	GPa	270.0	AFM indentation	Single-layer MoS <sub>2</sub>	Bertolazzi <i>et al.</i> <sup>7</sup>
	Breaking strength	GPa	23.0			
	Bending rigidity	eV	9.6	Calculation		Jiang <i>et al.</i> <sup>53</sup>
Graphene	In-plane elastic modulus ( $C_{11}$ )	GPa	1109.0	Inelastic X-ray scattering	Single-crystalline graphite	Bosak <i>et al.</i> <sup>54</sup>
	Out-of-plane elastic modulus ( $C_{33}$ )	GPa	38.7			
	Shear modulus ( $C_{44}$ )	GPa	5.0			
	In-plane elastic modulus	GPa	1000.0	AFM indentation	Single-layer graphene	Lee <i>et al.</i> <sup>8</sup>
	Bending rigidity	eV	1.4	Calculation		Lu <i>et al.</i> <sup>55</sup>
	Breaking strength	GPa	125.0	AFM indentation		Falin <i>et al.</i> <sup>6</sup>

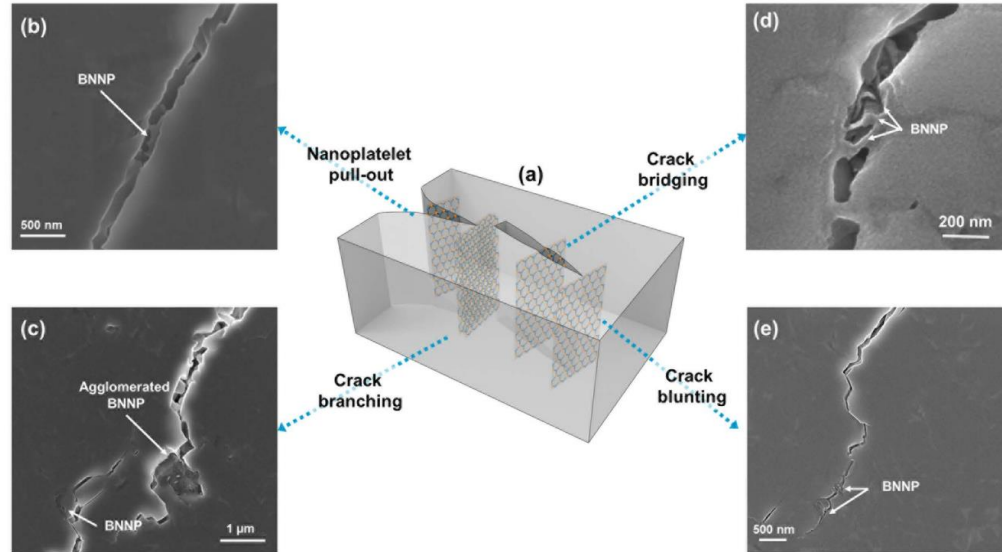


**Fig. 2.1. (a) Schematic image and microstructural evidence of the toughening mechanisms in the ceramic matrix including (b) nanoplatelet pull-out, (c) crack branching, (d) crack bridging, and (e) crack blunting.<sup>56</sup>**

Although the application of atomically thin h-BN as nanoscale protective coating layers is the ongoing interest, studies have demonstrated the h-BN nanotube (BNNT)<sup>57-60</sup> and nanoplatelet (BNNP)<sup>56</sup> as the reinforced components composite materials. For example, the toughness and wear resistance of Si<sub>3</sub>N<sub>4</sub> nanocomposite was found to be significantly enhanced with a small amount of BNNP in the structure.<sup>56</sup> The results show that the BNNPs with 2 vol.% could enhance the fracture toughness (~ 24.7 %), and tribological properties (~ 26.7 %) of the nanocomposite materials with the toughening mechanisms were proposed to be the combination of the pull-out, crack bridging, branching, and blunting mechanisms as depicted in Fig. 2.1. A relatively small amount of nanosheet h-BN additive in water was also found to significantly reduce friction force and amount of wear generated at the contacting interfaces between SiC ball and Si wafer.<sup>61</sup> Furthermore, study on tribological characteristics of cubic-BN (c-BN), amorphous-BN, and h-BN demonstrated that, although these materials are generally good as solid lubricant, the tribological performance of h-BN thin films was found to be relatively poorer than those of c-BN and a-BN.<sup>62</sup> This behavior was

reasoned to be due to h-BN had weaker adhesion strength to the substrate than those of c-BN and a-BN. This studies clearly show the importance effect of adhesion strength to substrate of these layered materials on their tribological performance.

In addition to h-BN, MoS<sub>2</sub> has been the most commonly used solid lubricant coating layers in number of critical applications in macro scale.<sup>63-65</sup> In the vacuum environments, sputtered MoS<sub>2</sub> thin films exhibited friction coefficients from 0.005 to 0.5, and the wear rate of about 10<sup>-8</sup> mm<sup>3</sup>/Nm.<sup>66,67</sup> However, in humid environments, their wear resistances dropped by the factor of about 10-10<sup>3</sup>, and friction coefficients increased to 0.15-0.3.<sup>68</sup> The higher friction of MoS<sub>2</sub> thin films in humid air was found to be due to the reaction between the moisture and oxygen in the environment with these dangling or unsaturated bonds at the edges of these basal planes.<sup>68</sup>

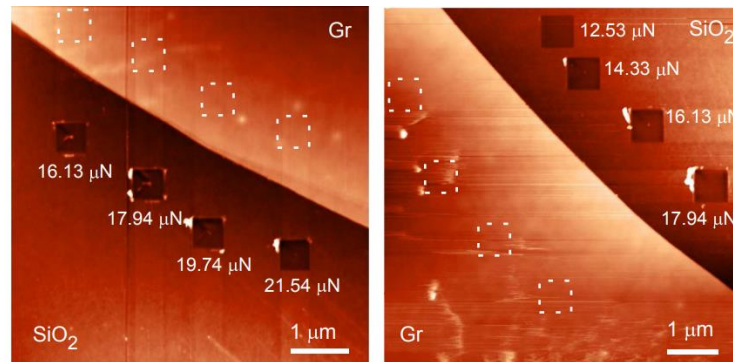


**Fig. 2.2. Topographic images of SiO<sub>2</sub> substrate and multilayer graphene (~ 4.5 nm thickness) after scratch tests under various normal forces. The normal forces were noted in the images.<sup>69</sup>**

Among these atomically thin materials, tribological properties of atomically thin graphene have been mostly studied. Particularly, surface damage protection and wear characteristics of atomically thin graphene prepared by mechanical exfoliation method,<sup>69-71</sup> epitaxial method,<sup>70,72</sup> chemical vapor deposition (CVD),<sup>31,73-75</sup> and thermal decomposition method,<sup>76</sup> have been investigated. The results demonstrated the good surface damage protected provided by multi-layer graphene

deposited on SiO<sub>2</sub> substrate, as shown in Fig. 2.2, in which after scratch test under given normal force, multilayer graphene was found to be likely intact, while SiO<sub>2</sub> substrate were significantly damaged.<sup>69</sup> The remarkable wear resistance of CVD-grown atomically thin graphene was also found, as shown in Fig. 2.3, single-layer graphene could last for 6,500 sliding cycles, and multi-layer graphene (3-4 layers) could survive for 47,000 sliding cycles under high contact pressure of about 0.5 GPa in hydrogen atmosphere.<sup>75</sup> In addition, wear resistance and surface damage protection of graphene was found to be highly sensitive to the environmental conditions, in which the CVD-grown atomically thin graphene could endure for much longer number of cycles sliding in hydrogen atmosphere than in nitrogen atmosphere.

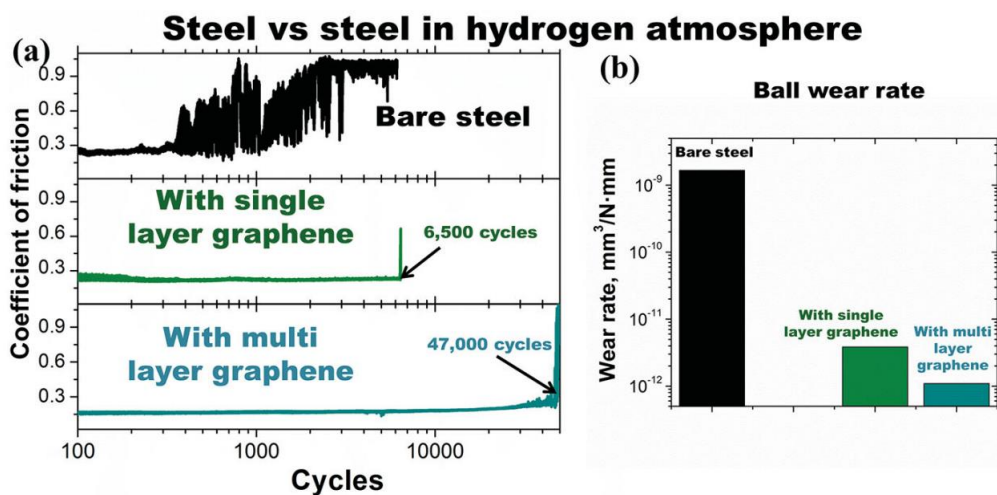


**Fig. 2.3. (a) Coefficient of friction and (b) wear rate for steel against steel sliding tribo-pairs in absence of graphene and in presence of single layer and few-layer graphene in hydrogen environment.<sup>75</sup>**

Although these studies generally demonstrated the great potential of 2D materials in significantly reducing friction and wear in mechanical systems, the nano-scale tribological performance and surface damage characteristics of atomically thin h-BN, MoS<sub>2</sub>, and graphene have not been clearly explored. Particularly, considering that the adhesion strengths to the underlying substrates of the atomically thin films significantly affect their tribological performance,

however determination and characterization of adhesion strength to substrate of these atomically thin films remains challenged. For instance, adhesion strength to substrate of exfoliated graphene with various number of layers was previously studied based on the critical force determined from progressive force scratch test by Shin *et al.*<sup>70</sup> Progressive force scratch test is often recognized as the standard method to characterize the adhesion strength to substrate of thin films based on the critical force. However, as shown in Fig. 2.4, Shin *et al.*<sup>70</sup> found that the critical forces of atomically thin graphene were significantly scattered, even with the same number of layer, due to the complex correlation between the atomically thin materials and their critical forces. Considering the significant effect of adhesion strength to substrate of the atomically thin films on their tribological performances, an accurate and reliable determination of the critical forces is considerably needed.

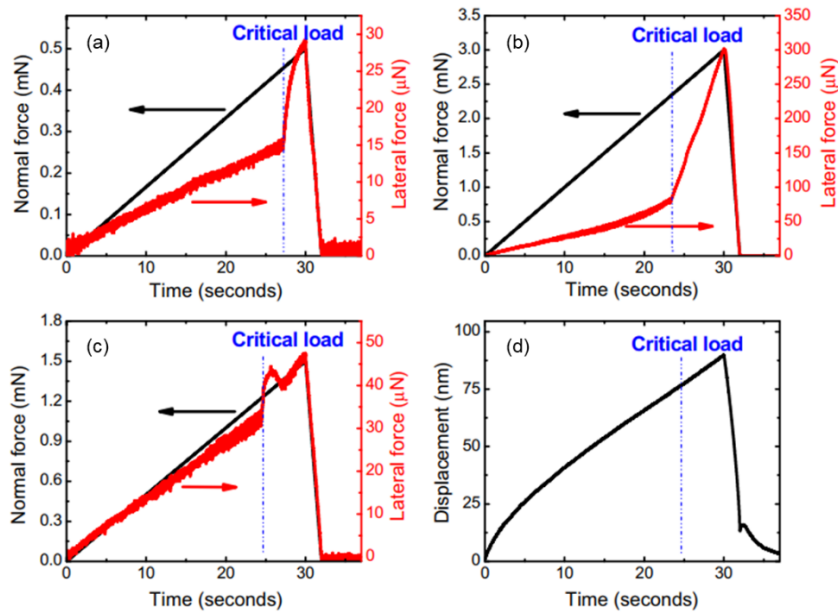


**Fig. 2.4. Normal force and lateral force with respect to time on single layer (a and b) and bilayer (c) graphene. (d) Normal displacement of probe versus time of the sample in (c). All the scratched specimens were exfoliated and pristine graphene.<sup>70</sup>**

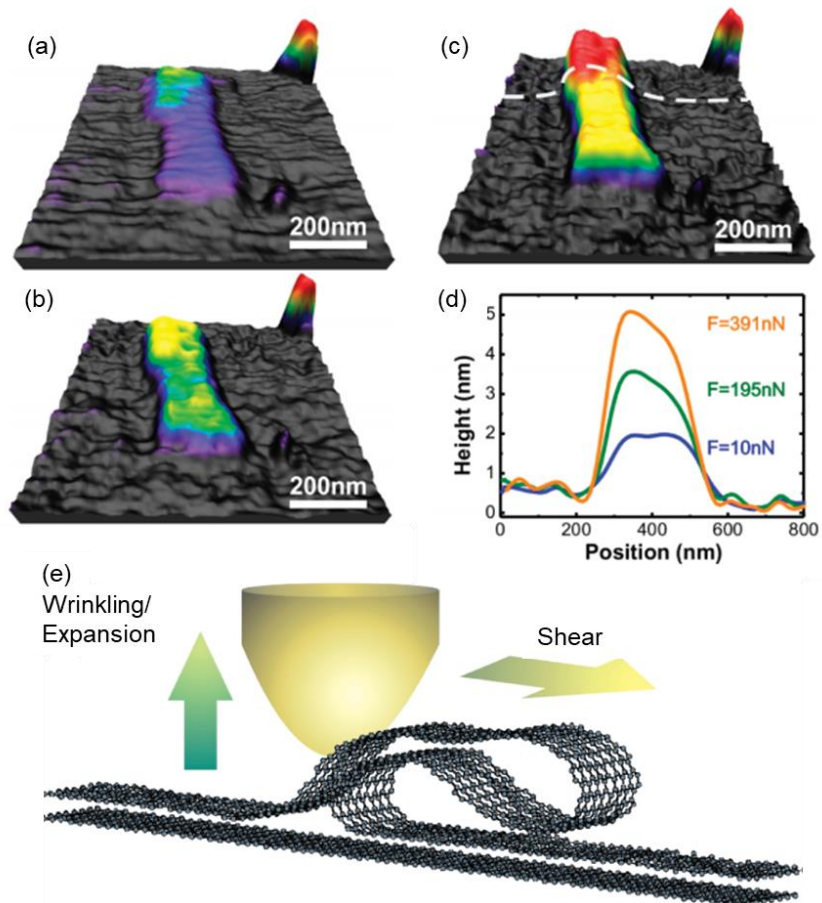


**Fig. 2.5. 3D topographic AFM images of atomically thin graphene obtained using contact mode under increasing normal force: (a) 10 nN, (b) 195 nN, and (c) 391 nN. (d) cross-sectional height profiles taken from the images in (a), (b), and (c) demonstrating the negative strain of atomically thin graphene (expansion upon shear and compression). (e) Schematic illustrating the dynamic wrinkling mechanism of atomically thin materials.<sup>77</sup>**

In addition to the adhesion strength to substrate, investigating on surface damage characteristics of atomically thin h-BN, MoS<sub>2</sub>, and graphene has just been begun. Recent study demonstrated an interesting finding of mechanical response of a few-layer h-BN, MoS<sub>2</sub>, and graphene to the simultaneous shear and compression by AFM.<sup>77</sup> Due to the contact scanning under normal force of about 100 nN, the vertical expansion of these atomically thin materials were observed as shown in Fig. 2.5 (a-d). Based on Fig. 2.5 (e), this expansion was proposed due to the combination of

shear and compressive stresses-induced wrinkle formation of the topmost layers at the areas in front of the moving tip, and the original structures of these atomically thin materials were then restored after the tip passed these areas. Furthermore, failure of atomically thin graphene with plastic deformation of the underlying substrates induced by scratch test was observed from both experiments,<sup>69,71,78</sup> and computational simulations,<sup>71,79</sup> as shown in Figs. 2.6 and 2.7, respectively.

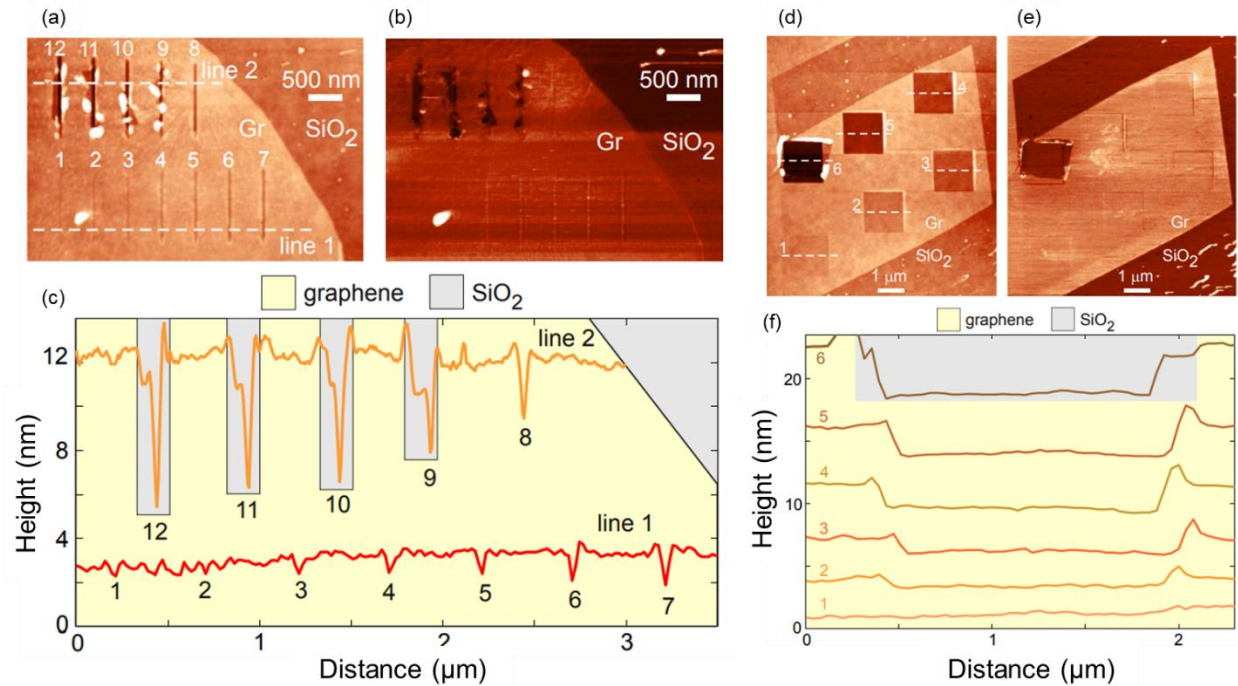


**Fig. 2.6. Scratching graphene with (a-c) line scratching and (d-f) areas scratching. (a and d) Topographic and (b and e) phase images of scratches areas. (c and f) Cross-sectional height profiles obtained from the corresponding topographic images. In panel a, the normal force was gradually increased from 1.41 mN to 17.48 mN (line 1<sup>st</sup> to line 12<sup>th</sup>) and in panel d, the normal force was gradually increased from 1.41 mN to 11.45 mN (area 1<sup>st</sup> to area 6<sup>th</sup>), with respect to the increasing noted number.<sup>69</sup>**

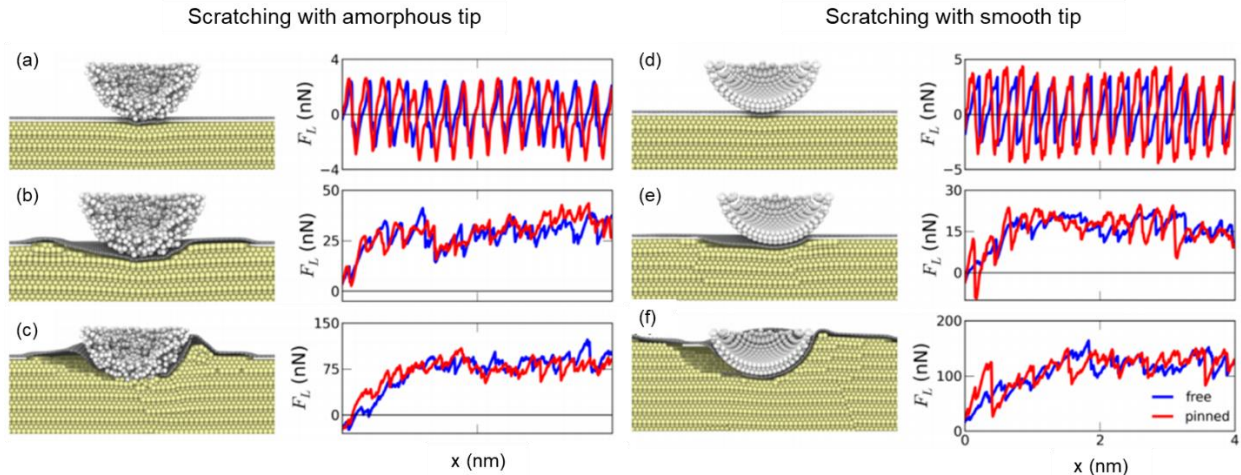


**Fig. 2.7. Scratching single-layer graphene with (a-c) amorphous and (d-f) smooth tips. At low normal forces the Pt substrates deform elastically, the lateral forces  $F_L$  are low and show clearly visible stick–slip (a, d). When substrates deform plastically under the intact graphene layer, the lateral forces increase and the stick–slip pattern disappears (b, e). Single-layer graphene rupture causes strong plastic deformation and formation of wear tracks (c, f).<sup>79</sup>**

From the simulation results, single-layer graphene was found to be intact under relative low normal force, the underlying Pt substrate of single-layer graphene was then plastically deformed as the normal force increased, and single-layer graphene eventually fracture under sufficient normal force.<sup>79</sup> The similar behavior of atomically thin graphene after scratch test was also experimentally observed, in which these scratched graphene was claimed to be plastically deformed with SiO<sub>2</sub> substrate, prior to the failure of graphene.<sup>69</sup> In addition, the combination of experiment and simulation works demonstrated that graphene could be damaged relatively easy when it was scratched at the edge of graphene.<sup>71</sup> Although the plastic deformation was observed at scratched areas of atomically thin graphene, defect formation of atomically thin graphene at the scratched areas were not fully characterized. It should be noted that the significant degradation of mechanical strength of graphene were previously observed due to the appearance of defect in structure of graphene.<sup>47</sup> Therefore, tribological performance of atomically thin graphene could be significantly



affected by defect formation and surface damage due to the close correlation between mechanical strength and tribological performance. Furthermore, despite atomically thin h-BN and MoS<sub>2</sub> were also proposed to have a great potential as a protective and solid lubricant coating layers, compared to atomically thin graphene, understanding of their adhesion strength to substrate as well as surface damage characteristics is still very limited. Hence, to implement these atomically thin h-BN, MoS<sub>2</sub>, and graphene for the protective and solid lubricant coating layers, their surface damage and defects formation induced by scratch test should be well characterized.

## **2.2 Friction force characteristics of 2D materials**

Apart from the wear resistance and surface damage characteristics of atomically thin h-BN, MoS<sub>2</sub>, and graphene, numerous studies have also been conducted to investigate frictional behaviors of these atomically thin materials using friction force microscopy (FFM). FFM could be considered as one of the most powerful tools to study friction characteristics of these atomically thin materials.<sup>21</sup> For example, from the study of CVD-growth single-layer h-BN on Cu,<sup>80</sup> the representative friction loops obtained from bare Cu surface and CVD-growth single-layer h-BN on Cu substrate as shown in Fig. 2.8 (a) clearly demonstrated the significant different friction force between Cu and single-layer h-BN. Fig. 2.8 (b) presents the plot of friction force as a function of normal force of these materials, which further indicated that CVD-grown single-layer h-BN could effectively reduce friction force of Cu substrate more than 40 times. Friction force of these mechanical exfoliated single-layer MoS<sub>2</sub> and graphene was also quantitatively obtained using FFM measurements with Si tip, and the results were shown in Fig. 2.8 (c).<sup>81</sup> These results revealed the relatively different load-dependent friction characteristics of these single-layers materials, which was proposed due to their differences in adhesion force and mechanical responses during FFM measurements. In addition, Fig. 2.8 (d) shows friction force variation with normal force of thermal

decomposed single- and bi-layer graphene obtained in ultra-high vacuum environments.<sup>16</sup> Based on FFM measurements, these studies clearly demonstrated low friction characteristics of atomically thin h-BN, MoS<sub>2</sub>, and graphene.<sup>16,80-82</sup>

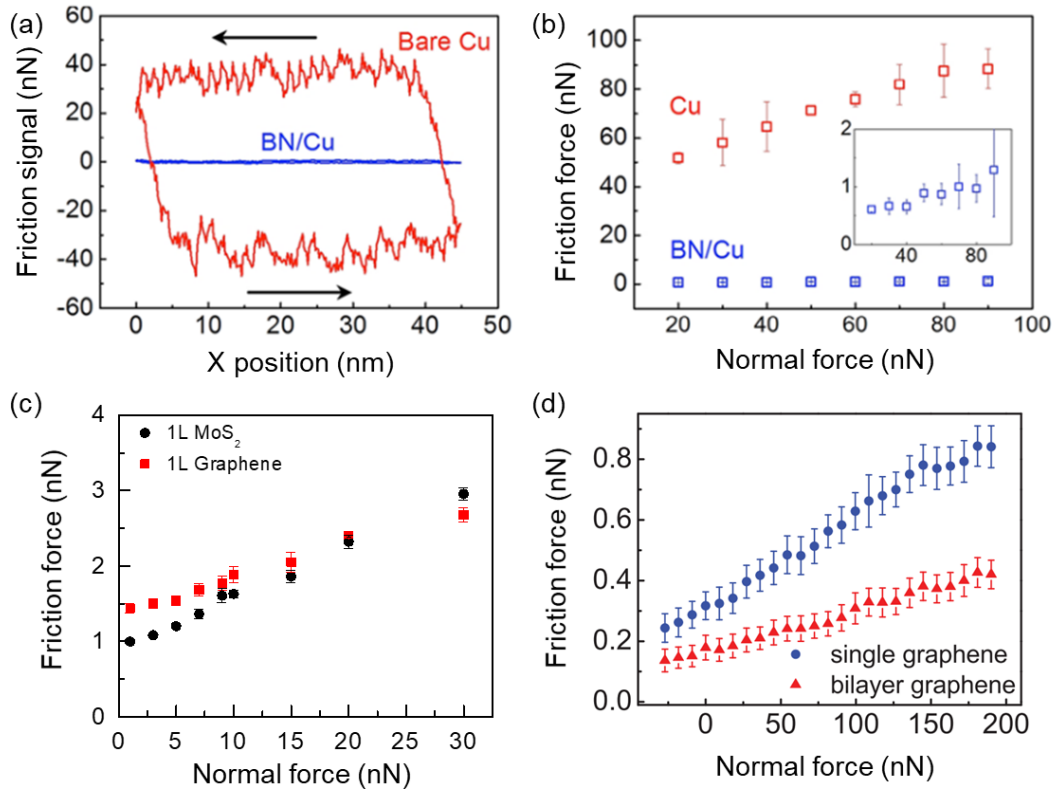


**Fig. 2.8.** (a) Friction loop and (b) load-dependent friction of the bare Cu substrate and single-layer h-BN growth on Cu.<sup>80</sup> (c) Friction force variation of mechanical exfoliated single-layer MoS<sub>2</sub> and graphene with respect to normal force.<sup>81</sup> (d) Friction force variation of thermal decomposition single- and bi-layer graphene with respect to normal force.<sup>16</sup> In panel a, the normal force was 40 nN. In panel a and c, friction force measurements were conducted in ambient condition using Si tip. In panel d, friction force was obtained in ultra-high vacuum environment.

In addition, friction force of these atomically thin materials was found strongly dependent on the number of layers.<sup>16,83-86</sup> Particularly, the thickness-dependent friction force of single- and a few-layer h-BN, MoS<sub>2</sub>, graphene, and NbSe<sub>2</sub> was clearly shown in Fig. 2.9 (a), in which friction

force increased as the number of layers decreased, with the largest friction force being measured from single-layer materials. The out-of-plane deformation of the atomically thin materials in front of AFM tip during contact sliding, referred as “puckering effect”, was found to be responsible for this dependence of friction on number of layers, which was proposed as the general frictional properties of atomically thin materials.<sup>83</sup> In addition, thickness-dependent friction characteristics of these atomically thin materials were found to be significantly affected by the adhesion strength to the substrate and surface morphology.<sup>85,86</sup> For example, suspended graphene or atomically thin graphene were loosely bonded to the relatively rough substrate such as SiO<sub>2</sub>, friction force of graphene increased as the number of layer decreased, whereas when graphene were strongly bonded to the atomically flat substrates, such as mica, h-BN, or bulk-like graphene, friction was not significantly changed as the number of layers changed. These behaviors clearly highlighted the important role of the adhesion and mechanical confinement to the underlying substrate on friction force characteristics of these atomically thin materials.

The effect of interactions between atomically thin materials and the underlying substrate on their friction force characteristics was further investigated. For example, friction of mechanical exfoliated graphene on SiO<sub>2</sub> substrate and CVD-growth graphene on Ni (111) substrate was compared.<sup>87</sup> From the results, shear strength of graphene on SiO<sub>2</sub> was found to be four times larger than that of graphene on Ni (111). This reduction of shear strength of graphene on Ni (111) was concluded to be a combined result of the lower roughness and the commensurate interface of the graphene-Ni (111) system. This result led to the stronger bonding between graphene and Ni (111), which could significantly suppress puckering of graphene. Furthermore, the anisotropic friction of graphene has been recently found, as shown in Fig. 2.10 (a), although no significant variation could be observed from the topographic image of single-layer graphene, three different friction force

areas, or domains, could be clearly observed from the FFM images and the corresponding friction loop.<sup>88</sup> From Fig. 2.10 (b-c), the appearance of these different friction domains was proposed due to ripples-induced anisotropic puckering of graphene. It was found that such ripples were formed by the inhomogeneous interaction of graphene with the underlying SiO<sub>2</sub> substrate, and its effect on anisotropic friction of graphene could be mitigated by increasing normal force. Such anisotropic friction force induced by the inhomogeneous interaction with the underlying substrate could also be expected to be observed on other atomically thin materials.

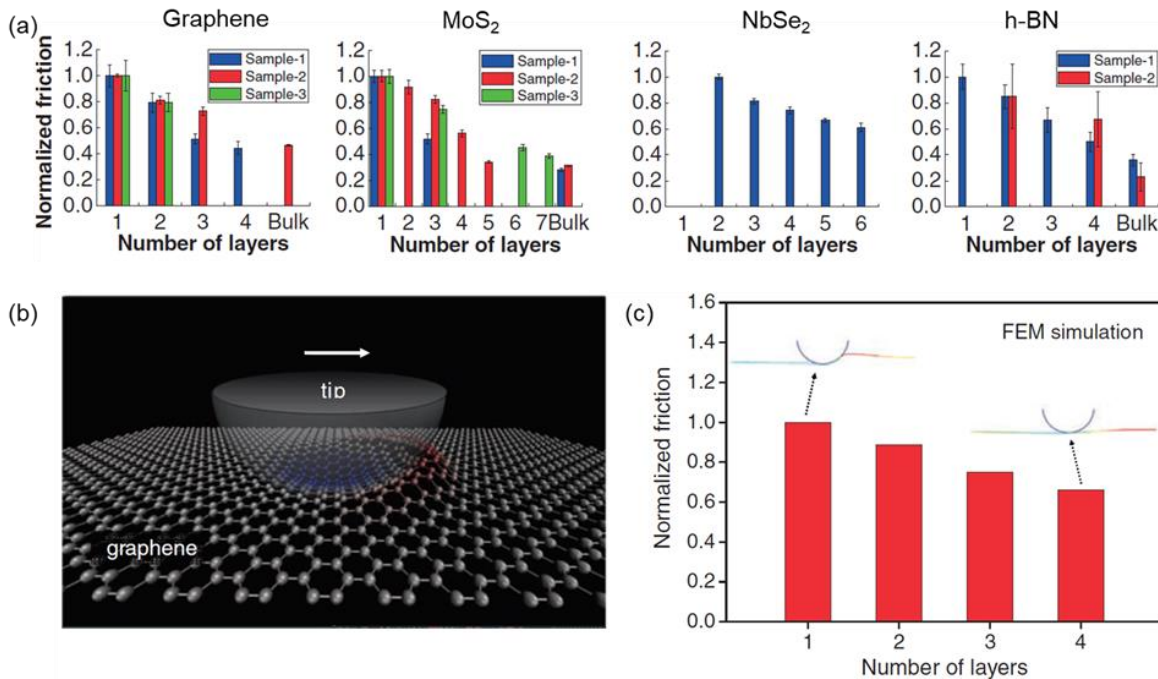


**Fig. 2.9.** (a) Thickness-dependent friction of atomically thin graphene, MoS<sub>2</sub>, NbSe<sub>2</sub>, and h-BN obtained using FFM measurements. (b) Schematic illustrating the puckering effect, in which the adhesion to the sliding AFM tip induced out-of-plane deformation of atomically thin graphene, resulting in the increased contact area and friction. (c) Thickness-dependent friction of atomically thin materials using FEM simulation. In panel a, the out-of-plane deformation was indicated by the color scale. In panel a and c, friction force was normalized by the value obtained for single-layer materials. The inset in c depicted the local out-of-plane deformation of the atomically thin materials around the contact areas for sliding over a single-layer and four-layer material.<sup>83</sup>

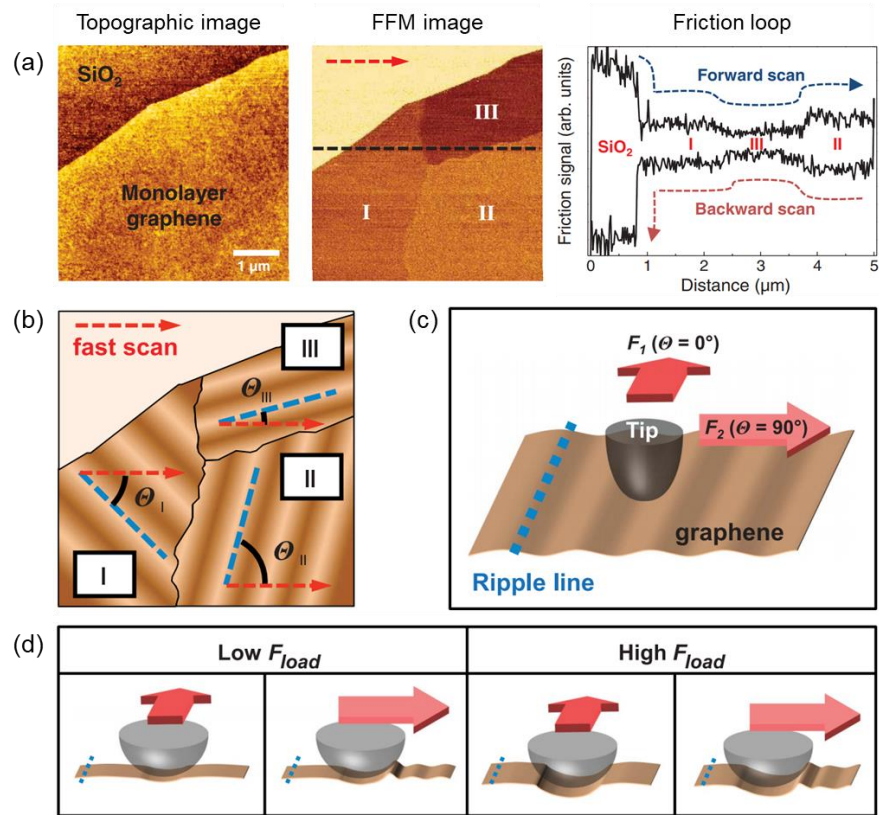


**Fig. 2.10.** (a) Topographic and FFM images of single-layer graphene on SiO<sub>2</sub> substrate along with friction loop. Schematic illustrating the (b) three ripple domains, (c) the relative angle between the ripple lines and scan direction, and (d) the puckering effect during the tip scanning across the surface of graphene under low and high normal force. In panel b, the forward scan direction was indicated by the red dashed arrow, and the back dashed line indicates the location where the friction loop was taken.<sup>88</sup>

In addition to the effect of substrate, friction force characteristics of these atomically thin materials were found to be highly affected by surface modification, including laser treatment,<sup>89</sup> fluorination,<sup>90,91</sup> hydrogenation,<sup>92-94</sup> and oxidation.<sup>92,95</sup> For example, friction of single- and a few layer MoS<sub>2</sub> were recently found to be significantly increased after laser treatment in ambient conditions under various laser powers.<sup>89</sup> As shown in Fig. 2.11 (b), friction of single- and bi-layer MoS<sub>2</sub> locally increased at the laser treated areas, particularly at laser treated areas under 5 mW and 10 mW. This behavior was proposed to be due to the laser-induced particle formation on top

surface of atomically thin MoS<sub>2</sub> after laser treatment as can be clearly seen on Fig. 2.11 (a). Although the origin of these particles was not clearly identified, its effect on friction force characteristics of atomically thin MoS<sub>2</sub> is considerable, especially when laser from Raman was not only commonly used to characterize,<sup>96-98</sup> but also to fabricate these atomically thin materials.<sup>36,37</sup> Therefore caution should be made when exposing these atomically thin materials to any focused laser, which could induce thermal heating to the surfaces.

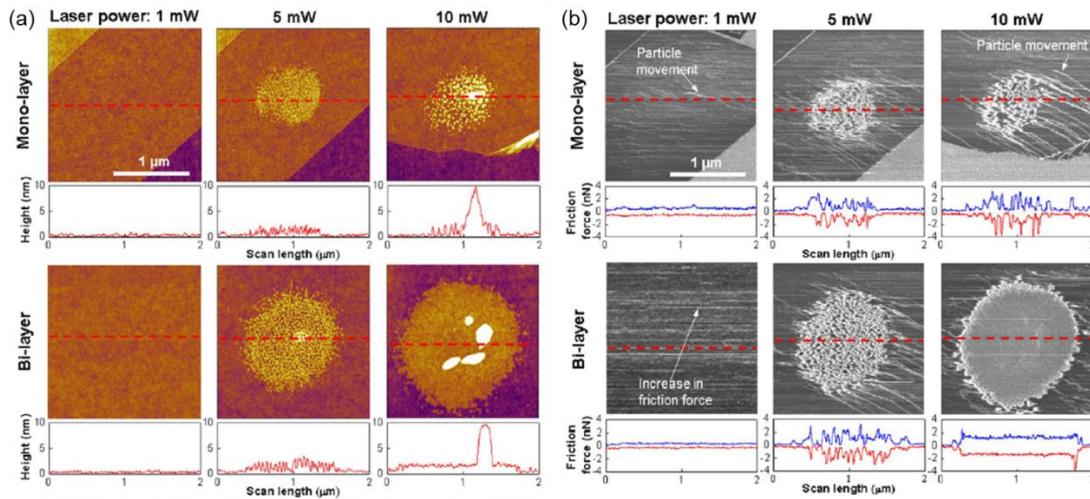


**Fig. 2.11. (a) Topographic and (b) FFM images of single- and bi-layer MoS<sub>2</sub> obtained by intermittent contact and contact mode, respectively, after laser treatment with 1 mW, 5 mW, and 10 mW for 60 s. The red dashed lines indicate the locations where the cross-sectional height profiles and friction loop were taken.<sup>89</sup>**

In addition to the laser treatment, friction force of fluorinated single-layer graphene (FG) was found to be larger (from 4-9 times higher) than that of pristine single-layer graphene as shown in Figs. 2.12 (a) and (b).<sup>90,91,95</sup> The enhancement of friction force of FG was reasoned to be due to the fluorination-induced increase in out-of-plane stiffness,<sup>90</sup> from Fig. 2.12 (b), or increase in corrugation of the interfacial potential originated from the strong local charge concentrated at fluorine sites.<sup>91</sup> Furthermore, by using the conductive AFM lithography, the local nanoscale hydrogenation and oxidation of single-layer graphene under ambient condition could be

achieved.<sup>92</sup> From the results, friction force of hydrogenated graphene and oxidized graphene were found to be about four times and eight times, respectively, larger than that of pristine graphene. The increase in friction of hydrogenated graphene was proposed to be due to the increase in atomic roughness, while adhesion and rigidity were not the dominant reasons.<sup>93</sup> Interestingly, by using the mechanical cleaning method with contact mode of AFM,<sup>99</sup> friction force of graphene and hydrogenated graphene were found to be similar with each other after the surface contamination were significantly removed.<sup>94</sup> Overall, these studies generally demonstrated that friction force of various functionalized single-layer graphene were larger than that of pristine single-layer graphene. Considering those aforementioned factors, such as substrate effect and surface modification, were found to significantly affect friction characteristics of single-layer graphene, similar studies on frictional behaviors of single-layer h-BN and MoS<sub>2</sub> are obviously ongoing interests.

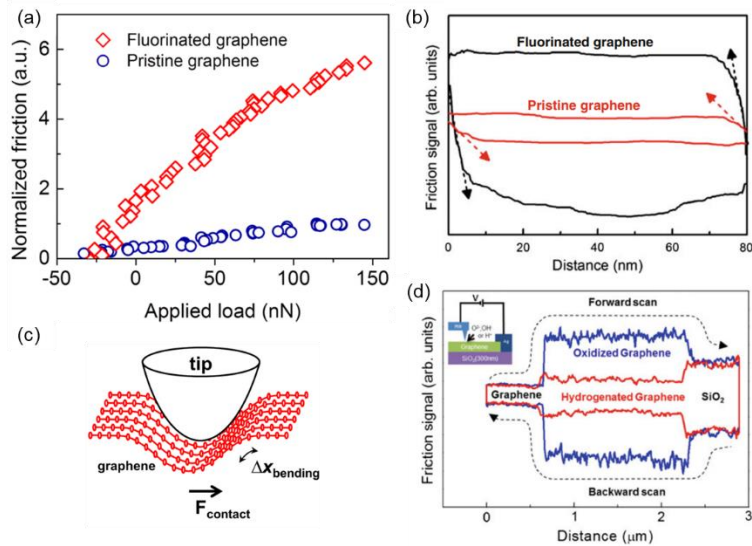


**Fig. 2.12. Plot of (a) normal force-dependent friction force and (b) representative friction loops of fluorinated single-layer graphene and pristine single-layer graphene. (c) Schematic illustrating the FFM measurements with the out-of-plane bending deformation. (d) Representative friction loops obtained from graphene, hydrogenated graphene, oxidized graphene, and SiO<sub>2</sub> substrate.<sup>90,95</sup>**

In addition to the dry frictional behaviors of these atomically thin materials, friction force between flow of water molecules with surface of single-layer h-BN, MoS<sub>2</sub>, and graphene was also investigated based on the molecular dynamic simulation.<sup>100,101</sup> The friction coefficients for water on surface of single-layer MoS<sub>2</sub>, graphene, and h-BN shown in Figs. 2.13 (a) and (b), respectively, defined as the ratio between friction force parallel to the surface per unit area, and were obtained by the plateau value of friction coefficient for a long times.<sup>100</sup> Friction coefficients for water on surface of single-layer h-BN, MoS<sub>2</sub>, and graphene were estimated to be about  $30.0 \times 10^4$  Ns/m<sup>3</sup>,  $17.8 \times 10^4$  Ns/m<sup>3</sup>, and  $9.6 \times 10^4$  Ns/m<sup>3</sup>, respectively. And the corresponding slip lengths of water on surface of single-layer h-BN, MoS<sub>2</sub>, and graphene were also determined to be about 1.8 nm, 3.3 nm, and 10.4 nm, respectively. The estimated water slippage on surface of single-layer h-BN, MoS<sub>2</sub>, and graphene indicate the surface hydrophobicity with low friction coefficients of these single-layer materials.

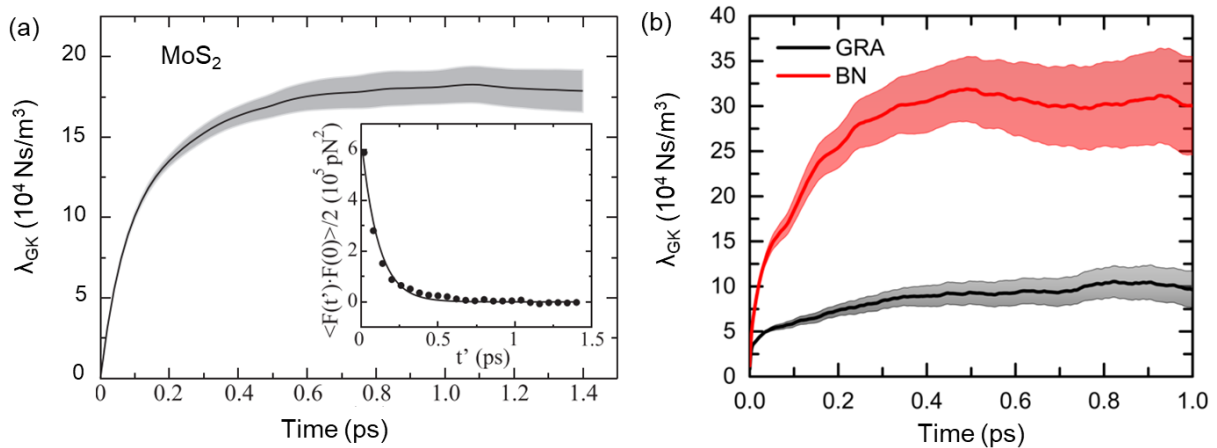


**Fig. 2.13.** The Green-Kubo estimate of friction coefficients of liquid water on (a) MoS<sub>2</sub>, and (b) graphene and h-BN. The friction coefficients  $\lambda$  was obtained by the plateau value for long time. The shaded areas represent the error bars. The inset in panel a is the time-dependency of force correlation function and the fit of solid line indicates an exponential decay.<sup>100,101</sup>



## Chapter 3

### Surface damage characteristic of 2D materials

To prolong lifetime of nanoscale mechanical systems, investigations of the tribological performance and surface damage characteristics of 2D materials, including atomically thin h-BN, MoS<sub>2</sub>, and graphene as the protective and solid lubricant coating layers are essential. Several studies were conducted to assess nano-scale wear resistance and surface damage protection of atomically thin h-BN,<sup>56,61</sup> MoS<sub>2</sub>,<sup>102</sup> and graphene.<sup>31,69,71,72,79</sup> Although these studies generally demonstrated the potential of these atomically thin materials in significantly reducing friction and wear in mechanical systems, their nanoscale tribological performance and surface damage characteristics have not been clearly explored. Considering adhesion strengths to the underlying substrates of the atomically thin materials significantly affect their tribological performances, however determination of adhesion strength to substrate of these atomically thin materials remains challenged. In addition, surface damage characteristics of these atomically thin materials have not been fully characterized. Hence, to implement atomically thin h-BN, MoS<sub>2</sub>, and graphene for the protective and solid lubricant coating layers, comprehensive understanding of their adhesion strength to substrate as well as surface damage characteristics is crucial.

In this chapter, adhesion strengths to substrate and surface damage characteristics of atomically thin h-BN, MoS<sub>2</sub> and graphene were systematically investigated using progressive and constant force scratch tests. The scratch tests were all performed in the AFM system using diamond tip with an aim to provide more accurate force measurements. Scratched areas were carefully examined by AFM and Raman spectroscopy measurements. Based on these observations, surface damage of atomically thin h-BN, MoS<sub>2</sub> and graphene induced by scratch tests were clearly observed.

### 3.1 Experimental section

Single- and a few-layer h-BN, MoS<sub>2</sub>, and graphene were mechanically exfoliated from the high-quality single crystalline h-BN (HQ Graphene), MoS<sub>2</sub> (SPI Supplies) and graphite (NGs), respectively. The atomically thin materials were then deposited onto silicon (Si) wafer capped by a thermally grown SiO<sub>2</sub> layer with 300 nm thickness. Optical microscopy (VK-X200, Keyence), AFM (MFP-3D, Asylum Research), and Raman spectroscopy (Alpha300R, Witec) were then employed to carefully examine the topography and thickness of the atomically thin materials, prior to the scratch tests. Particularly, the atomically thin materials (single- and a few-layer) were firstly located using the optical microscopy. Their topographic images were then obtained from the intermittent contact mode of AFM using Si probes with nominal spring constant of 2 N/m (AC240, Olympus). Thickness of atomically thin materials was determined based on the cross-sectional height profiles obtained from topographic images. To further confirm the number of layers, Raman spectroscopy measurements were performed using an excitation laser wavelength of 532 nm. Raman spectra was collected through a 100× objective (NA ~ 0.9) with a laser spot size of about 720 nm and the spectra resolution was set to be about 1.4 cm<sup>-1</sup> (1800 lines/mm grating). In addition, the laser power was kept below 0.5 mW with an acquisition time of 10 sec during Raman measurement to eliminate the laser-induced thermal effect<sup>103</sup> and particle formation<sup>89</sup> on these atomically thin materials.

After careful preparation and characterization of atomically thin h-BN, MoS<sub>2</sub> and graphene, their tribological performances were systematically investigated using AFM-based scratch tests including progressive force scratch test, constant force scratch test. The nano-crystalline diamond tip (NaDiaProbes, Advanced Diamond Technologies), with a tip radius of about 40 nm, was used in both progressive force and constant force scratch tests. For the quantitative force measurements

using AFM, the cantilevers were calibrated in both normal<sup>104</sup> and lateral<sup>81,105</sup> directions. Based on the force calibration results, normal spring constant and lateral sensitivity of diamond probe used for scratch tests were about 45 N/m and 0.02 mV/nN, respectively. In addition, sliding speed of diamond tip was set to 500 nm/s for both scratch tests.

In the progressive force scratch test, single-layer h-BN, MoS<sub>2</sub> and graphene were scratched under a progressive normal force for one single scratch line with the scratch distance of 2 μm. First, the diamond tip was brought into contact with these single-layer materials under relatively low normal force of 400 nN to keep the tip stable on the specimen surface.<sup>71</sup> Once this contact was established, the specimen was scratched under normal force progressively increased from 400 nN up to 4,000 nN to find the critical force of the specimen. The critical force was defined as the normal force, where the atomically thin materials were totally torn-off and the substrate was exposed.<sup>70</sup> The critical force was determined from 3-5 sets of progressive force scratch test. To further determine the effect of number of layers on adhesion strength to substrate of these atomically thin materials, the progressive force scratch tests were performed with bi-layer, tri-layer, and multi-layer h-BN, MoS<sub>2</sub> and graphene.

In constant force scratch test, single-layer h-BN, MoS<sub>2</sub> and graphene were scratched at defined areas of 1 μm × 1 μm under constant normal force. At each area, these single-layer materials were scratched under given normal force ranging from 500 nN to 5,000 nN to observe the evolution of surface damage characteristics of single-layer materials with respect to normal force. An area scratching was selected in this test with an aim to facilitate the observation of scratched area using AFM and Raman spectroscopy measurements. Adhesion force between AFM tip and materials were carefully monitored during all scratch tests. Furthermore, the contact pressure between the

AFM tip and SiO<sub>2</sub> substrate was estimated by the Derjaguin-Muller-Toporov (DMT) contact model for the attractive forces that were predominant outside of the contact area.<sup>106</sup>

To clearly observe the topography and frictional behaviors of scratched areas, the intermittent-contact and contact modes of AFM were carefully conducted after scratch tests. In intermittent contact imaging, the relatively sharp Si tips (SuperSharpSilicon, Nanosensors) with the nominal tip radius of about 2 nm were used. FFM images of these single-layer materials were obtained from the contact mode of AFM using compliant Si tip (LFMR, Nanosensors) with a nominal spring constant of 0.2 N/m. The normal force was set to be 0.5 nN in the contact mode imaging to observe frictional behavior of the scratched areas without further introducing undesirable surface damage to the single-layer materials. In addition to the AFM measurements, after the constant force scratch tests, with an aim to further investigate the surface damage characteristics of single-layer h-BN, MoS<sub>2</sub> and graphene, the scratched areas were characterized using Raman intensity mapping. Raman intensity mapping image was obtained by scanning across these single-layer materials with the laser step size of about 230 nm and acquisition time of about 0.5 sec to 1.0 sec for each spectrum. All experiments, including AFM and Raman spectroscopy measurements, were conducted in ambient conditions (25°C, 30% RH).

### **3.2 Thickness determination of 2D materials**

Fig. 3.1 (a) shows optical microscopy images of single- and a few-layers h-BN, MoS<sub>2</sub> and graphene on the SiO<sub>2</sub> substrate. The locations of single-layer MoS<sub>2</sub> and graphene could be clearly identified based on their relatively strong thickness-dependent optical contrast. While single-layer h-BN were relatively difficult to observe by optical microscopy due to their low optical contrast on SiO<sub>2</sub> substrate.<sup>96</sup> As the number of layers increased, the optical contrasts of these atomically thin materials were increased, and single-layer h-BN could be randomly located nearby those

thicker ones. Topographic images of the atomically thin materials obtained from the intermittent-contact mode as shown in Fig. 3.1 (b) clearly demonstrate the relatively clean surface of these materials. Furthermore, based on the cross-sectional height profiles, thickness of single-layer h-BN, MoS<sub>2</sub>, and graphene was determined to be about 0.38 nm, 0.86 nm, and 0.43 nm, respectively.

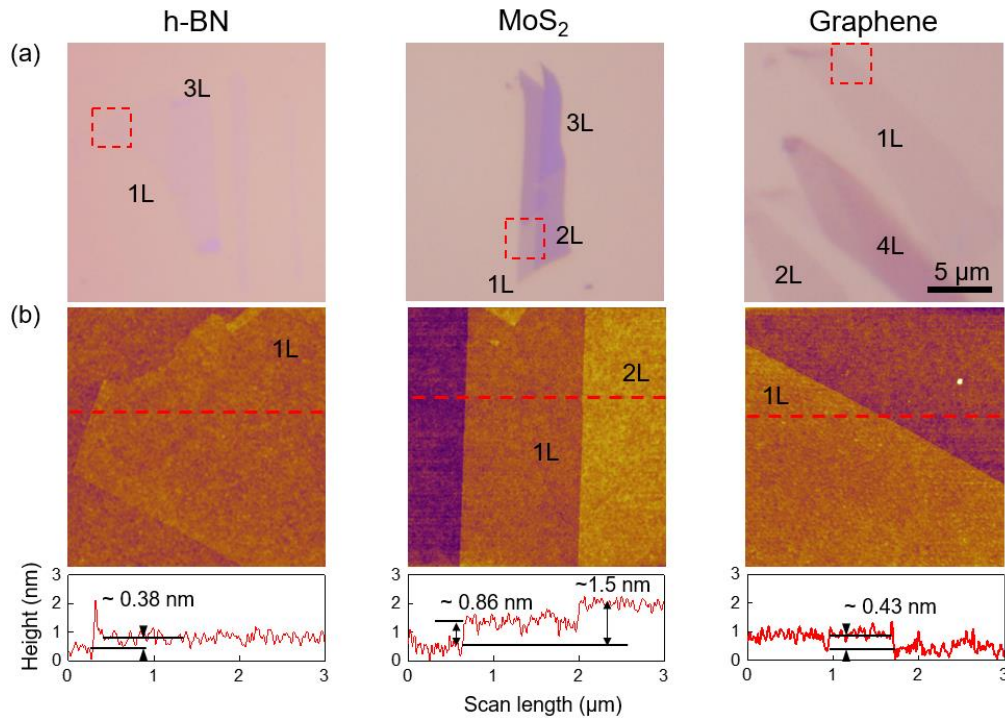


**Fig. 3.1. (a) Optical microscopy images and (b) AFM topographic images of single- and a few layer h-BN, MoS<sub>2</sub>, and graphene. The topographic images were obtained from the intermittent contact mode of AFM. In panel b, the cross-sectional profiles are included and the red dashed lines indicate the location where the cross-sectional profile are taken.**

Thickness of single- and a few-layer h-BN, MoS<sub>2</sub>, and graphene with respect to number of layers as shown in Fig. 3.2 (a), clearly demonstrates the linear dependence between thickness and number of layers. The interlayer spacing values of h-BN, MoS<sub>2</sub>, and graphene were estimated to be about 0.35 nm, 0.64 nm and 0.37 nm, respectively, which are consistent with theoretical values of these layered materials. Furthermore, Fig. 3.2 (b) show the variation of surface roughness values of h-BN, MoS<sub>2</sub> and graphene with respect to the number of layers. Surface roughness values were

determined from AFM topographic images obtained at five different locations with a  $1\ \mu\text{m} \times 1\ \mu\text{m}$  scanning area. Surface roughness of single-layer h-BN, MoS<sub>2</sub>, and graphene was determined to be about 0.16 nm, 0.14 nm, and 0.15 nm, which clearly show the atomically flat surfaces of these single-layer materials used in this work. In addition, the surface roughness of these single-layer materials were found to be closed to that of SiO<sub>2</sub> substrate ( $\sim 0.17\ \text{nm}$ ), suggesting the good flexibility and conformity of these single-layer materials to underlying substrate. Furthermore, as the number of layers increased, the surface roughness of these atomically thin materials was found to be generally decreased. This behavior is likely due to the increasing of bending rigidity of these atomically thin materials as their number of layer increase, which lead to less dominant effect of the substrate roughness to the morphology of the atomically thin materials. Overall, the variation of thickness and surface roughness of single- and a few-layer h-BN, MoS<sub>2</sub>, and graphene with respect to number of layer clearly revealed the atomically thin and flat surface of these materials.

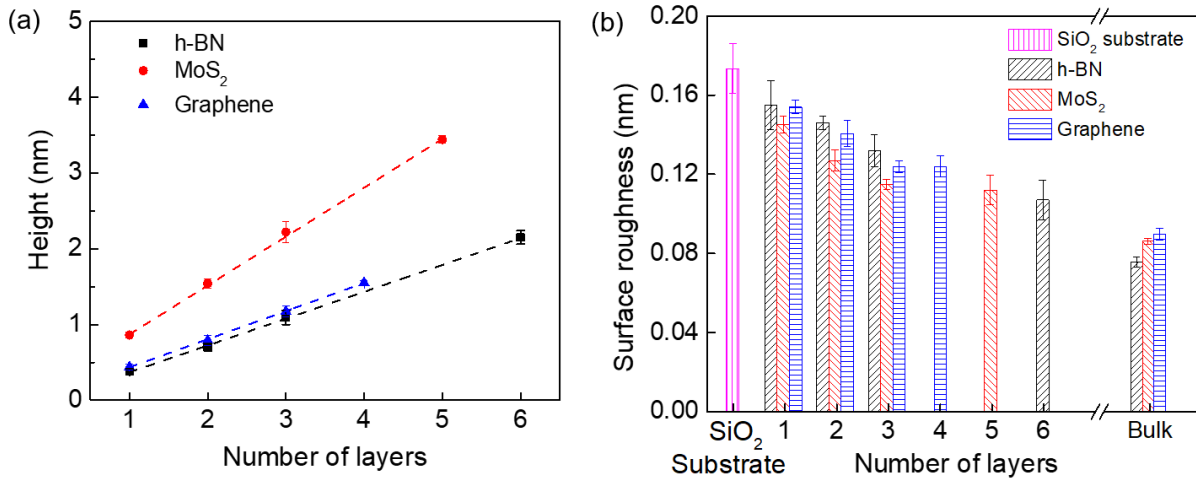


**Fig. 3.2. Variation of (a) thickness and (b) surface roughness of atomically thin h-BN, MoS<sub>2</sub> and graphene with respect to number of layers. The error bar represents one standard deviation.**

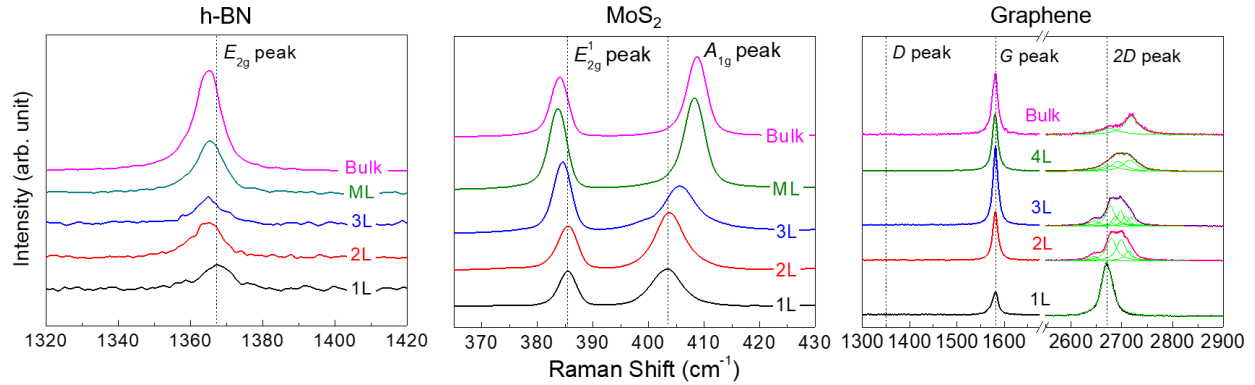


**Fig. 3.3. Raman spectra of single- and a few layer h-BN, MoS<sub>2</sub>, and graphene. Frequency of the characteristic peak of single layer h-BN, MoS<sub>2</sub>, and graphene are denoted as dashed lines for comparison. Raman 2D peaks of graphene were fitted using Lorentzian function.**

Thickness of single- and a few-layer h-BN, MoS<sub>2</sub>, and graphene were further examined by Raman spectroscopy with a 532 nm excitation source at room temperature. Fig. 3.3 shows the Raman spectra of atomically thin h-BN, MoS<sub>2</sub> and graphene, which clearly demonstrate the dependence of their Raman characteristic peaks on thickness. Particularly, Raman spectra of single-layer h-BN show relatively weak  $E_{2g}$  characteristic peak ( $\sim 1367 \text{ cm}^{-1}$ ), arising from the in-plane vibration of B-N atoms.<sup>96</sup> As number of layers increased, the intensity of  $E_{2g}$  peak significantly increased and its frequency decreased (redshifted), which agree with previous study.<sup>96</sup> In the case of atomically thin MoS<sub>2</sub>, their Raman spectra shows two Raman characteristic peaks,  $E_{2g}^1$  peak and  $A_{1g}$  peak, which are associated with the in-plane vibration of Mo-S atoms and the out-of-plane vibration of the S atoms, respectively.<sup>97</sup> As the number layer decreased from bulk to single layer, the frequency of  $E_{2g}^1$  peak increased (blueshifted) while that of  $A_{1g}$  peak decreased (redshifted), which is also consistent with the other study.<sup>97</sup> As for atomically thin graphene, two Raman characteristic peaks including G peak ( $\sim 1580 \text{ cm}^{-1}$ ) and 2D peak ( $\sim 2670 \text{ cm}^{-1}$ ) can be clearly observed from the Raman spectra. Among G peak and 2D peak, which are resulted from the in-plane vibration of the  $sp^2$  carbon atoms and a two-phonon double resonance Raman process,

respectively, 2D peak was used to identify the number of graphene layer.<sup>98</sup> In particular, single-layer graphene shows a sharp and symmetric 2D peak which can be fitted by only one Lorentzian peak, as the thickness increased, 2D peak becomes broader and increased in its frequency (blueshifted), for instance, 2D peak of bi-layer graphene splits into four Lorentzian peaks,<sup>98</sup> and that of graphite clearly consisting of two Lorentzian peaks.<sup>107</sup>

### **3.3 Adhesion strength to substrate of single-layer materials**

After characterization of the thickness of the atomically thin h-BN, MoS<sub>2</sub>, and graphene using AFM and Raman spectroscopy, the adhesion strength to substrate of these atomically thin materials were evaluated based on their critical force determined from the progressive force scratch test. In this test, single-layer h-BN, MoS<sub>2</sub> and graphene were scratched by the diamond tip under normal force progressively increased from 400 nN to 4,000 nN. The critical force was defined as the normal force, where the atomically thin film was torn-off and the underlying substrate was exposed. The large critical force indicates that the atomically thin film is strongly adhered to substrate. However, accurate and reliable determination of critical force of atomically thin films from scratch test has been remained a challenge.<sup>70,108</sup>

In this work, by carefully matching the lateral force variation with respect to normal force during progressive force scratch test with the topographic and friction force microscopy (FFM) images of scratched areas, the critical force and surface damage of single-layer h-BN, MoS<sub>2</sub>, and graphene were clearly characterized. In particular, the lateral force variation with respect to normal force during progressive force scratch test was monitored as shown in Fig. 3.4 (a), the failure of atomically thin materials under given normal force was indicated by an abruptly increase of lateral force. Furthermore, scratch tracks of the atomically thin materials were clearly observed based on the topographic and FFM images of the scratched areas as depicted in Figs. 3.4 (b) and (c),



respectively. Topographic images of scratched areas were obtained using the relatively sharp silicon AFM tip with the nominated tip radius around 2 nm, which is roughly 20 times smaller than that of the AFM diamond tip used for scratch tests, hence topography of scratched areas could be clearly observed. In addition, FFM images from only the forward scan were included for clarify, where the darker contrast indicates lower friction and brighter contrast indicates larger friction. Since friction force the SiO<sub>2</sub> substrate is significantly larger than those of atomically thin materials, therefore the failure of atomically thin materials could also be observed from FFM images. Based on these observations, the critical forces of single-layer h-BN, MoS<sub>2</sub> and graphene were determined to be  $\sim 900 \pm 200$  nN,  $\sim 1,300 \pm 150$  nN, and  $\sim 3,300 \pm 200$  nN, respectively, which are corresponding to the contact pressure of about 7.57 GPa, 8.51 GPa, and 11.52 GPa, respectively. The contact pressure was estimated by the Derjaguin-Muller-Toporov (DMT) contact model, in which the attractive forces between AFM tip and SiO<sub>2</sub> substrate were predominant outside of the contact area.<sup>106</sup> Considering the compressive strength of thermally grown amorphous SiO<sub>2</sub> substrate is about 0.69 ~ 1.38 GPa,<sup>109</sup> these estimated critical contact pressures clearly demonstrate the significant improvement of the load carrying capacity of the SiO<sub>2</sub> substrate provided by single-layer h-BN, MoS<sub>2</sub>, and graphene. Furthermore, among these single-layer materials, the results also suggest that single-layer graphene has the largest critical force, followed by single-layer MoS<sub>2</sub> and h-BN, which indicates that single-layer graphene may have stronger adhesion strength to substrate than those of single-layer MoS<sub>2</sub> and h-BN. Considering that the critical forces of these atomically thin materials could be strongly influenced by their mechanical properties.<sup>70</sup> In particular, the breaking strengths of single-layer h-BN, MoS<sub>2</sub>, and graphene were reported about 23 N/m,<sup>6</sup> 15 N/m,<sup>7</sup> and 42 N/m,<sup>8</sup> respectively. The significantly lower mechanical strengths of single-layer h-BN and MoS<sub>2</sub>, compared to single-layer graphene, could be responsible for the less mechanical

stability induced by scratch test.<sup>110</sup> Therefore, single-layer h-BN and MoS<sub>2</sub> were found to be relatively easily deformed, while single-layer graphene could effectively endure more normal force. Even though single-layer h-BN and MoS<sub>2</sub> are generally good as solid lubricant, these relatively weak adhesion strengths to substrate could significantly degrade their tribological performances.

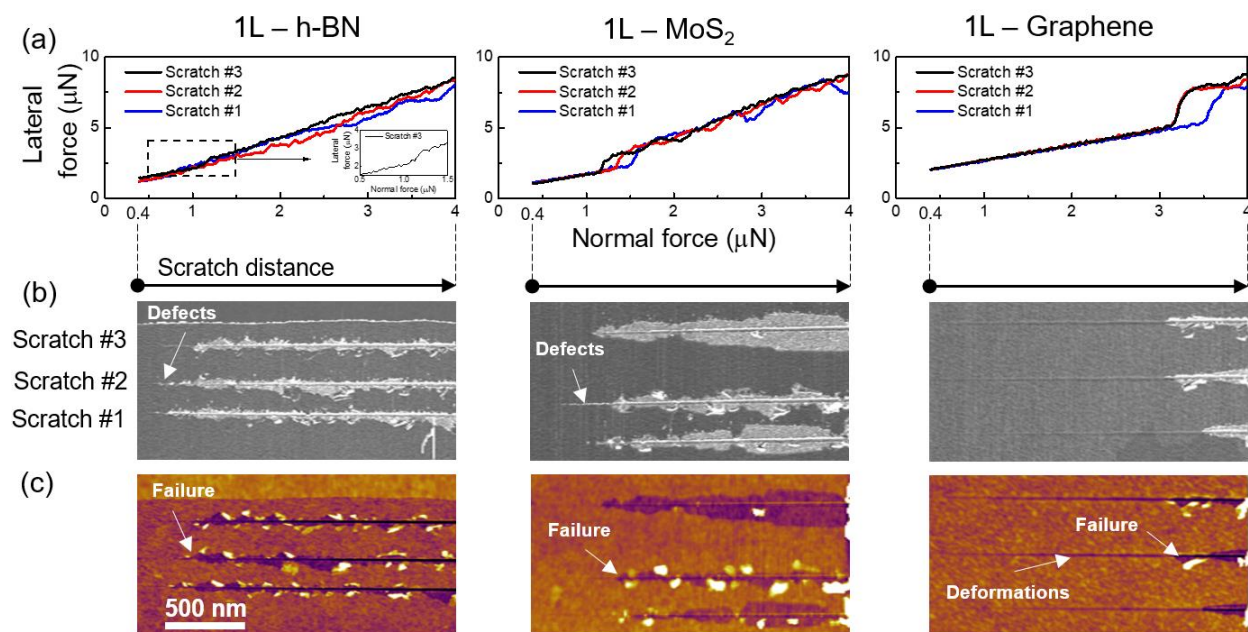


**Fig. 3.4. Progressive force scratch test results of single-layer (from left to right) h-BN, MoS<sub>2</sub>, and graphene. (a) Lateral force variation with respect to normal force during progressive force scratch tests. The normal force was progressively increased from 400 nN to 4000 nN with a scratch distance of 2 μm. (b) FFM images (forward scans), and (c) topographic images of scratch tracks from single-layer h-BN, MoS<sub>2</sub> and graphene after progressive force scratch tests. Critical force of single-layer materials were determined by the abruptly change in lateral force during scratch test, where the failure of these single-layer materials occurred and the substrate was exposed.**

From the topographic images of scratch tracks as shown in Fig. 3.4 (c), single-layer h-BN and MoS<sub>2</sub> were torn-off along with the expose of substrate, shortly after scratch tracks were formed on top surface of these materials. Furthermore, as shown in the corresponding FFM images, shortly

prior to the failure of single-layer h-BN and MoS<sub>2</sub>, the scratch tracks exhibited an increase in friction which indicates a certain amount of defect was probably formed at scratch tracks. Interestingly, in the case of single-layer graphene specimen, based on the topographic image of the scratch tracks as shown in Fig. 3.4 (c), a height decrease at scratch tracks with increasing normal force was observed, prior to the failure. While the corresponding FFM image from Fig. 3.4 (b) shows that the scratch tracks of graphene could maintain its low frictional behavior, until the failure occurred. This behavior indicates that the underlying SiO<sub>2</sub> substrate could be plastically deformed due to scratch test, and by owing the superior mechanical strength, single-layer graphene was able to cover that deformed substrate up until its failure point. The out-of-plane bending of atomically thin materials induced by scratch test is likely responsible for the deformation of the underlying substrate. Particularly, bending modulus of single-layer h-BN, MoS<sub>2</sub> and graphene were reported to be about 0.95 eV,<sup>51</sup> 9.61 eV,<sup>53</sup> and 1.40 eV,<sup>55</sup> respectively. The relatively large out-of-plane bending modulus of single-layer MoS<sub>2</sub> could be responsible for no significant plastic deformation of substrate was observed at scratch tracks of single-layer MoS<sub>2</sub>. Furthermore, although owing low out-of-plane bending modulus, the plastic deformation of the substrate was not clearly observed at the scratch tracks of single-layer h-BN. In this case, due to the relatively low mechanical strength and highly sensitive to the shear stress of single-layer h-BN, the plastic deformation of substrate might occur either simultaneously with or shortly before the failure of the specimen.

Based on the critical force determined from progressive force scratch test, the adhesion strength to substrate of single-layer h-BN, MoS<sub>2</sub>, and graphene were evaluated. The results show that these atomically thin materials were strongly adhered to their substrates, which in-turn significantly improve the load carrying capacity of the substrate. Furthermore, the effect of surface damage on

topography and friction force of these atomically thin materials were found to be relatively different from each other. In addition, although the plastic deformation of substrate beneath single-layer graphene after scratch tests was commonly observed in previous studies, the defect formation of graphene at scratch track have not been clearly investigated.<sup>69,71</sup> Therefore, due to their distinctive surface damage behaviors toward the failure induced by scratch tests, further understanding surface damage characteristics of single-layer h-BN, MoS<sub>2</sub>, and graphene is essential to properly implement these layered materials as the nanoscale protective coating layers.

### **3.4 Surface damage characteristic of single-layer materials**

After progressive force scratch tests, surface damage characteristics of single-layer h-BN, MoS<sub>2</sub>, and graphene were further investigated using constant force scratch test. In this test, with an aim to observe the evolution of surface damage of single-layer materials with respect to normal force, diamond tip was also employed to scratch a defined area of 1  $\mu\text{m} \times 1 \mu\text{m}$  on the surface of these single-layer materials under given normal forces. The scratched areas were then carefully characterized by AFM and Raman spectroscopy measurements.

#### **3.4.1 Surface damage characteristics of single-layer h-BN**

Topographic and FFM images along with the cross-sectional profiles and friction loops, obtained at scratched areas of single-layer h-BN under various normal forces are shown in Figs. 3.5 (a) and (b), respectively. Based on these AFM images, no significant change in topography and friction was observed at the scratched area under 500 nN normal force. As the normal force increased to 800 nN, although no significant change was observed from topographic image, a few spikes with higher friction force were locally observed along the scratch direction at the FFM image, which indicates that a few surface defects were likely formed at the scratched area. This surface defects were also observed only from the FFM image of the scratched area under 1,200

nN normal force. Furthermore, a few local failures of single-layer h-BN specimen were clearly observed from both topographic and FFM images, where the atomically thin specimen was torn-off and substrate was exposed, leading to a significant friction increase at the failure areas. Finally, single-layer h-BN was totally failed under 1,500 nN normal force (~8.91 GPa contact pressure), where the specimen was torn-off after a few scratches. Furthermore, shortly before the failure of the materials, a small height decrease of about 0.3 nm was observed at the scratched area, while its friction force was not significantly changed. This behavior is likely attributed to the plastic deformation of the underlying SiO<sub>2</sub> substrates, while single-layer h-BN remained unfractured for a few scratches.

Surface damage characteristic of scratched areas were further investigated using Raman spectroscopy. Figs. 3.6 (a), (b), and (c), respectively shows the topographic, LFM images and the corresponding Raman intensity mapping image of  $E_{2g}$  peak ( $\sim 1,370 \text{ cm}^{-1}$ ) of single-layer h-BN specimen after scratch test under various normal forces ranging from 500 nN to 1,200 nN. As shown in Figs. 3.6 (a) and (b), the defect formation and failure of single-layer h-BN can be observed from topographic and FFM images at the scratched areas. While no significant change was observed from the  $E_{2g}$  peak intensity image at those areas, the result suggests that the  $E_{2g}$  peak intensity may not be affected by the defects. This result is similar to the behavior of  $G$  peak obtained from defective graphene, where its intensity was not significantly influenced by the defect.<sup>111</sup> It should be noted that  $E_{2g}$  peak of h-BN and  $G$  peak of graphene are all originated from the  $E_{2g}$  phonon mode, which is the in-plane vibrational mode of B-N atoms and C atoms, respectively.<sup>96</sup>

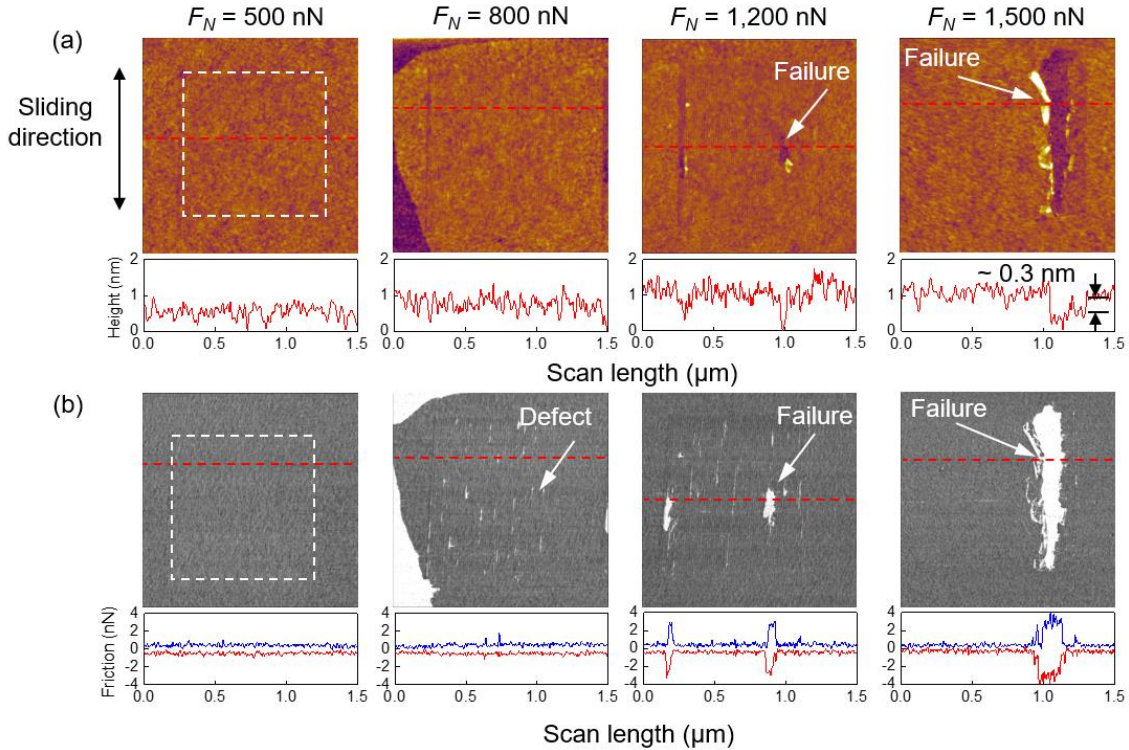


**Fig. 3.5. High resolution (a) topographic and (b) FFM (forward scan) images of single layer h-BN after a constant force scratch test under 500 nN; 800 nN; 1,200 nN; and 1,500 nN normal force. Single-layer h-BN was scratched under a constant normal force at area of  $1 \mu\text{m} \times 1 \mu\text{m}$  as indicated by white dashed square in panel a and b. The cross-sectional profiles and friction loops are included in panel a and b, which demonstrate the change in friction and topography of single layer h-BN due to the constant force scratch test.**

Figs. 3.6 (d) and (e) show Raman spectra and  $E_{2g}$  peak frequency obtained at the scratched areas with respect to the normal force, respectively. The result shows that the  $E_{2g}$  peak frequency, obtained at the scratched areas, shifted to higher frequency (blueshifted) by a relatively small amount ranging from  $0.3 \text{ cm}^{-1}$  to  $0.8 \text{ cm}^{-1}$  compared to that of  $E_{2g}$  peak obtained at the as-exfoliated specimen. In general, compressive strain often produces phonon hardening and tensile strain produces phonon softening, which in turn resulting in blueshift and redshift of the corresponding Raman mode.<sup>29</sup> Therefore, the observed blueshift of  $E_{2g}$  peak is likely attributed to the in-plane compressive strain at the scratched areas induced by the scratch tests. Interestingly, although no

significant change was observed from both topographic and FFM images of scratched area under 500 nN normal force, the Raman spectrum obtained from this area also shows a blueshift  $\sim 0.8 \text{ cm}^{-1}$  of  $E_{2g}$  peak, which indicates that there is a certain degree of compressive strain within the layer. Furthermore, as the normal force increased from 500 nN to 1,200 nN, the blueshift of  $E_{2g}$  peak at those scratched areas were not significantly increased, which implies that the degree of compressive strain at those scratched areas was similar to each other. We speculate that the degree of strain at the scratched areas should be increased as the normal force increased during scratch test, however, due to the defect formation and local failure of the atomically thin specimen, which may effectively relax the accumulated strain in the layer. The defect formation on the surface of scratched single-layer h-BN might be originated from its pure mechanical failure including broken bond generated by the local penetration of AFM tip, or formation of tetrahedron with three B atoms in the plane due to the out-of-plane deformation of N atom during scratch test. The broken bond and tetrahedron defects in single-layer h-BN were predicted to have the lowest formation energy, which are 4.4 eV and 4.3 eV, respectively, while that of Stone-Wales defects was found to be the largest one, around 8.8 eV.<sup>112</sup> That could be the reason why Stone-Wales defects in h-BN have not been experimentally observed.<sup>113</sup>

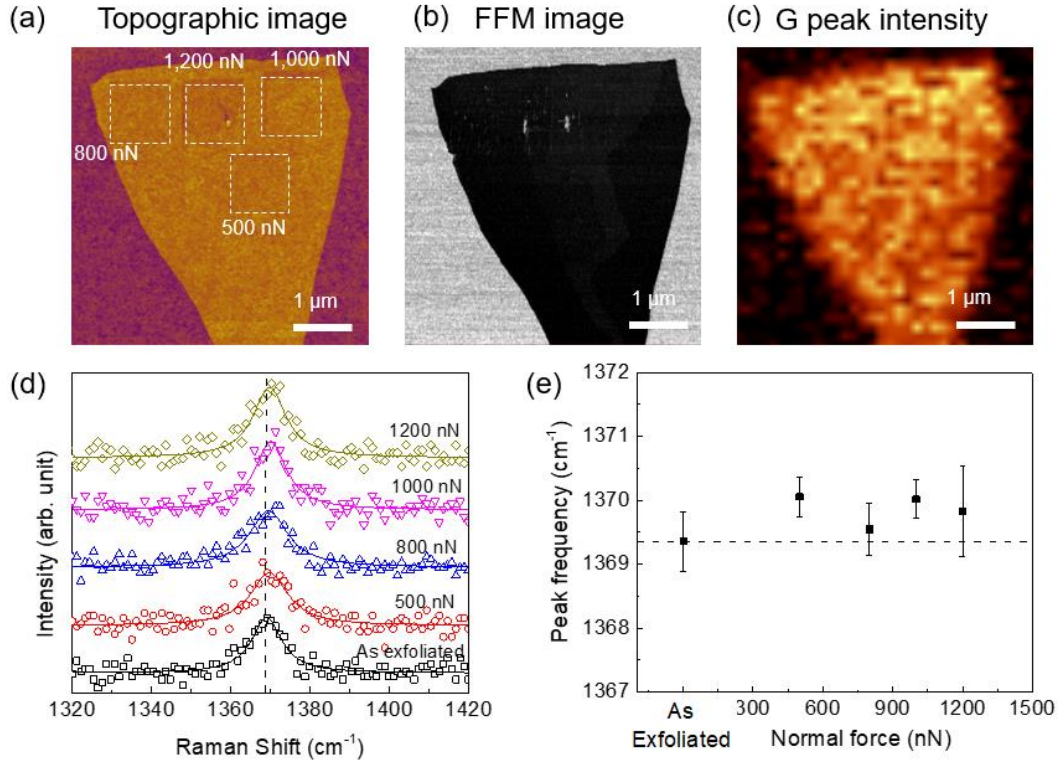


**Fig. 3.6.** (a) Topographic image, (b) FFM image (forward scan), and (c) Raman mapping image with the G peak intensity of single layer h-BN after a constant force scratch test under various normal force ranging from 500 nN to 1200 nN. (d) Raman spectra and (e) summary of frequency of G peak of scratched single-layer h-BN with respect to normal force. Single-layer h-BN was scratched under a constant normal force at the area of  $1\ \mu\text{m} \times 1\ \mu\text{m}$  as indicated by white dashed square in panel a. The Raman spectra were fitted using Lorentzian function and the frequency of G peak from as-exfoliated single-layer h-BN are also denoted as dashed lines for comparison in the panel d and e. Error bar represents one standard deviation.

### 3.4.2 Surface damage characteristics of single-layer MoS<sub>2</sub>

Figs. 3.7 (a) and (b) show topographic and FFM images of single-layer MoS<sub>2</sub> after constant force scratch test under various normal force, respectively. As can be seen that no significant damage was observed from both topographic and FFM images at scratched area under 1,000 nN normal force. As the normal force increased to 1,500 nN, based on the FFM image, a few spikes with higher friction were locally observed at scratched area, while no significant change was found



from the topographic image. This behavior indicates that a few defects were likely formed at the surface of scratched area and resulted in increasing friction force at those areas. Furthermore, surface roughness and friction force of single-layer MoS<sub>2</sub> specimen was found to be significantly increased at the scratched area under 2,000 nN normal force, although the specimen at scratched areas was not torn-off and the substrate was not exposed yet. Therefore, the observed surface roughness and friction increase was likely due to the significant amount of defect formation on top surface of single-layer MoS<sub>2</sub> as the normal force increased. In addition, failure of single-layer MoS<sub>2</sub> specimen was found at the end of the scratched area under 2,000 nN normal force, where the thin film was torn-off and the substrate was clearly exposed. This interesting observation suggests the maximum normal force that single-layer MoS<sub>2</sub> can possibly endure is about 2,000 nN normal force (~ 9.78 GPa contact pressure), prior to the failure. As clearly shown in the topographic and FFM images, single-layer MoS<sub>2</sub> was found to be immediately failed under 2,500 nN normal force.

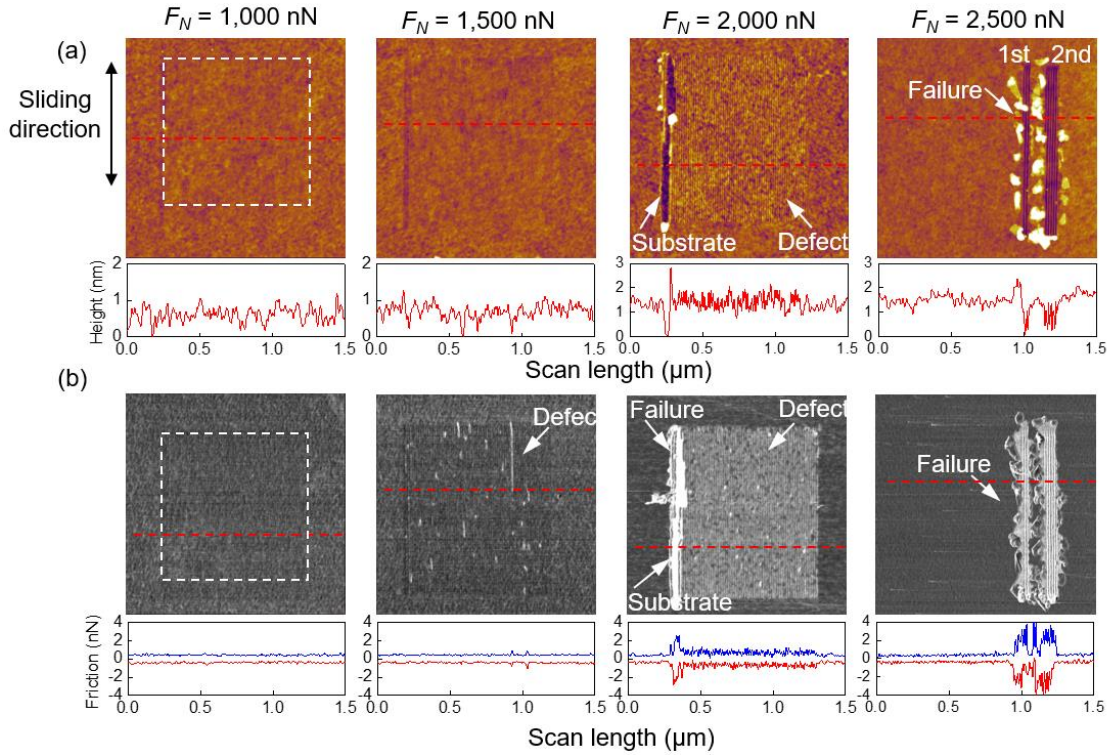


**Fig. 3.7. High resolution (a) topographic and (b) FFM (forward scan) images of single layer MoS<sub>2</sub> after a constant force scratch test under 1,000 nN, 1,500 nN, 2,000 nN, and 2,500 nN normal force. Single-layer MoS<sub>2</sub> was scratched under a constant normal force at the area of 1 μm × 1 μm as indicated by white dashed square in panel a and b. Cross-sectional height profiles and friction loops are included in panel a and b, which demonstrate the change in friction and topography of single layer MoS<sub>2</sub> due to the constant force scratch test.**

Figs. 3.8 (a-d) shows topographic image, FFM image and the corresponding Raman intensity mapping of  $E_{2g}^1$  peak and  $A_{1g}$  peak images of single-layer MoS<sub>2</sub> after scratch tests under 2,000 nN normal force. Based on the topographic and FFM images, defect formation on the surface of specimen was clearly observed. Furthermore, Raman intensity images of  $E_{2g}^1$  peak and  $A_{1g}$  peak clearly show the darker contrast at the scratched areas compared to the unscratched areas. This result indicates that the intensities of  $E_{2g}^1$  peak and  $A_{1g}$  peak at the scratched areas were lower than those at the unscratched areas. Particularly, by comparing the Raman peaks intensity with respect to the normal force as shown in Fig. 3.8 (f), intensities of  $E_{2g}^1$  peak and  $A_{1g}$  peak were found to be

abruptly decreased after scratch test under 2,000 nN normal force. In addition to the intensity, Raman spectra and frequency of Raman peaks obtained the scratched areas under various normal force were shown in Figs. 3.8 (e) and (g), respectively. The results clearly show the blueshift of both  $E_{2g}^1$  peak and  $A_{1g}$  peak obtained at the scratched area under 2,000 nN normal force, compared to the frequency of Raman peaks obtained at the unscratched area. The observed intensity decrease and blueshift of the  $E_{2g}^1$  peak and  $A_{1g}$  peak is likely attributed to the in-plane and out-of-plane compressive strains, respectively, at scratched areas under 2,000 nN normal force.<sup>97,114</sup> In contrast, the intensity and frequency of Raman peaks obtained at the scratched areas under 1,000 nN and 1,500 nN normal force were not significantly changed, which indicates that the degree of compressive strain in the layer was relatively small after scratch tests.

The crystalline quality of single-layer MoS<sub>2</sub> after scratch test was further characterized by Raman spectroscopy based on the frequency separation between  $E_{2g}^1$  peak and  $A_{1g}$  peak,  $\Delta k$ , and the full width at half maximum (FWHM) of  $E_{2g}^1$  peak.<sup>30,33</sup> The value of  $\Delta k$  and  $E_{2g}^1$  peak FWHM were obtained from Raman spectra as shown in Figs. 3.8 (g) and 3.9, respectively. The value of  $\Delta k$  of single-layer MoS<sub>2</sub> after scratch test under 1,000 nN and 1,500 nN normal force were found to be about 18.8 cm<sup>-1</sup> and 18.7 cm<sup>-1</sup>, respectively, which is closed to that of as-exfoliated specimen (~ 18.7 cm<sup>-1</sup>). Furthermore, the  $E_{2g}^1$  peak FWHM of single-layer MoS<sub>2</sub> after scratch test under 1,000 nN and 1,500 nN normal force were found to be around 3.30 cm<sup>-1</sup> and 3.32 cm<sup>-1</sup>, respectively, which also agree with that of as-exfoliated specimen (~ 3.34 cm<sup>-1</sup>). Those results indicate that single-layer MoS<sub>2</sub> was able to sustain good crystalline quality after scratch test under 1,000 nN and 1,500 nN normal force. However, the value of  $\Delta k$  and  $E_{2g}^1$  peak FWHM of single-layer MoS<sub>2</sub> specimen after scratch test under 2,000 nN normal force were determined to be about 19.3 cm<sup>-1</sup> and 3.81 cm<sup>-1</sup>, respectively, which are significantly larger than those of as-exfoliated specimen.

This result further suggests that the crystalline quality of single-layer MoS<sub>2</sub> specimen after scratch test under 2,000 nN normal force was significantly degraded,<sup>30,33</sup> which is likely due to the significant amount of surface defect formation after scratch test.

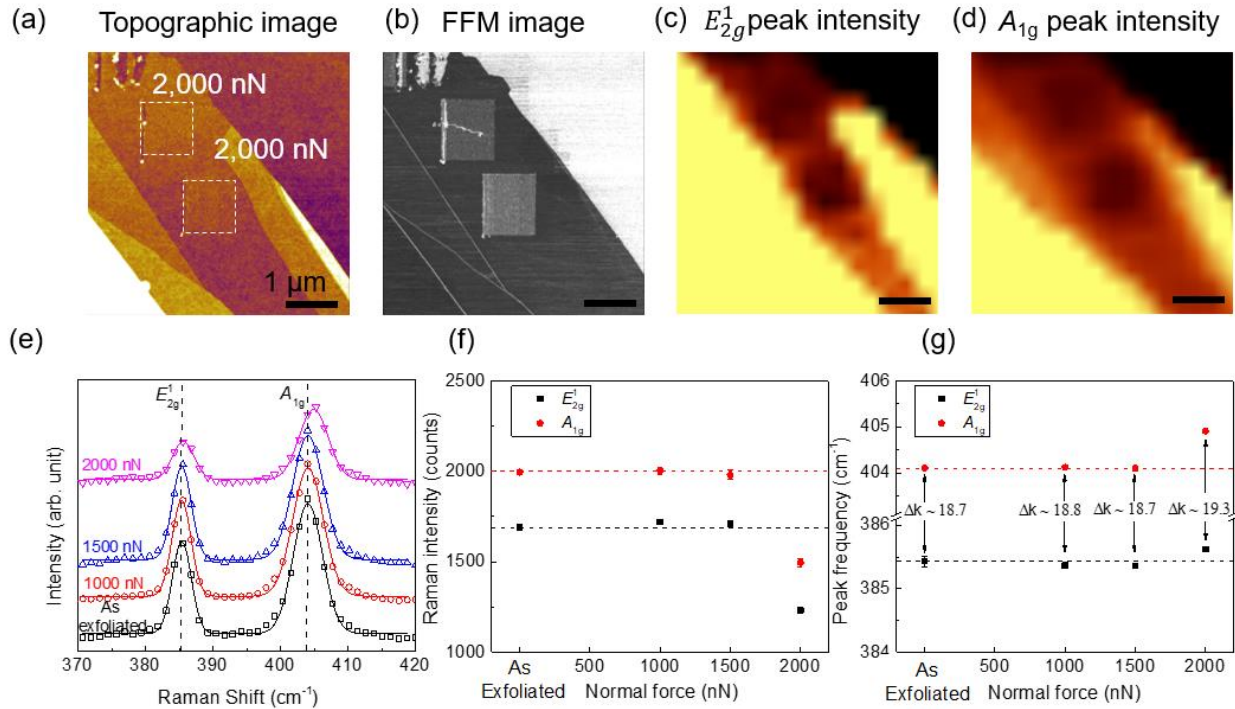


**Fig. 3.8.** (a) Topographic image, (b) FFM image (forward scan), and Raman mapping images with (c)  $E_{2g}^1$  and (d)  $A_{1g}$  peaks intensity of single layer MoS<sub>2</sub> after a constant force scratch test under 2,000 nN normal force. (e) Raman spectra, and summary of (f) intensity, and (g) frequency of  $E_{2g}^1$  and  $A_{1g}$  peaks of scratched single-layer MoS<sub>2</sub> with respect to normal force. Single-layer MoS<sub>2</sub> was scratched under a constant normal force at the area of 1 μm × 1 μm as indicated by white dashed square in panel a. Raman spectra were fitted using Gaussian function. In panel e, f, and g, the frequency and intensity of the  $E_{2g}^1$  and  $A_{1g}$  peaks from the as-exfoliated single layer MoS<sub>2</sub> are also denoted as dashed lines for comparison. Error bar represents one standard deviation.

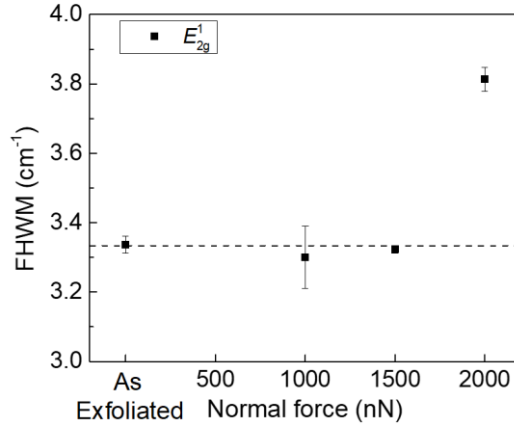


**Fig. 3.9.** The Raman  $E_{2g}^1$  peak FWHM of scratched single-layer MoS<sub>2</sub> with respect to normal force. The  $E_{2g}^1$  peak FWHM from the as-exfoliated single layer MoS<sub>2</sub> is denoted as dashed lines for comparison. Error bar represents one standard.

In general, surface defect of atomically thin MoS<sub>2</sub> could occur from different surface treatment conditions including particle adsorption on top surface of MoS<sub>2</sub> due to high laser power treatment,<sup>89</sup> oxygen chemical adsorption at crack sites of single-layer MoS<sub>2</sub> due to high temperature annealing,<sup>115</sup> and wrinkle formation on top surface of multi-layer MoS<sub>2</sub> due to the combination of compressive stress and shear.<sup>77</sup> The defect that was formed at scratched areas in our case is likely attributed to the wrinkle formation on top surface of single-layer MoS<sub>2</sub>. Due to the large contact pressure during scratch test, single-layer MoS<sub>2</sub> was compressed and the top surfaces in the area beneath the tip become wrinkled as the tip scratched across the surface, resulting in surface roughness and friction force increase of the scratched areas. The wrinkle formation on the surface of single-layer MoS<sub>2</sub> is similar to what was observed in the case of few-layer MoS<sub>2</sub>.<sup>77</sup> However, based on the study of Barboza et al, it should be noted that such wrinkle formation was proposed to be observed only in the case of few-layer MoS<sub>2</sub>,<sup>77</sup> where the layer-substrate interactions were insignificant. And therefore, wrinkle formation on the surface of single-layer MoS<sub>2</sub> was not observed within their relatively small normal force, ranging from 10 nN to 391 nN. In our work, due to the large interaction between single-layer MoS<sub>2</sub> and substrate, wrinkle

formation was only observed at the scratched areas under normal force of at least 1,500 nN (~ 8.91 GPa contact pressure).

Furthermore, the oxidation of single-layer MoS<sub>2</sub> was also put into consideration due to the possibility of high temperature generated at the contacting interface between AFM tip and single-layer materials during scratch test. This high temperature could lead to the formation of Mo-O bonding at the scratched areas due to the oxygen chemical adsorption at crack sites of single-layer MoS<sub>2</sub> at high temperature.<sup>115</sup> However, based on the Raman spectra obtained from the scratched areas, the oxidation of MoS<sub>2</sub> is not likely occur due to the lack of the Raman peak at around 820 cm<sup>-1</sup>, which is often referred as the Raman signature of oxidized MoS<sub>2</sub>.<sup>37,116</sup> In addition, Haiyan Nan et al.<sup>115</sup> recently observed the strong photoluminescence (PL) enhancement of single-layer MoS<sub>2</sub> at the defects formed during the thermal annealing with high temperature. In that work, they demonstrated that the oxygen chemical adsorption at defect sites, which is resulted in Mo-O bonding, is the main reason for the significant enhancement of both PL A- and B-excitons at defect sites of single-layer MoS<sub>2</sub>. From the PL spectra of single-layer MoS<sub>2</sub>, the strong A exciton (~ 1.84 eV) and the weaker B exciton (~ 1.98 eV) arise from the direct transition at the K and K' point in the Brillouin zone, respectively.<sup>117</sup> Fig. 3.10 (a) shows the PL A-exciton intensity mapping of single-layer MoS<sub>2</sub> after scratch tests under 2,000 nN normal force. Based on the different contrast form inside and outside of the scratched areas in the PL image, the decrease in intensity clearly observed from the scratched areas under 2,000 nN normal force. Furthermore, the PL spectra obtained at scratched areas under various normal force as shown in Fig. 3.10 (b) demonstrates the gradually decreasing in PL intensity of A- and B-excitons of scratched single-layer MoS<sub>2</sub> with the increasing normal force. The significant PL decrease indicate the absence of Mo-O bonding

induced by chemically adsorbed oxygen at scratched areas, hence single-layer MoS<sub>2</sub> might be not oxidized during the scratch test.

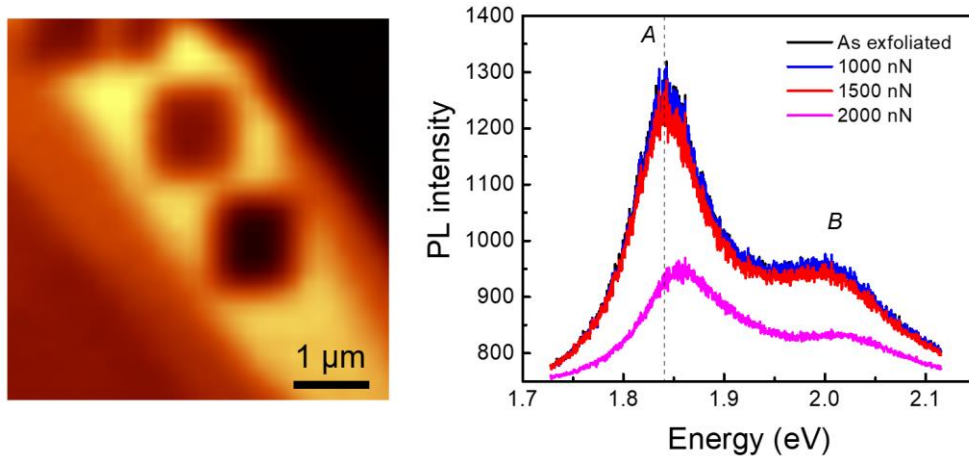


**Fig. 3.10. (a) Photoluminescence (PL) intensity image of single layer MoS<sub>2</sub> after constant force scratch test under 2,000 nN normal force. (b) PL spectra of scratched single-layer MoS<sub>2</sub> with respect to normal force. In panel b, the energy of the A exciton of as-exfoliated single layer MoS<sub>2</sub> was noted as dashed line for comparison.**

### 3.4.3 Surface damage characteristics of single-layer graphene

Figs. 3.11 (a) and (b) show the topographic and FFM images of single-layer graphene after constant force scratch test under various normal force, respectively. Based on the AFM images, no significant change was observed at the scratched area under normal force of 1,000 nN. A height decrease of about 1.0 nm was observed from the topographic image of scratched area under 3,000 nN normal force. As the normal force increased from 4,000 nN to 5,000 nN, the height gradually decreased from 1.5 nm to 1.6 nm, respectively, prior to the failure. While no significant change in frictional behavior was observed at any scratched areas. These behaviors indicate that the underlying substrate was plastically deformed due to large contact pressure induced by scratch test, and the degree of plastic deformation increased as the normal force increased. The maintained low friction force at the scratched areas shows that single-layer graphene could endure the scratch test

and cover the plastically deformed substrate, up to 5,000 nN normal force ( $\sim 13.21$  GPa contact pressure). The results clearly demonstrate the remarkable load carrying capacity of single-layer graphene. Furthermore, the plastic deformation of substrate and following by failure of single-layer graphene under sufficient contact pressure was also consistent with the results from progressive force scratch test of atomically thin graphene.

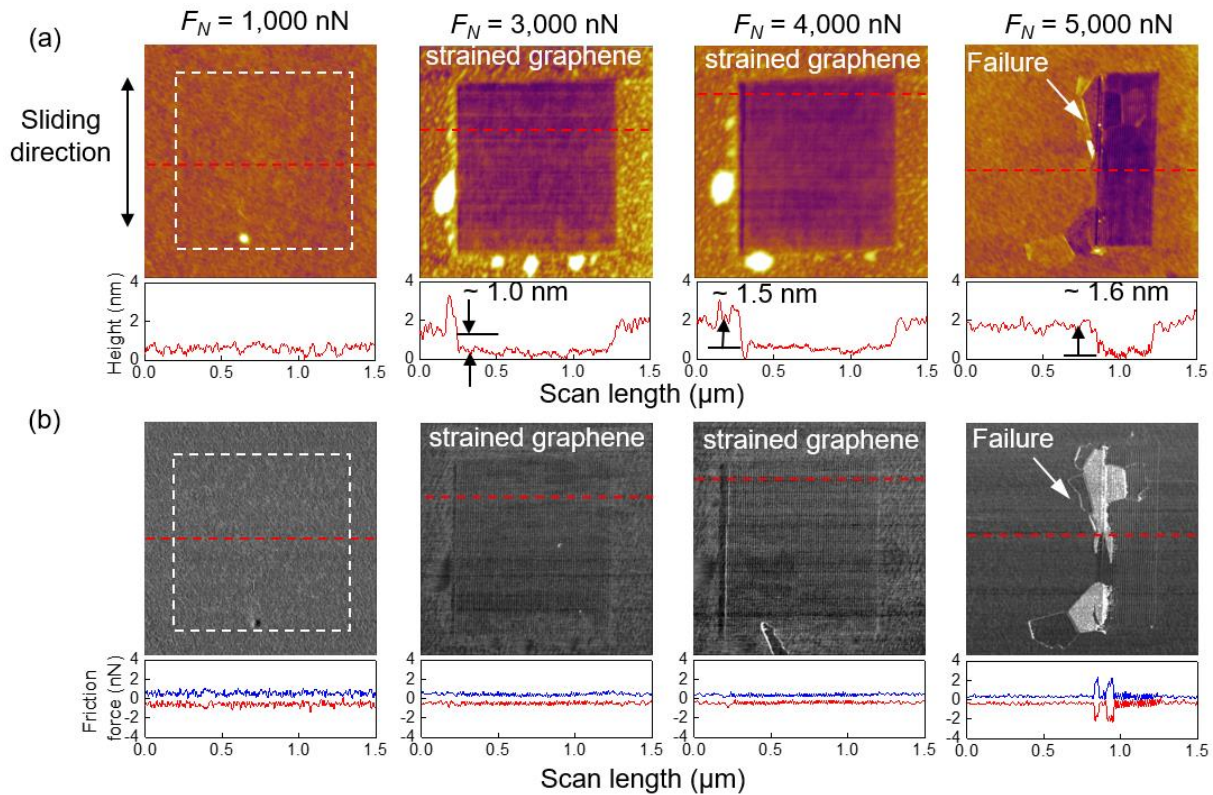


**Fig. 3.11. High resolution (a) topographic and (b) FFM (forward scan) images of single layer graphene after a constant force scratch test under (from left to right) 1,000 nN, 3,000 nN, 4,000 nN, and 5,000 nN normal force. Single-layer graphene was scratched under a constant normal force at the area of  $1 \mu\text{m} \times 1 \mu\text{m}$  as indicated by white dashed square in panel a and b. Cross-sectional height profile and friction loop are included in panel a and b, which demonstrate the change in friction and topography of single-layer graphene due to the constant force scratch test.**



Figs. 3.12 (a) and (b) show the topographic images, FFM images and the corresponding Raman intensity mapping of D peak and 2D peak images of single-layer graphene after constant force scratch test under various normal force ranging from 800 nN to 2,400 nN and from 3,000 nN to 5,000 nN, respectively. D peak ( $\sim 1350 \text{ cm}^{-1}$ ) corresponds to the breathing mode of six-atoms rings and is only activated by the defects.<sup>98</sup> Although no defect is required for the activation of 2D peak of single-layer graphene, 2D peak intensity was also found to be strongly influenced by the defects.<sup>118</sup> Hence, based on D peak and 2D peak of single-layer graphene after scratch test, the defect formation could be clearly observed. As shown in the AFM images, topography of single-layer graphene started to change due to the plastic deformation of substrate after scratch test under 1,400 nN normal force ( $\sim 8.72 \text{ GPa}$  contact pressure). As the normal force increased, the degree of plastic deformation of substrate increase, which in turn greatly affects to the topography of single-layer graphene. In contrast, no significant change in friction force of scratched areas were observed. The corresponding Raman intensity mapping images of D peak and 2D peak of single-layer graphene after scratched areas various normal forces are shown in Figs. 3.12 (a) and (b). Based on difference in contrast from the Raman intensity image of D peak and 2D peak, in which the brighter (darker) contrast indicates the higher (lower) intensity, defect formation in single-layer graphene could be clearly identified. According to these Raman intensity images, a relatively large amount of defect was observed from the edge of single-layer graphene, as expected.<sup>98</sup> Furthermore, no significant change was observed from the scratched areas under 800 nN normal force, which suggests the absence of a significant amount of defect at those areas. The increase in intensity of D peak and decrease in intensity of 2D peak were clearly observed at scratched areas under normal force ranging from 2,200 nN to 5,000 nN, which indicates that the defect was formed at those scratched areas.

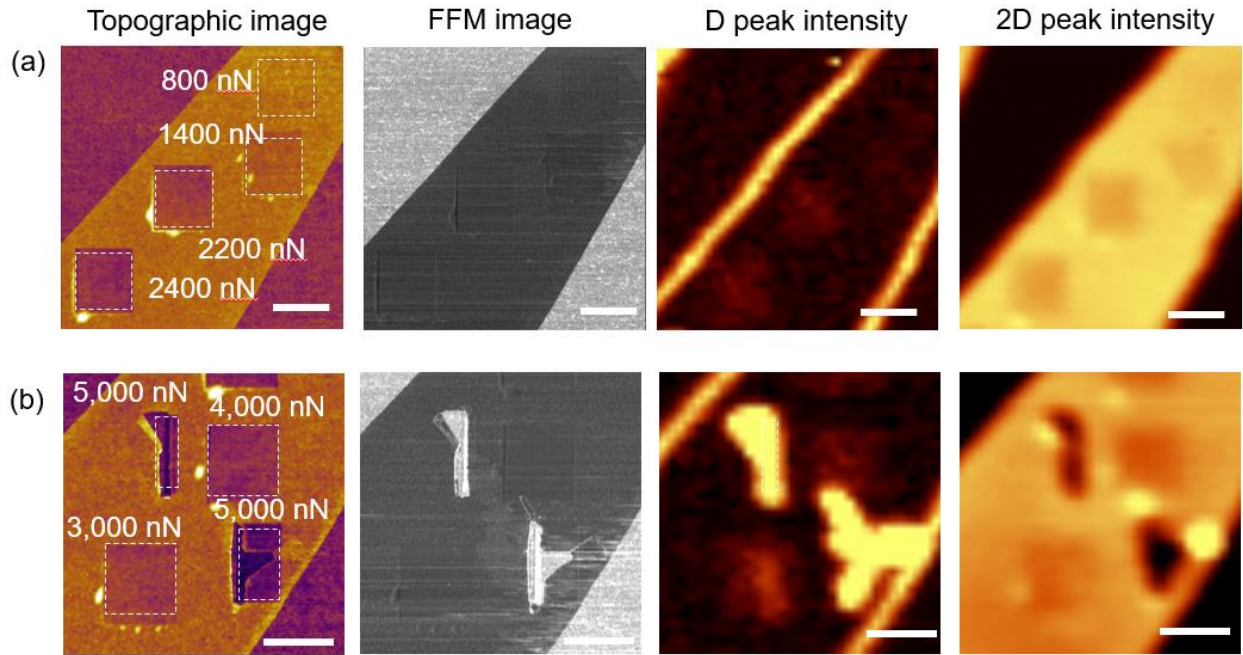


**Fig. 3.12.** Topographic image, FFM image (forward scan), and Raman mapping images with the D and 2D peaks intensity of single layer graphene after a constant force scratch test under various normal force ranging (a) from 800 nN to 2,400 nN and (b) from 3,000 nN to 5,000 nN. Single-layer graphene were scratched under a constant normal force at the area of  $1 \mu\text{m} \times 1 \mu\text{m}$  as indicated by white dashed square in panel a and b.

The variation of intensity of D peak and 2D peak with respect to the normal force as shown in Fig. 3.13 (c), clearly shows that, as the normal force increased, the intensity of D peak increased and the intensity of 2D peak increased. The result further suggests that as the normal force increased, the amount of defect formed at scratched area of single-layer graphene increased, prior to the failure. It should be noted that the relatively high intensity of D peak observed at the scratched areas under 5,000 nN is likely attributed to the defects at the edges of single-layer graphene, which were formed by the failure of the materials.

Furthermore, with an aim to roughly estimate the defect density at the scratched areas, the Tuinstra-Koenig relation was employed:<sup>119</sup>

$$L_D = [2.4 \times 10^{-10} \text{ nm}^{-3}] \cdot \lambda^4 \cdot (I_D/I_G)^{-1}$$

, where  $L_D$  is the distance between point-like defects and  $\lambda$  is Raman excitation wave length ( $\sim 532$  nm).<sup>120,121</sup> At the scratched areas under 2,200 nN and 4,000 nN normal force, the intensity ratio  $I_D/I_G$  was determined to be about 0.45 and 0.48, respectively. Hence, based on the Tuinstra-Koenig relation, the distance between defects formed at the scratched areas under 2,200 nN and 4,000 nN normal force were estimated to be about 42.22 nm and 40.82 nm, respectively. This result suggests that as the normal force increased, the density of the defect at the scratched area was increased. Although the defect formation was observed at the tested area, according to the previous studies, these estimated values of  $L_D$  also indicate that scratched areas have a relatively low defect density ( $L_D \geq 10$  nm).<sup>120,122</sup> Considering that frictional behaviors of the atomically thin materials are presumably sensitive to surface defects, where friction increases with increasing defect formation like the case of atomically thin h-BN and MoS<sub>2</sub>, the relatively low defect density at the scratched single-layer graphene could be responsible for no significant change in friction was observed, even right before the failure occurred.

Raman spectra of G peak and 2D peak obtained at scratched areas under various normal force, as shown in Fig. 3.13 (a), clearly demonstrate the blueshift G peak at those scratched areas, while the frequency of 2D peak was not significantly changed. The blueshift of G peak is likely attributed to the in-plane compressive strain of single-layer graphene at scratched areas.<sup>123</sup> Furthermore, based on the variation of G peak frequency with respect to normal force at the scratched areas as depicted in Fig. 3.13 (b), the degree of blueshifted G peak generally increased with increasing normal force, which suggests the in-plane compressive strain at scratched areas generally increased as the normal force increased. Interestingly, at scratched areas under 800 nN normal force, G peak blueshifted by about  $1.6 \text{ cm}^{-1}$ . This result indicates a certain amount of compressive strain at that scratched area, although no significant change in topography and friction was observed.

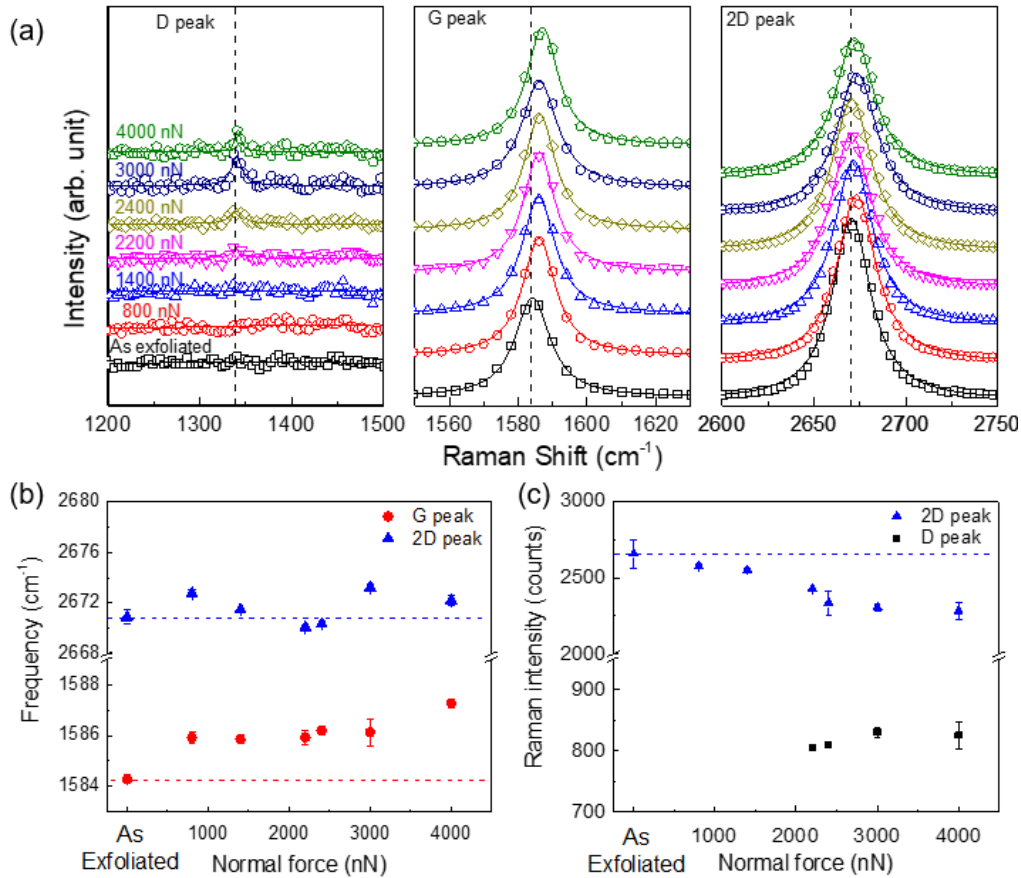


**Fig. 3.13.** (a) Raman spectra, and summary of (a) frequency and (c) intensity of G, and 2D peaks of scratched single-layer graphene with respect with respect to normal force. The Raman spectra in panel a were fitted using Lorentzian function. The frequency and the intensity of the D, G and 2D peaks from the as-exfoliated single layer graphene are also denoted as dashed lines for comparison in the panel a, b, and c. Error bar represents one standard deviation.

Based on the Raman study of disorder graphite, a three-stage classification of disorder along an *amorphization trajectory* ranging from graphite to tetrahedral amorphous carbon (ta-C) was proposed, including: (1) graphite to nano-crystalline graphite; (2) nano-crystalline graphite to amorphous carbon (a-C,  $\sim 20\% \text{ sp}^3$ ); and (3) a-C to ta-C ( $> 85\% \text{ sp}^3$ ).<sup>124</sup> In this study of single-layer graphene, based on the Raman spectra of D peak and G peak obtained at the scratched areas with respect to normal force, only stage 1 is likely the most relevant.<sup>122</sup> In this stage, which is the

transformation from single-crystalline graphene to nanocrystalline graphene due to scratch test under 4,000 nN normal force, the evolution of Raman spectrum are as follow:<sup>122,124</sup> (1) D peak appeared and the intensity ratio  $I_D/I_G$  increased; (2) G peak frequency increased (blueshifted) from 1584.11  $\text{cm}^{-1}$  to 1587.23  $\text{cm}^{-1}$ ; and (3) there was no dispersion of G peak. It is well established that pristine single-crystalline graphene is claimed to be the strongest material, however, defective nano-crystalline graphene is proposed to have a significant degradation in its mechanical toughness and strength.<sup>47</sup> Therefore, the degradation in mechanical properties of single-layer graphene specimen due to defect formation could potentially affect its tribological performance as a protective and solid lubricant coating layers. For instance, with the large amount of the pre-existing defects at the edges, this could be the reason why the single-layer graphene at the edge area was found to be easily failed under a much smaller normal force ( $\sim 2$  orders of magnitude smaller), compared to the case of graphene at the interior area.<sup>71</sup>

Based on the constant force scratch test results, surface damage characteristics of single-layer h-BN, MoS<sub>2</sub>, and graphene were systematically investigated. The evolution of surface damage of these single-layer materials can be defined as the multi-stage layer removal process, which may be initiated from: (i) the elastic deformation to (ii) the plastic deformation of the single-layer material-substrate system along with the defect formation and propagation within the structure of single-layer materials and finally to (iii) the total removal of the single-layer materials and expose of the substrate. At stage (i), the single-layer materials remained intact with no significant defect formation after scratch test under relatively small normal force. Therefore, at this stage, these single-layer materials could provide their best tribological performance for very long period of time. Stage (ii) was initiated when the defects were significantly formed along with the plastic deformation of the substrate at scratched areas as the normal force increased. Although the failure

of the single-layer materials may not occur at this stage yet, however, the topography, friction force as well as the crystalline quality and mechanical strengths of single-layer h-BN, MoS<sub>2</sub> and graphene were permanently and differently affected due to their own types of defect, leading to the potential degradation of their tribological performances.

The observed residual compressive strains at scratched areas could further indicate the failure mechanisms at stage (iii) of single-layer h-BN, MoS<sub>2</sub>, and graphene during scratch test. In general, compressive strain and the tensile strain could occur simultaneously during the scratch test due to the friction force between the scratching tip and the surface of single-layer materials. Particularly, the compressive strains and tensile strains were originated from the pushing force in front of the tip, and from the pulling force behind the tip, respectively, regardless the scratching direction of the tip. The schematic of the scratched atomically thin specimen is shown in the Fig. 3.14, where the single-layer materials was compressed at the buckling region in front of the tip, while was simultaneously stretched at the area behind of the tip. The dominance of the compression or tension acted on the atomically thin materials during scratch test would strongly affect their mechanical instability, and therefore their failure mechanisms. Recently, single-layer graphene have been proposed to exhibit a highly asymmetry in strain induced mechanical instability, where the critical compressive strains for buckling instability have been found to be significantly smaller than the critical tensile strains for fracture. In particular, the buckling formation was found just under about  $10^{-4}$  % compressive strain, whereas the tensile strain for fracture was determined about 2%.<sup>125</sup> And such a highly asymmetry in strain induced mechanical instability is expected for most of 2D materials from single to a few number of layers.<sup>126</sup> This observation indicates that these single-layer materials are extremely unstable against compressive strains. Based on the blueshift of the Raman characteristic peaks observed at the scratched areas of single-layer h-BN, MoS<sub>2</sub> and

graphene, compared to the tensile strain, the compressive strains induced by the scratch test is likely to be more dominant. Under compression, two types of mechanical instabilities would be induced, which are buckling and fracture. In particular, the compressive strains will first induce buckling preempting fracture under relatively small normal force, and then, the compressive strains increased with increasing normal force, the atoms bonds in the materials were further compressed and eventually rupture.<sup>79,126</sup> Which could be considered as the failure mechanism of single-layer h-BN, MoS<sub>2</sub> and graphene induced by scratch test.

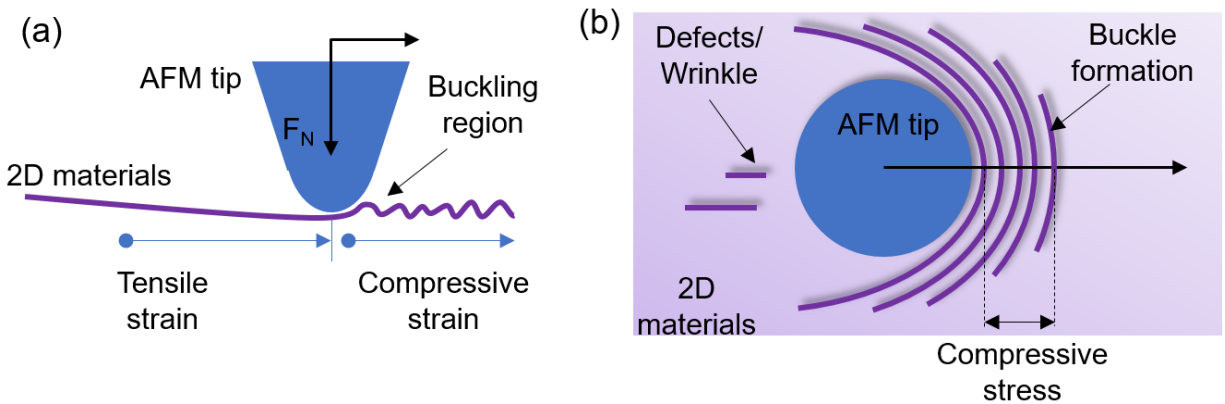


**Fig. 3.14. Schematic illustrating the buckling region in front of the sliding AFM tip from (a) side view and (b) plane view during scratch test.**

### 3.5 Effect of number of layers on surface damage characteristics

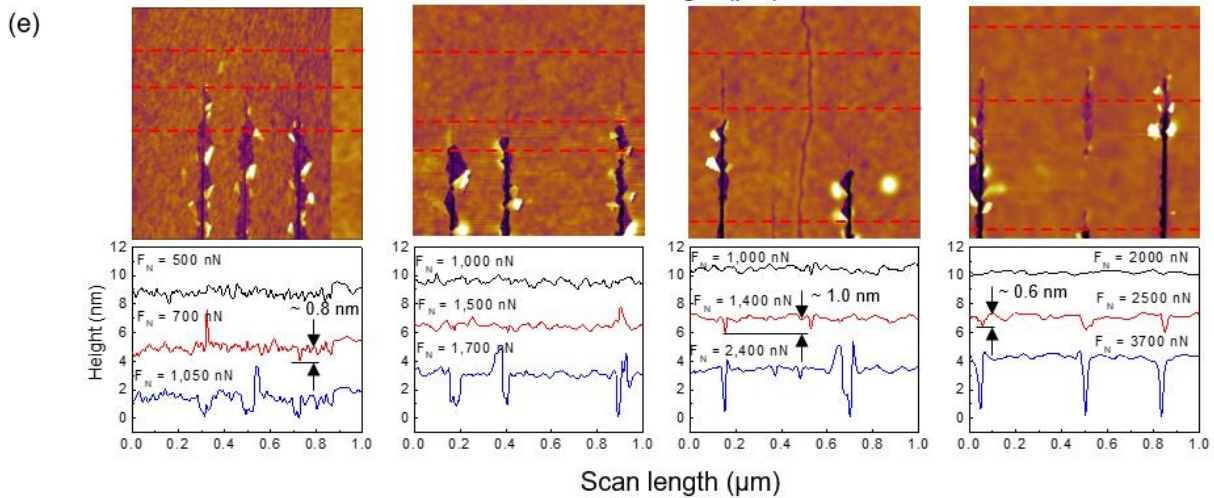
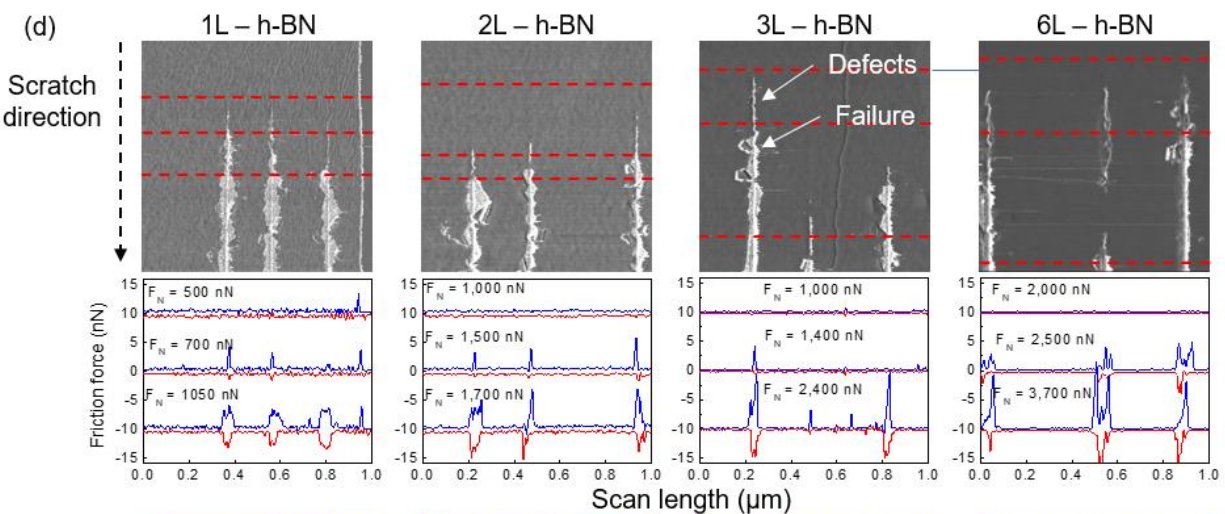
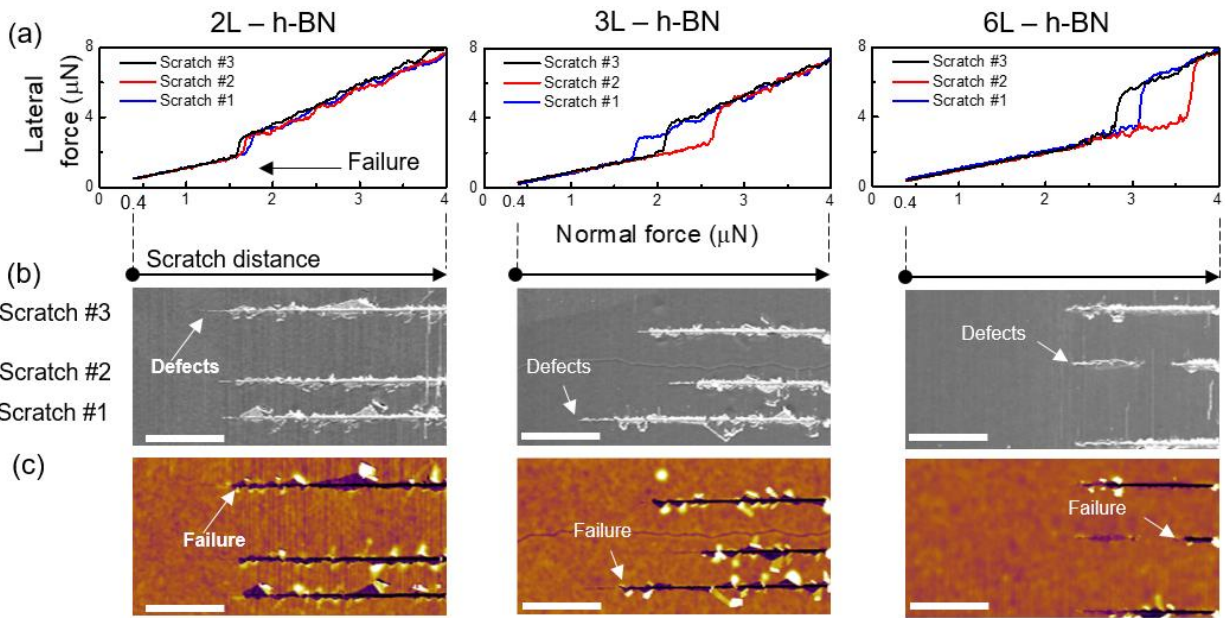
It was proposed that thicker graphene could provide better tribological performance than the thinner one.<sup>69</sup> However, the mechanism of this enhancement of tribological performance of graphene have not been clearly explained. Therefore, the effect of number of layer on tribological performance of atomically thin h-BN, MoS<sub>2</sub> and graphene was further investigated. Considering that the adhesion strengths to the substrates of these atomically thin materials would significantly affect their tribological performances, hence the progressive force scratch test was further

conducted on bi-layer, tri-layer, and multi-layer h-BN, MoS<sub>2</sub> and graphene with an aim to investigate the effect of number of layers on their adhesion strengths to substrate.

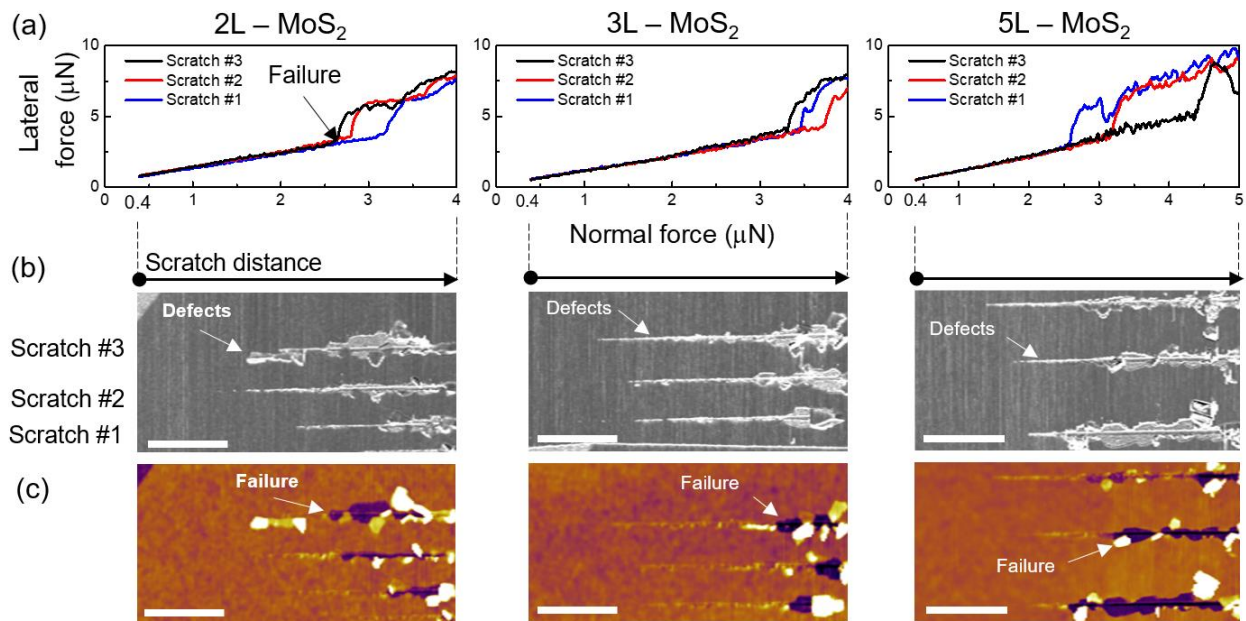
### **3.5.1 Adhesion strength to the substrate of multi-layer**

The lateral force variation with respect normal force during progressive force scratch test, and the corresponding topographic and FFM images of scratch tracks of atomically thin h-BN, MoS<sub>2</sub>, and graphene were shown in Figs. 3.15 (a-c), 3.16 (a-c), and 3.17 (a-c), respectively. By matching those images like the case of single-layer materials, the critical forces of these atomically thin h-BN, MoS<sub>2</sub> and graphene were determined and summarized with respect to number of layer as demonstrated in Fig. 3.18 (a). It should be noted that, the critical forces of single-layer materials were also included in Fig. 3.18 (a) for comparison. The result clearly shows that as number of layers of h-BN, MoS<sub>2</sub>, and graphene increased, the critical force of these atomically thin materials generally increased. This result indicates that the adhesion strength to substrate of single- and a few-layer h-BN, MoS<sub>2</sub> and graphene generally increased with the increasing number of layers. This behavior may be attributed to the van der Waals interactions of the substrate with not only its nearest layer, but also other above layers as shown in Fig. 3.18 (c), hence the bonding of atomically thin materials to underlying substrate increased as the number of layers increased.





**Fig. 3.15. Progressive force scratch test results of bi-, tri-, and multi-layer h-BN. (a) Lateral force variation with respect to normal force during progressive force scratch tests. (b) FFM images (forward scans), and (c) topographic images of scratch tracks after progressive force scratch tests. High resolution (d) FFM images (forward scans) and (e) topographic images of scratch tracks formed at single- and multi-layer h-BN after progressive force scratch tests. In panel b, the scratch distance of about 2  $\mu\text{m}$  was also noted. In panel b and c, scale bars: 500 nm. Friction loops and cross-sectional profiles are included in panel d and e, respectively. Red dashed lines indicate the location and the corresponding normal force during scratch test, where friction loops and cross-sectional profile are taken.**



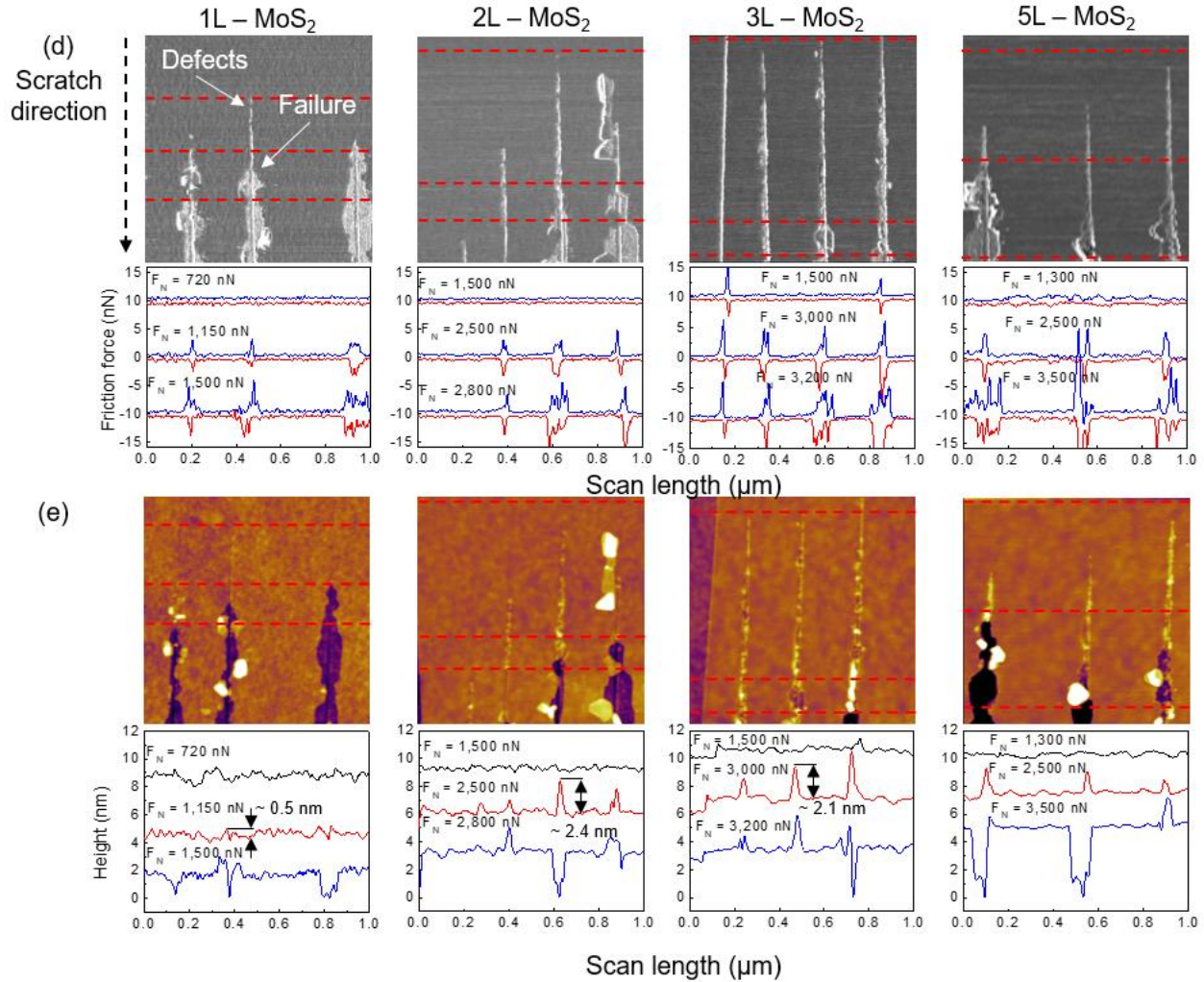


**Fig. 3.16. Progressive force scratch test results of bi-, tri-, and multi-layer MoS<sub>2</sub>.** (a) Lateral force variation with respect to normal force during progressive force scratch tests. (b) FFM images (forward scans), and (c) topographic images of scratch tracks after progressive force scratch tests. High resolution (d) FFM images (forward scans) and (e) topographic images of scratch tracks formed at single- and a multi-layer MoS<sub>2</sub> after progressive force scratch tests. In panel b, the scratch distance of about 2 μm was also noted. In panel b and c, scale bars: 500 nm. Friction loops and cross-sectional profiles are included in panel d and e, respectively. Red dashed lines indicate the location and the corresponding normal force during scratch test, where friction loops and cross-sectional profile are taken.

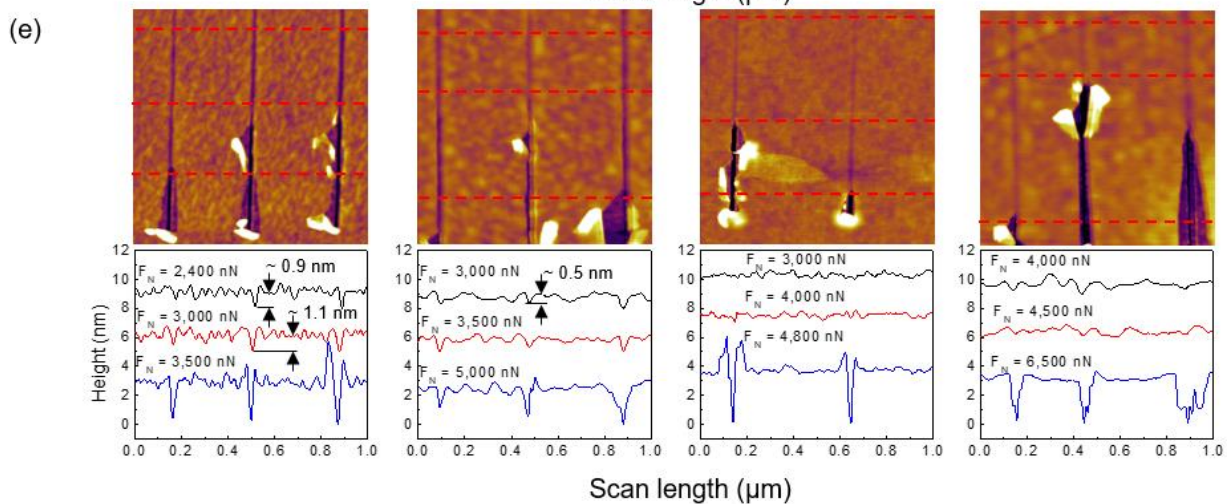
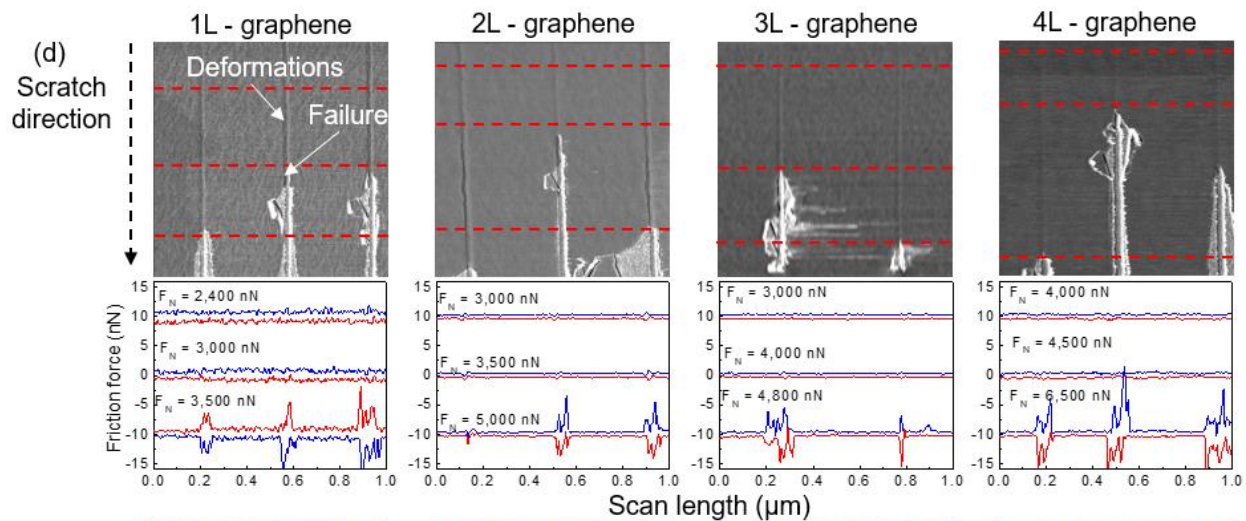
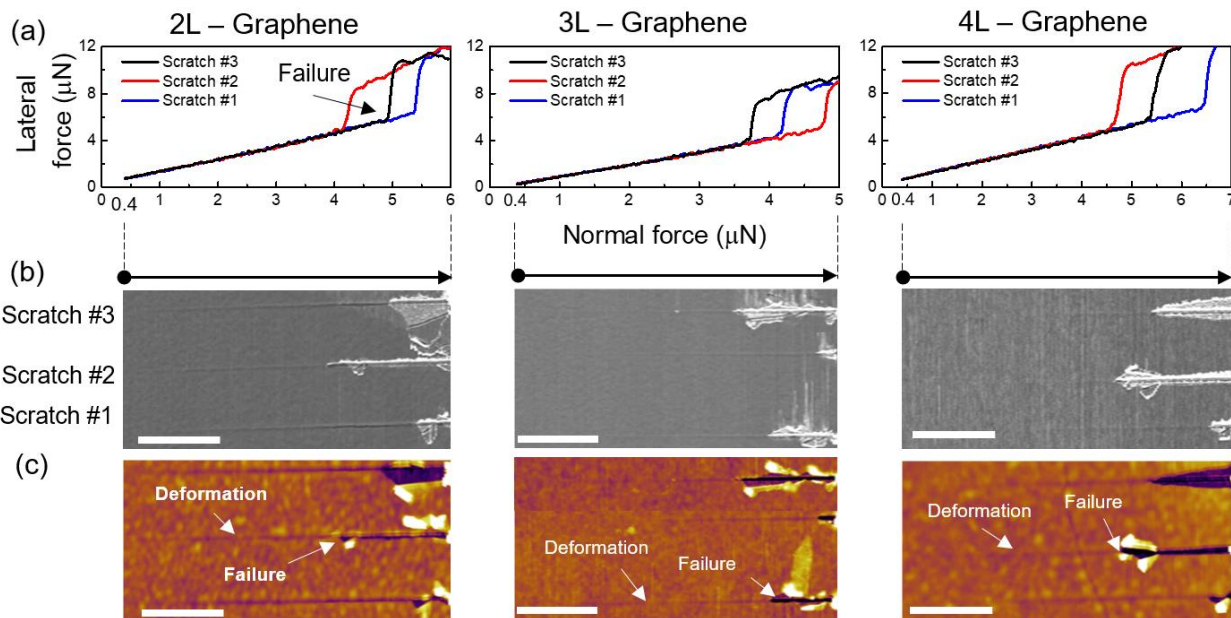


**Fig. 3.17. Progressive force scratch test results of bi-, tri-, and multi-layer graphene. (a) Lateral force variation with respect to normal force during progressive force scratch tests. (b) FFM images (forward scans), and (c) topographic images of scratch tracks after progressive force scratch tests. High resolution (d) FFM images (forward scans) and (e) topographic images of scratch tracks formed at single- and multi-layer graphene after progressive force scratch tests. In panel b, the scratch distance of about 2  $\mu\text{m}$  was also noted. In panel b and c, scale bars: 500 nm. Friction loops and cross-sectional profiles are included in panel d and e, respectively. Red dashed lines indicate the location and the corresponding normal force during scratch test, where friction loops and cross-sectional profile are taken.**

The high resolution topographic and FFM images of scratch tracks on single- and a few-layer h-BN, MoS<sub>2</sub> and graphene were shown in Figs. 3.15 (d, e), 3.16 (d, e), and 3.17 (d, e), respectively. The topographic images clearly show the failure of single- and a few-layer h-BN and MoS<sub>2</sub> along with the expose of SiO<sub>2</sub> substrates shortly after the formation of scratch tracks on top surface of these atomically thin materials. Furthermore, shortly prior to the failure of the atomically thin h-BN and MoS<sub>2</sub>, the friction increase was also clearly observed at the scratch tracks, which is likely attributed to the defect formation on the surface of these atomically thin materials. Interestingly, defect formation at scratch tracks affected differently to topography of atomically thin h-BN and MoS<sub>2</sub>, shortly prior to the failure of the materials. For instance, based on the topographic image of scratch tracks formed in the surface of tri-layer h-BN under 1,400 nN normal force as shown in Fig. 3.15 (e), a height decrease of about 1 nm was clearly observed at the first scratch track. While in case of atomically thin MoS<sub>2</sub>, a height increase of about 2.1 nm were observed from the second scratch track formed in the surface of tri-layer MoS<sub>2</sub> under 3,000 nN normal force, as shown in Fig. 3.16 (e). In the case of atomically thin graphene, based on the topographic images as shown in Fig. 3.17 (e), a height decrease at scratch tracks with increasing normal force was observed, prior to the failure. For instance, single-layer graphene exhibited a height decrease of about 0.9

nm and 1.1 nm under 2,400 nN and 3,000 nN normal force, respectively, prior to the failure. Interestingly, the corresponding FFM images from Fig. 3.17 (d) show that the scratch tracks of graphene could maintain its low frictional behavior, until the failure occurred. The height decrease observed at scratch tracks on single- and a few-layer h-BN and graphene is likely attributed to the plastic deformation of the underlying SiO<sub>2</sub> substrate. By owing the relatively low out-of-plane bending modulus, atomically thin h-BN and graphene was out-of-plane deformed during scratch test, which resulting in the deformation of the underlying substrate. However, due to the relatively low mechanical strength, surface of single- and a few-layer h-BN was found to be damaged almost simultaneously with the deformation of the substrate. The surface damaged of atomically thin h-BN may cause friction increase at the scratch tracks, shortly prior to the failure. In contrast, single- and a few-layer graphene was able to endure the plastically deformed substrate prior to the failure, without any significant change in friction of scratch tracks. This great endurance of atomically thin graphene during scratch test may be inherited from its superior mechanical strength. In the case of single- and a few-layer MoS<sub>2</sub>, due to the relatively large out-of-plane bending stiffness which are many times larger than those of atomically thin h-BN and graphene, atomically thin MoS<sub>2</sub> were not significantly out-of-plane deformed during scratch tests, hence no significant plastic deformation of the underlying substrate was found at scratch tracks. Instead of that, the height increased observed at scratch tracks is likely attributed to the wrinkle formation at the top surface of atomically thin MoS<sub>2</sub> during scratch test, which leads to the friction increase at the scratch tracks, prior to the failure. The occurrence of wrinkle formation or plastic deformation at scratch tracks of atomically thin h-BN, MoS<sub>2</sub>, and graphene and their effects on topography and friction at those areas, prior to the failure of these atomically thin materials are consistent with what were observed from single-layer materials.

Furthermore, considering  $F_d$  as the normal force required to induce surface damages including wrinkle formation and plastic deformation at scratch tracks of single- and a few-layer h-BN, MoS<sub>2</sub>, and graphene during progressive force scratch tests. Due to the significant effect of these surface damages induced by scratch tests on the topography, friction force, as well as mechanical strengths of these atomically thin materials at scratched areas, the determination of  $F_d$  is as important as that of critical force ( $F_c$ ). The variation of  $F_d$  with respect to number of layers of h-BN, MoS<sub>2</sub>, and graphene as summarized in Fig. 3.18 (d) clearly shows that the value of  $F_d$  generally increased with the increasing number of layers. This increase in value of  $F_d$  indicates that as the number of layer increased, the occurrence of surface damages at scratch tracks was likely to be more delayed. As it is reported for layered material subject to an indentation test, the thicker the specimen is, the harder it is to deform,<sup>6,7</sup> which is likely attributed to the increasing of bending modulus with the increasing of number of layer. Therefore, as the number of layers of h-BN and graphene increased, the normal force required to induced plastic deformation of the SiO<sub>2</sub> substrate increased. In the case of atomically thin MoS<sub>2</sub>, while out-of-plane bending of MoS<sub>2</sub> induced by scratch test was not predominant due to its relatively large bending stiffness, the top layer was probably wrinkled/folded at scratch tracks due to the scratching tip overcoming the binding energy between the top layer and its below layers or substrate. As it was observed that the thicker the atomically thin MoS<sub>2</sub> was, the more delayed occurrence of wrinkle formation at scratch tracks would generally be, which suggests that the binding energy between the top layer and its below layers may increase with increasing number of underlying layers. This behavior is in agreement with previous study,<sup>127</sup> which proposed that the amount of energy needed to peel off the top layer significantly increased as the number of underlying layer increased due to the enhanced interlayer binding energy that the top layer received when the material became thicker. From the progressive

scratch test results of h-BN, MoS<sub>2</sub>, and graphene, as the number of layer increased, not only the adhesion strength to substrates of these atomically thin materials increased but also the surface damages induced by scratch tests were also delayed.

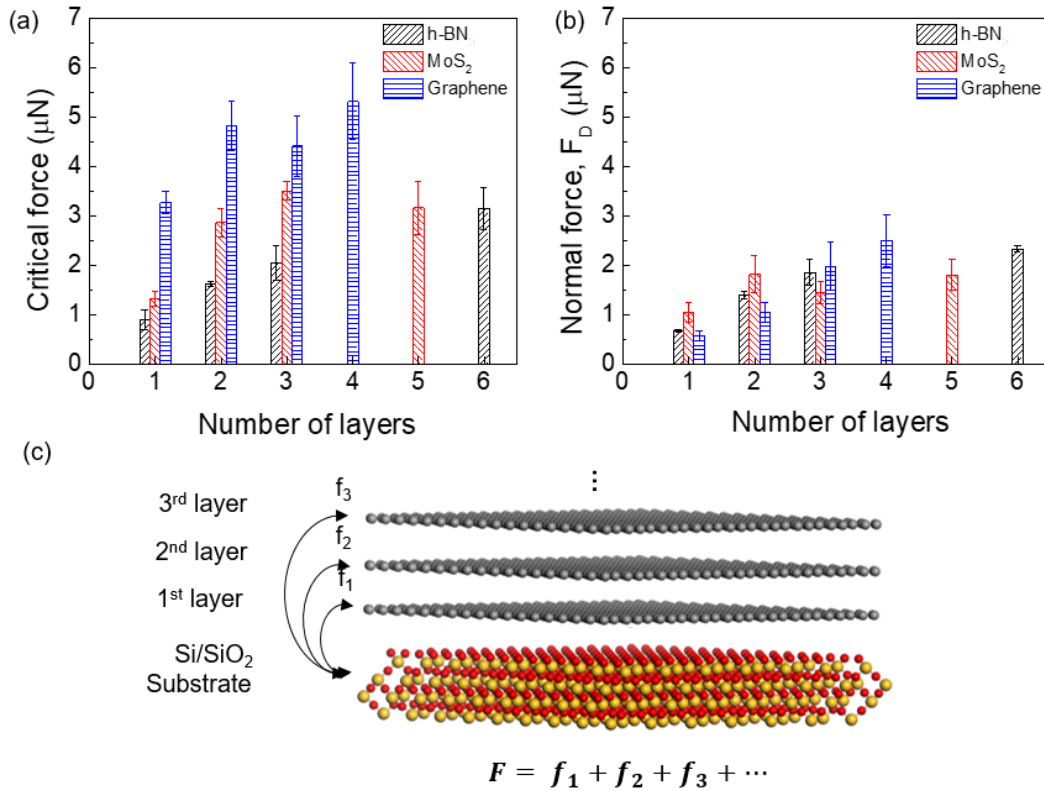


**Fig. 3.18.** Variation of the (a) critical force,  $F_c$ , and (b) normal force that induced surface damages,  $F_d$ , of h-BN, MoS<sub>2</sub>, and graphene with respect to number of layers. (c) Schematic of total van der Waals interactions between substrate and atomically thin films, which demonstrates that the total interactions between the atomically thin film and substrate gradually increased as the number of layers increased. The error bar in panel a and b represents one standard deviation.



### 3.5.2 Surface damage characteristics of multi-layer

The constant force scratch test on h-BN, MoS<sub>2</sub>, and graphene with various number of layer were also conducted. Topographic and FFM images of scratched areas on tri- and multi-layer h-BN, MoS<sub>2</sub> and graphene under various normal force from Fig. 3.19 (d) clearly show that, compared to what were observed from scratched areas of single-layer materials, surface damages including wrinkle formation and plastic deformation were effectively reduced as the number of layer increased. For instance, under 1,500 nN normal force, while single-layer h-BN was found to be torn-off after a few scratches, while no significant damages were observed at scratched area of tri-layer h-BN. Under 2,500 nN normal force, although single-layer MoS<sub>2</sub> was immediately failed, just a few wrinkles were locally formed at scratched areas of tri-layer MoS<sub>2</sub>. In the case of tri-layer graphene after scratch test under 3,000 nN normal force, a height decrease of about 0.5 nm were observed at scratched area, while a height decrease of 1 nm was previously found at scratched area of single-layer graphene under same normal force. The result indicates that the degree of plastic deformation of substrate at scratched area of tri-layer graphene was significantly reduced.

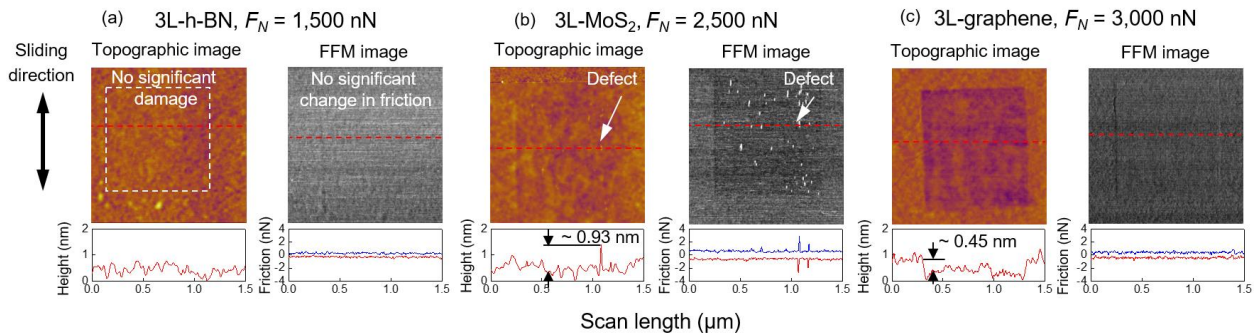


**Fig. 3.19. High resolution topographic and FFM (forward scan) images of tri-layer (a) h-BN, (b) MoS<sub>2</sub>, and (c) graphene after a constant force scratch test under various normal force. The atomically thin materials were scratched under a constant normal force at the area of 1 μm × 1 μm as indicated by white dashed square. The cross-sectional height profile and friction loop are also included in the images**

### 3.5.3 Frictional behaviors during scratch tests.

Friction force variation during constant force scratch test with respect to number of layers of h-BN, MoS<sub>2</sub>, and graphene, as plotted in Fig. 3.20 (a), clearly show thickness-dependent friction of these atomically thin materials. Under the same normal force, as the number of layer decreased, friction force was found to be increased, and the largest friction was measured at single-layer materials. The dependence of friction force on number of layers has been considered as one of a few general frictional behaviors of these layered materials,<sup>83</sup> which is because of the out-of-plane deformation, or “puckering effect”, of the top layers in front of AFM tip during contact sliding. Interestingly, this thickness-dependent friction of atomically thin materials was reserved during scratch test under extremely large normal force in this work with the complicated factors including deformation of substrate and surface damages might all significantly affect to the friction force measurements, while these factors was likely eliminated by using very small normal force (~1 nN with tip radius of about 10 nm) from the study of Lee *et al.*<sup>83</sup> Furthermore, based on the variation of friction force with respect to normal force, two distinct frictional behaviors, including linear and non-linear dependence of friction force on normal force, were clearly observed. In particular, single-, bi-, and tri-layer graphene, as well as bi- and tri-layer h-BN exhibited the non-linear dependence of friction force on normal force. While friction force of atomically thin MoS<sub>2</sub> (regardless number of layers), single- and multi-layer h-BN, and multi-layer graphene clearly demonstrates a linear relationship with normal force. Based on the topographic images of these atomically thin materials after scratch tests as shown in Fig. 3.20 (b), we found that the linear and non-linear dependence of friction force on normal force is closely related to the deformation of the underlying SiO<sub>2</sub> substrate due to scratch test. For instance, the underlying SiO<sub>2</sub> substrates at scratched areas of atomically thin MoS<sub>2</sub> (regardless number of layers), as well as multi-layer h-

BN and graphene were not plastically deformed after scratch tests. While plastic deformation of SiO<sub>2</sub> substrate can be clearly observed at scratched areas of single-, bi-, and tri-layer graphene, as well as bi- and tri-layer h-BN based on the height decrease at those areas.

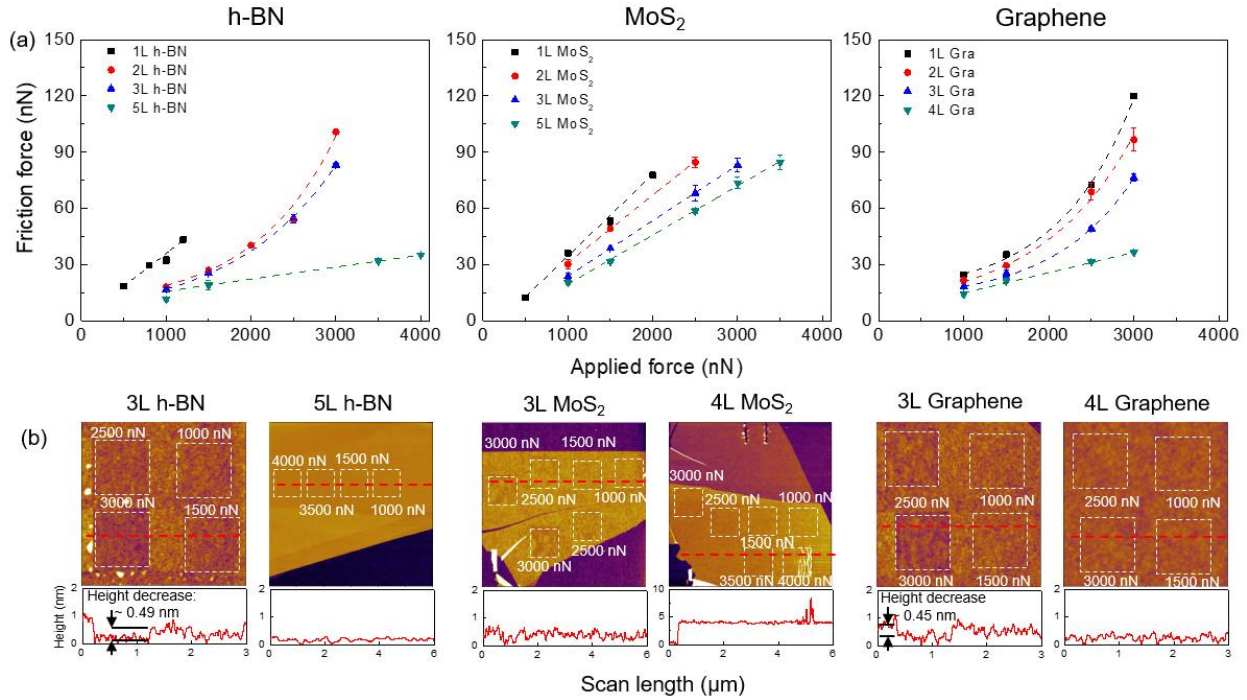


**Fig. 3.20.** Variation of friction force of single- and a few-layer h-BN, MoS<sub>2</sub>, and graphene during constant force scratch tests. The friction data was fitted by linear and exponential relationships with normal force. Error bar in panel a corresponds to one standard deviation. (b) AFM topographic images of tri- and multi-layer h-BN, MoS<sub>2</sub>, and graphene after constant force scratch test. In panel b, the topographic images were obtained from the intermittent contact mode of AFM. Cross-sectional profiles are included and the red dashed lines indicate the location where the cross-sectional profile are taken. These atomically thin materials were scratched under a constant normal force at the area of 1  $\mu\text{m} \times 1 \mu\text{m}$  as indicated by white dashed square in panel b.

The close correlation between the plastically deformed SiO<sub>2</sub> substrate at scratched areas of atomically thin materials and their non-linear dependence of friction force on normal force may suggest that the deformation of the underlying substrate could introduce additional friction force to AFM tip during scratch tests. This additional friction force is likely attributed to shear force required to plow the underlying SiO<sub>2</sub> substrate at scratched areas. As it has been reported in the recent study of friction characteristics between silica probe and micelles layers,<sup>128</sup> which also observed an additional friction force due to the deformation of the micelles layers, resulting in the nonlinear dependence of friction on normal force. As the number of layers increased, the deformation of SiO<sub>2</sub> substrate at scratched areas was effectively reduced, hence friction force of multi-layer materials during scratch tests remained linearly proportional to normal force as clearly shown in Fig. 3.20 (a).

Based on progressive and constant force scratch tests on atomically thin h-BN, MoS<sub>2</sub>, and graphene with various number of layers, the results clearly show that not only the adhesion strength to substrate of atomically thin materials increased with increasing number of layers, but also the occurrence and the degree of surface damages, such as wrinkle formation and plastic deformation, induced by scratch tests were found to be more delayed as the materials was thicker. Furthermore, as the number of layers increased, friction force during scratch test was found to be decreased. The improvement of adhesion strength to substrate, surface damage resistance as well as friction force of atomically thin h-BN, MoS<sub>2</sub>, and graphene as the number of layer increased indicates that the tribological performance of these atomically thin materials could be effectively enhanced by simply increasing the thickness of materials. However, considering that the material properties of atomically thin h-BN, MoS<sub>2</sub>, and graphene could drastically change with their thicknesses, for instance the desirable electrical properties were often found from the thinnest ones. While in the

miniaturized nanoscale systems, apart from the primary surface damage resistance application, these atomically thin-based coating layers could be employed for other purposes regarding to their material properties. Therefore, optimizing the choice of the thickness of these atomically thin materials as protective and solid lubricant coating layers while maintaining the beneficial combination of material properties from that choice is essential.

### **3.6 Summary**

In summary, this work presents a systematical investigation of surface damage resistance of atomically thin h-BN, MoS<sub>2</sub>, and graphene using AFM-based scratch tests including progressive force and constant force scratch tests. Adhesion strength to substrate of single- and a few-layer h-BN, MoS<sub>2</sub>, and graphene were evaluated based on their critical forces obtained from the progressive force scratch test. The results suggest that these atomically thin films were strongly adhered to their substrates, which in-turn significantly improve the load carrying capacity of the underlying substrate. Furthermore, single-layer graphene was found to have stronger adhesion strength to substrate than that of single-layer h-BN and MoS<sub>2</sub>.

Surface damage characteristics of single-layer h-BN, MoS<sub>2</sub>, and graphene were further investigated using the constant force scratch tests. The results suggest the evolution of surface damage of these atomically thin materials under three different ranges of normal force with respect to their load carrying capacities. At relatively low normal force, no significant change in topography and friction force was observed at scratched areas, which indicates scratch test induced pure elastic deformation to the intact atomically thin materials. As normal force increased, defect formations along with plastic deformations of the underlying substrate at scratched areas were observed. At this stage, although the atomically thin materials were not failed yet, their topography, friction force, as well as crystalline quality and mechanical strengths were permanently affected,

which may in turn significantly degrade their tribological performance. As the normal force finally reached to the critical force for failure, the atomically thin materials were torn-off, and the substrates were exposed. The residual in-plane compressive strain observed from the scratched areas of single-layer h-BN, MoS<sub>2</sub> and graphene could further shed the light on the determination of the failure mechanism of these atomically thin materials. The compressive strain-induced buckling formation in front of AFM tip was likely to be the primary source of mechanical instability of these atomically thin films during scratch tests. As the compressive strain increased, the atom bonds in materials were further compressed, and eventually rupture.

In addition, based on the results obtained from progressive force scratch test, the adhesion strength to the substrate as well as surface damage resistance of atomically thin h-BN, MoS<sub>2</sub>, and graphene were found to be generally enhanced as the number of layers increased. Furthermore, from the constant scratch test results, the degree of surface damages as well as friction force of atomically thin h-BN, MoS<sub>2</sub>, and graphene were generally decreased with increasing number of layers. Therefore, the tribological performances of these atomically thin materials could be effectively improved by simply increasing number of layers.

## Chapter 4

### Friction characteristic of 2D materials

Layered materials such as bulk h-BN, MoS<sub>2</sub>, and graphite are conventionally used as solid lubricants for number of critical engineering applications based on their low friction characteristics. The characteristically weak interlayer bonding in the structure was found to be responsible for the remarkably low shear strength at the contacting interface of these layered materials.<sup>4,5</sup> In addition, 2D materials such as single-layer h-BN, MoS<sub>2</sub>, and graphene have been proposed to have a great potential for use as nanoscale protective and solid lubricant coating layers. These solid lubricant coating layers are used to primarily reduce friction force generated at the contacting interface between mechanical moving parts in the system, which is one of the major sources of energy dissipation and possibly severe damage to the nano-scale device. Therefore, comprehensive understanding of nanoscale frictional behaviors of these single-layers materials is essential.

In this chapter, friction characteristics of single-layer h-BN, MoS<sub>2</sub>, and graphene were systematically investigated using friction force microscopy (FFM) measurements under various test conditions such as normal force and sliding speed, and environmental conditions such as relative humidity and thermal annealing. From the FFM measurement results, the dependence of topography, normal force, sliding speed, relative humidity, and thermal annealing on frictional behaviors of these single-layer materials was clearly observed. These observations are useful not only for comprehensive fundamental understating of their nanoscale friction characteristics, but also for design of the reliable nanoscale protective and solid lubricant coating layers based on these single-layer materials.

## 4.1 Experimental section

Atomically thin h-BN, MoS<sub>2</sub>, and graphene were deposited onto Si substrate capped by 300 nm of thermally grown SiO<sub>2</sub> using mechanical exfoliated method. Preparation and thickness characterization of these atomically thin materials are similar to the procedure presented in section 3.1. Particularly, atomically thin materials were located using optical microscopy (VK-X200, Keyence) and their topographic images were then obtained from the intermittent contact mode of AFM (MFP-3D, Asylum Research) using Si tips (AC240, Olympus). Based on the cross-sectional height profiles from these topographic images, thickness of single-layer h-BN, MoS<sub>2</sub>, and graphene were carefully determined. Furthermore, to confirm the thickness of these single-layer materials, Raman spectroscopy (Alpha300R, Witec) measurements were also conducted with a 532 nm excitation laser wavelength and a 100× objective (NA ~ 0.9). In Raman spectroscopy measurements, to avoid surface damage induced by thermal effect,<sup>89,103</sup> laser power was kept well below 0.5 mW.

After characterization of thickness of these single-layer materials, their friction characteristics were systematically investigated using FFM measurements under various test conditions such as normal force and sliding speed, and environmental conditions such as relative humidity and thermal annealing. In FFM measurements, ultra-nanocrystalline diamond tip (NaDiaProbes, Advanced Diamond Technologies) with tip radius of about 40 nm was scanned across the surfaces of these single-layer materials using contact mode of AFM. For the quantitative force measurements using AFM, normal<sup>104</sup> and lateral<sup>81</sup> force calibrations were carefully performed prior to FFM measurements. The calibration results showed that the normal spring constant and lateral force sensitivity of the diamond tip used for FFM measurements were about 0.15 N/m and 1.04 mV/nN, respectively.



The effects of test conditions including normal force and sliding speed on friction of these single-layer materials were parametrically investigated in the ambient conditions (25 °C, 30 % RH). Particularly, the normal force was varied in the range from 1 nN to 50 nN with sliding speed was set to 375 nm/s. The sliding speed was then varied in the range of 10 nm/s – 3,000 nm/s with normal force was set to 1 nN, 5 nN, and 7 nN. It should be noted that the maximum normal force (50 nN) selected in this work was relatively small to reduce the possibility of inducing surface damage during FFM measurements, and the minimum normal force used was as small as possible, which depends on the adhesion force between tip and these single-layer materials. In addition, considering the scan length of about 300 nm in FFM measurements, the maximum sliding speed (3,000 nm/s) was selected to obtain reliable friction force data.

The effect of environmental conditions such as relative humidity, thermal annealing, and temperature on frictional behaviors of single-layer h-BN, MoS<sub>2</sub>, and graphene were further investigated. Particularly, the humidity-dependent friction of these single-layer materials was characterized in the humidity cell (Humidity Sensing Cell, Asylum Research) at different relative humidity. To control the relative humidity, a gas mixture consists of dry nitrogen gas and nitrogen gas bubbled through the flask of water was continuously flew into the humidity cell. By adjusting the gas ratio of a mixture using two rotameters, the relative humidity in the cell could be well controlled in the range between 5 % and 75 %. The relative humidity was initially lowered to 5 % and then slowly increased to 75 % with the interval time of 2 hours. Effect of temperature, including thermal annealing process, on friction characteristics of these single-layer materials was then investigated using the temperature-controlled stage (Polyheater, Asylum Research). In the thermal annealing process, temperature was gradually increased from room temperature (~ 25 °C) to 100 °C with the temperature rate of about 25 °C / 2h, the temperature was then keep at 100 °C

for 2h before the cooling-down process naturally initiated. For comparison, FFM measurements of these single-layer materials were conducted before and after the thermal annealing process. In addition, frictional behaviors of these single-layer materials under various temperatures including 50 °C, 75 °C, and 100 °C, were also observed. It should be noted that the effect of test conditions and environmental conditions on friction force of single-layer h-BN, MoS<sub>2</sub>, and graphene were investigated on different sets of materials to ensure the accurate observation of each effect. Furthermore, considering the adhesion forces between tip and these single-layer materials could significantly affect their frictional behaviors, the variations of adhesion force before and after FFM measurements were carefully monitored.

## 4.2 Thickness characterization of single-layer materials

Topographic images of atomically thin h-BN, MoS<sub>2</sub> and graphene on SiO<sub>2</sub> substrate obtained from the intermittent-contact mode, as shown in Fig. 4.1 (a), clearly demonstrate the relatively clean surface of these materials. Furthermore, based on the cross-sectional height profiles, thickness of single-layer h-BN, MoS<sub>2</sub>, and graphene was determined to be about 0.47 nm, 0.71 nm, and 0.53 nm, respectively. These estimated thicknesses are in good agreement with those of single-layer h-BN, MoS<sub>2</sub>, and graphene reported from previous studies.<sup>89,129,130</sup>

These single-layer materials were further examined by Raman spectroscopy with a 532 nm excitation source at room temperature. Based on the Raman spectra of single-layer h-BN, MoS<sub>2</sub> and graphene as shown in Fig. 4.1 (b) clearly revealed the dependence of their Raman characteristic peaks on thickness, which are also consistent with other studies.<sup>96-98</sup> Particularly, Raman spectra of single-layer h-BN show relatively weak  $E_{2g}$  characteristic peak ( $\sim 1367\text{ cm}^{-1}$ ), arising from the in-plane vibration of B-N atoms.<sup>96</sup> In the case of single-layer MoS<sub>2</sub>, their Raman spectra shows two Raman characteristic peaks,  $E_{2g}^1$  peak ( $\sim 385\text{ cm}^{-1}$ ) and  $A_{1g}$  peak ( $\sim 403\text{ cm}^{-1}$ ),

which are associated with the in-plane vibration of Mo-S atoms and the out-of-plane vibration of the S atoms, respectively.<sup>97</sup> As for the single-layer graphene, two Raman characteristic peaks including G peak ( $\sim 1580\text{ cm}^{-1}$ ) and sharp and symmetric 2D peak ( $\sim 2670\text{ cm}^{-1}$ ) can be clearly observed from the Raman spectra.<sup>98</sup>

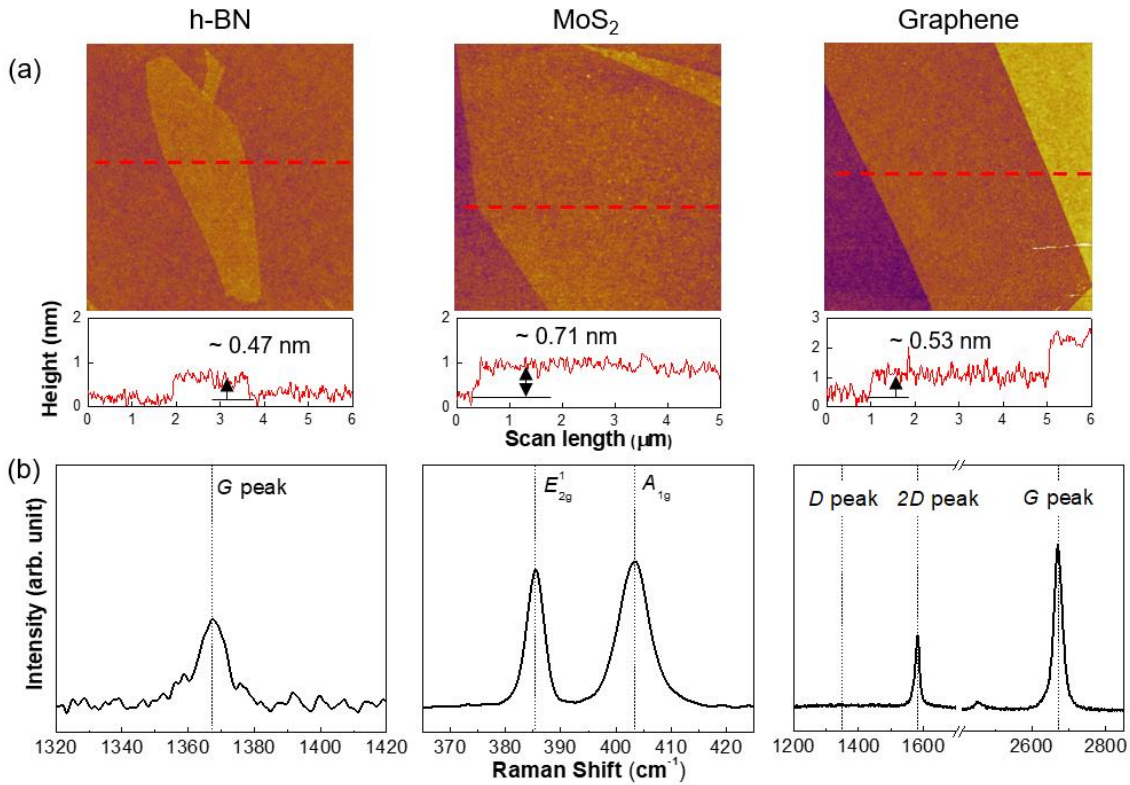
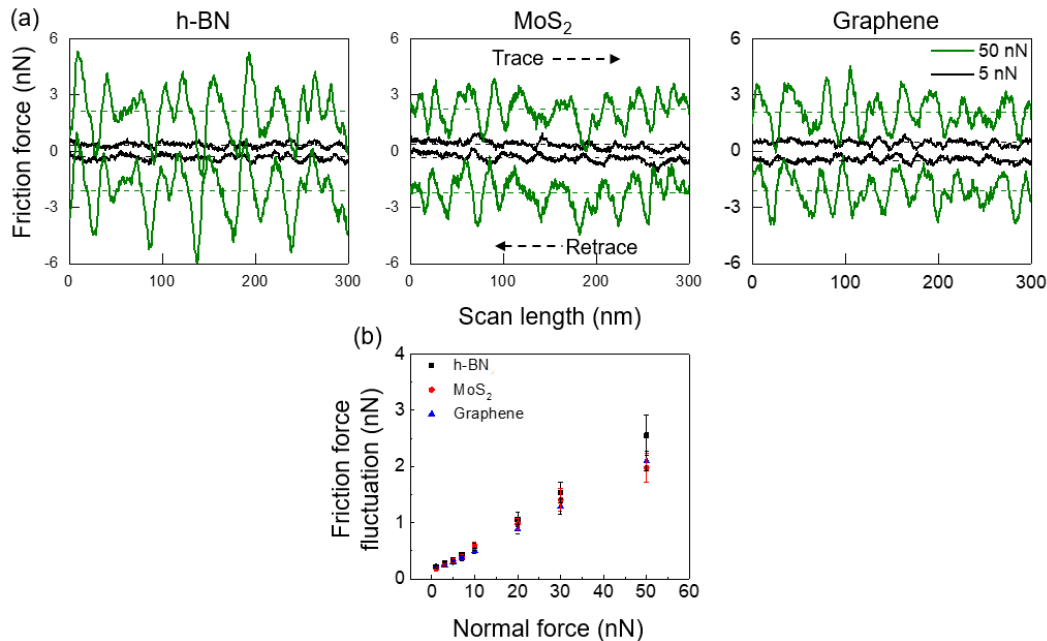


**Fig. 4.1. (a) AFM topographic images and (b) Raman spectra of single-layer h-BN, MoS<sub>2</sub> and graphene. Topographic images were obtained from intermittent contact mode of AFM, the cross-sectional profiles are included in panels a. Red-dashed lines indicate the locations where the cross-sectional profiles are taken. In panels b, frequency of the characteristic Raman peaks of single-layer h-BN, MoS<sub>2</sub>, and graphene are denoted as dashed lines.**

### 4.3 Effect of test conditions: normal force and sliding speed

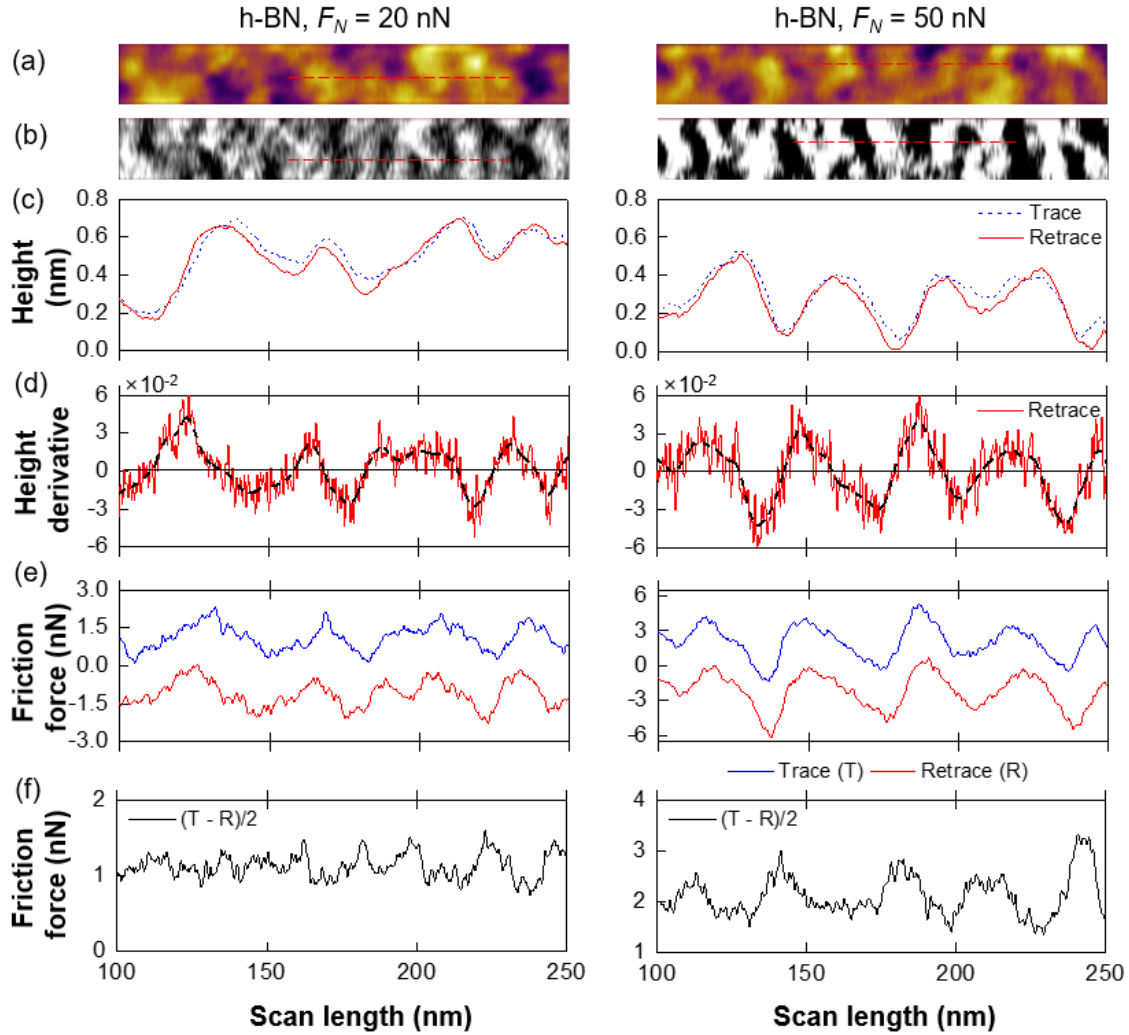
#### 4.3.1 Effect of topography

Fig. 4.2 (a) shows the representative example of friction loops obtained from single-layer h-BN, MoS<sub>2</sub>, and graphene under normal force of 5 nN and 50 nN. A typical friction loop consists of trace and retrace friction profiles, which are obtained by sliding the AFM tip over sample in the forward and backward directions, respectively. From friction loop, friction value that fluctuated from its average value (dashed line) was considered as the friction fluctuation. According to Fig. 4.2 (a), a significant increase in friction fluctuation of single-layer h-BN, MoS<sub>2</sub>, and graphene was clearly observed as the normal force increased from 5 nN to 50 nN. The variation of friction fluctuation with respect to normal force as shown in Fig. 4.2 (b) also demonstrated that as the normal force increased friction fluctuation of these single-layer materials significantly increased.



**Fig. 4.2. (a) Friction loops consisting of friction forces measured in both trace (forward scanning) and retrace (backward scanning) directions of single-layer h-BN, MoS<sub>2</sub>, and graphene, under 5 nN and 50 nN normal force. (b) Variation of friction force fluctuation in friction loop with respect to normal force.**

In addition, topographic and FFM images of single-layer h-BN, MoS<sub>2</sub>, and graphene obtained simultaneously under various normal force were presented in Figs. 4.3 (a, b), 4.4 (a, b), and 4.5 (a, b), respectively, along with the cross-sectional height profiles and friction loops. FFM images clearly show the local friction force variation of these single-layer materials along with the strong correlation between topography and friction force. It should be noted that these cross-sectional height profiles and friction loops were obtained from topographic and FFM images, respectively, at the same location to accurately evaluate the effect of surface slope on the friction force measurements of these single-layer materials. In the cross-sectional height profiles, the shapes of height trace and retrace profiles were found to be consistent with each other, which indicates the artifacts produced during contact scanning were likely negligible. The surface slope variation was further estimated by taking the derivative of the above cross-sectional height profiles single-layer h-BN, MoS<sub>2</sub>, and graphene as shown in Figs. 4.3 (d), 4.4 (d), and 4.5 (d) respectively, along with the smoothed profiles depicted as black-dashed lines. By comparing the surface slope variation and friction force variation under same normal force, it can be clearly seen that the friction force increased and decreased closely with the increase and decrease in surface slope of the topography, respectively. Particularly, when comparing the measured friction force retrace with the surface slopes obtained under same normal force, friction force was high at the edge with positive slope and low at the edge with negative slope. As normal force increased, the difference between the local highest and lowest friction force significantly increased, which indicates that the fluctuation observed at the friction loop of these single-layer materials may be due to the local variation in their friction force.



**Fig. 4.3.** (a) Topographic and (b) FFM images of single-layer h-BN obtained simultaneously from the contact mode of AFM under normal force of 20 nN and 50 nN. (c) Cross-sectional height profiles, (d) derivative cross-sectional height profile, (e) friction loops and (f) half subtracted friction are also included. The red dashed lines indicate the locations where the cross-sectional height profiles, height derivatives and friction loops were taken.

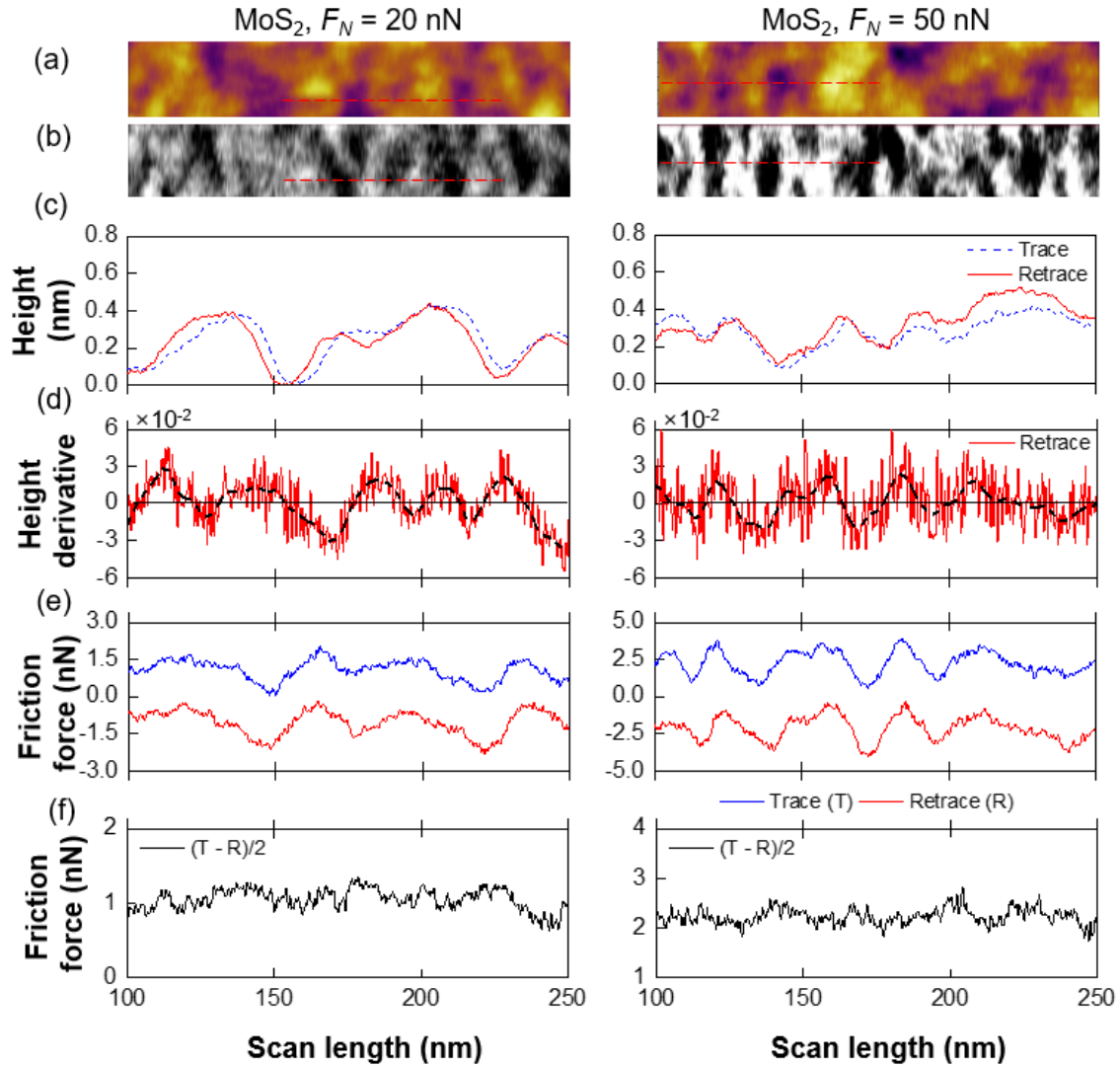


**Fig. 4.4.** (a) Topographic and (b) FFM images of single-layer MoS<sub>2</sub> obtained simultaneously from the contact mode of AFM under normal force of 20 nN and 50 nN. (c) Cross-sectional height profiles, (d) derivative cross-sectional height profile, (e) friction loops and (f) half subtracted friction are also included. The red dashed lines indicate the locations where the cross-sectional height profiles, height derivatives and friction loops were taken.

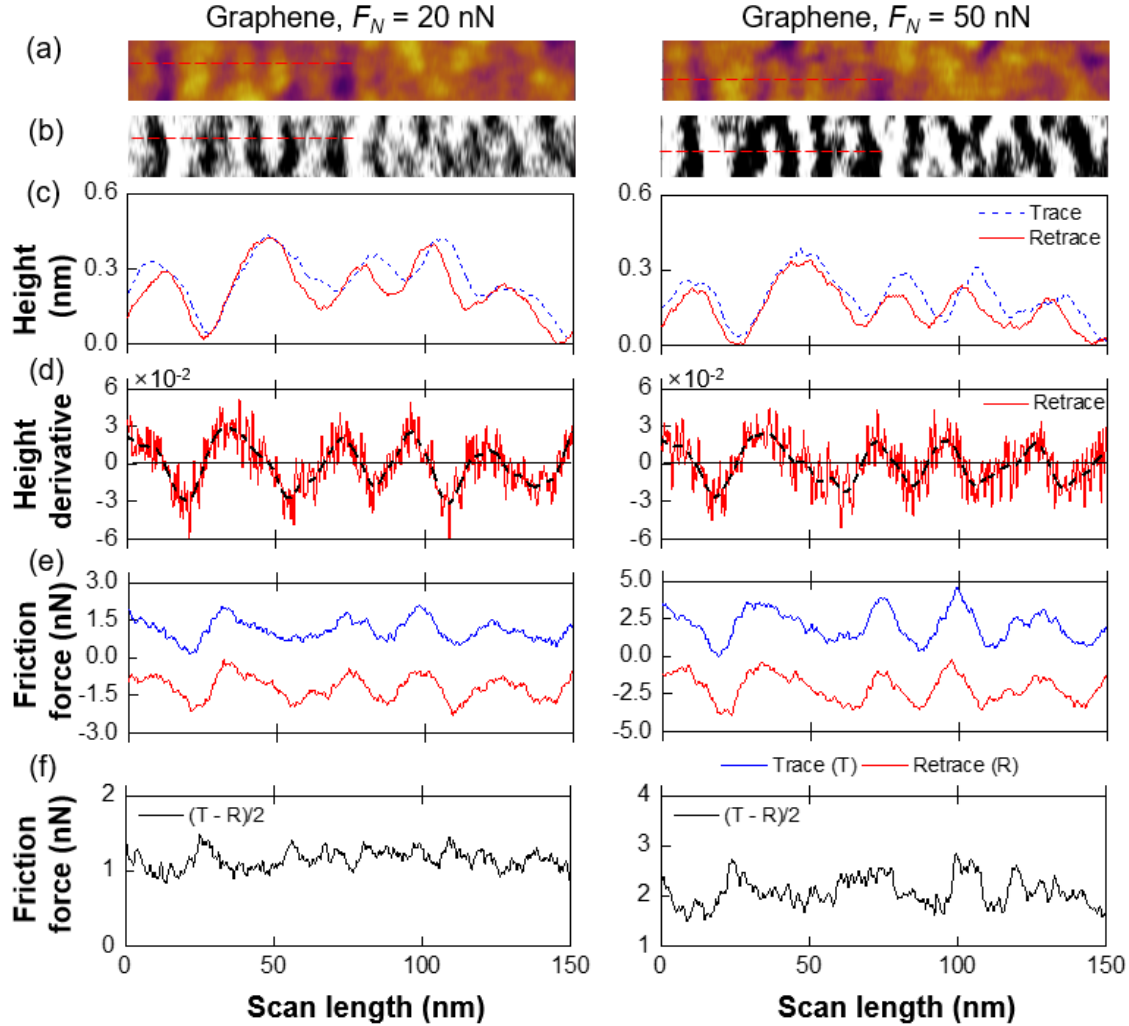


**Fig. 4.5.** (a) Topographic and (b) FFM images of single-layer graphene obtained simultaneously from the contact mode of AFM under normal force of 20 nN, and 50 nN. (c) Cross-sectional height profiles, (d) derivative cross-sectional height, (e) friction loops and (f) half subtracted friction are also included. The red dashed lines indicate the locations where the cross-sectional height profiles, height derivatives and friction loops were taken.

Considering these dominant frictional mechanisms at micro- and nano-scale, including adhesive, ratchet, and plowing. The adhesive friction mechanism could not explain these observed local variations in friction force of these single-layer materials. The ratchet mechanism described the influence of local slope on friction force measurement, that is when the tip encounter a given slope of the topography and a friction force may be required for the tip to climb against it, which



resulting in friction locally increased at that point. In addition, considering the remarkable surface damage resistance of single-layer h-BN, MoS<sub>2</sub>, and graphene, their surface damages may be not significant because of the relatively small normal force (up to 50 nN) used in FFM measurements, therefore the contribution of plowing friction on the local variation in friction was likely negligible. Hence, the local variation in friction force of these single-layer materials was due to likely attributed to the ratchet mechanism, when the tip ascending the leading edge, the surface slope was positive and friction increased; and when the tip descending the trailing edge, the surface slope was negative and friction decreased as depicted in Fig. 4.6 (a). Particularly, when an AFM tip sliding over an asperity making an angle  $\delta$  with the horizontal plane under constant normal force  $F_N$ , the slope of asperity causes a friction force varied with respect to normal force and slope of topography as  $F_F \sim \tan \delta \cdot F_N$ . Therefore, the AFM tip may experience an increase and decrease in friction when climbing up and down, respectively, an asperity of given slope, and this transition in friction corresponding to transition in slope is proportional to normal force, which may explain the increase in friction fluctuation with increasing normal force as observed from 4.2 (a) and (b). In addition to the slope effect, it was proposed that due to the ‘collision’ effect, the magnitude of the increase in friction measured when the tip climbed up an asperity was found to be larger than the magnitude of the decrease in friction measured when the tip climbed down a similar asperity.<sup>131</sup> As a results, the effect of topography on friction measured by FFM could not be eliminated by the subtraction of trace and retrace friction profiles, which is consistent with the friction force data (half of subtraction of trace and retrace) presented in Figs. 4.3, 4.4, and 4.5 (f). Although, in general, these effects of topography on friction force measured by FFM have been well established, such frictional behaviors have not been observed from single-layer h-BN, MoS<sub>2</sub>, and graphene. Therefore, this observation of topography-induced contributions to friction force of these single

materials could be useful when attempting to predict and interpret their frictional behaviors in the systems with various topographical characteristics. For example, step edges at the surface of these atomically thin materials could induce a considerable increase in friction force and even wear when the tip traversed up these steps, as previously found by other studies.<sup>71,132</sup> Although number of mechanisms have been proposed to explain these observations, the significant change in slope and the mechanical impact of AFM tip with these steps could also strongly influence these behaviors.

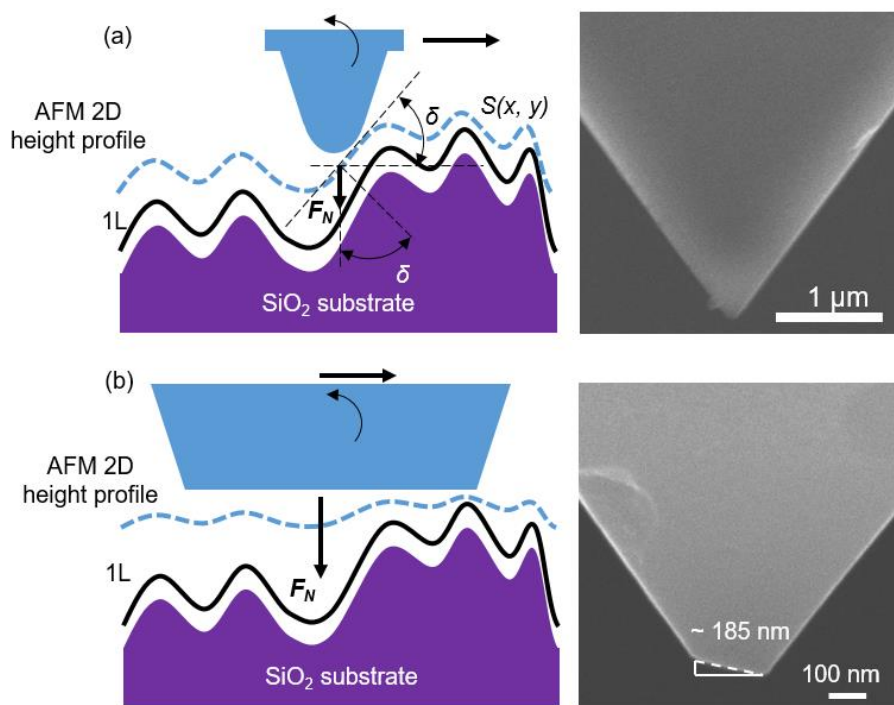


**Fig. 4.6. (a) Schematic diagram of the scanning (a) sharp tip and (b) flat-ended tip on surface of single-layer materials with these relevant force vectors. Due to the local slope of topography, normal force ( $F_N$ ) causes a component of the lateral force. In panel a and b, SEM images of the nano-crystalline diamond tips were also included.**

In the case of FFM measurements of these single-layer materials using the flat-ended diamond tip as shown in Fig. 4.6 (b), the effect of surface slope on friction force was found to be significantly different. The representative example of friction loops obtained from single-layer h-BN, MoS<sub>2</sub>, and graphene under normal force of -100 nN and 50 nN using flat-ended tip, and the

variation of friction fluctuation in friction loop with respect to normal force of these single-layer materials were presented in Fig. 4.7 (a) and (b), respectively. The results clearly demonstrated the increase in friction fluctuation as normal force increased, which indicated that the surface slope still affected the friction force measurements with the flat-ended tip. However, the degree of increase in friction fluctuation with respect to normal force using flat-ended tip was found to be relatively smaller than that using sharp tip.

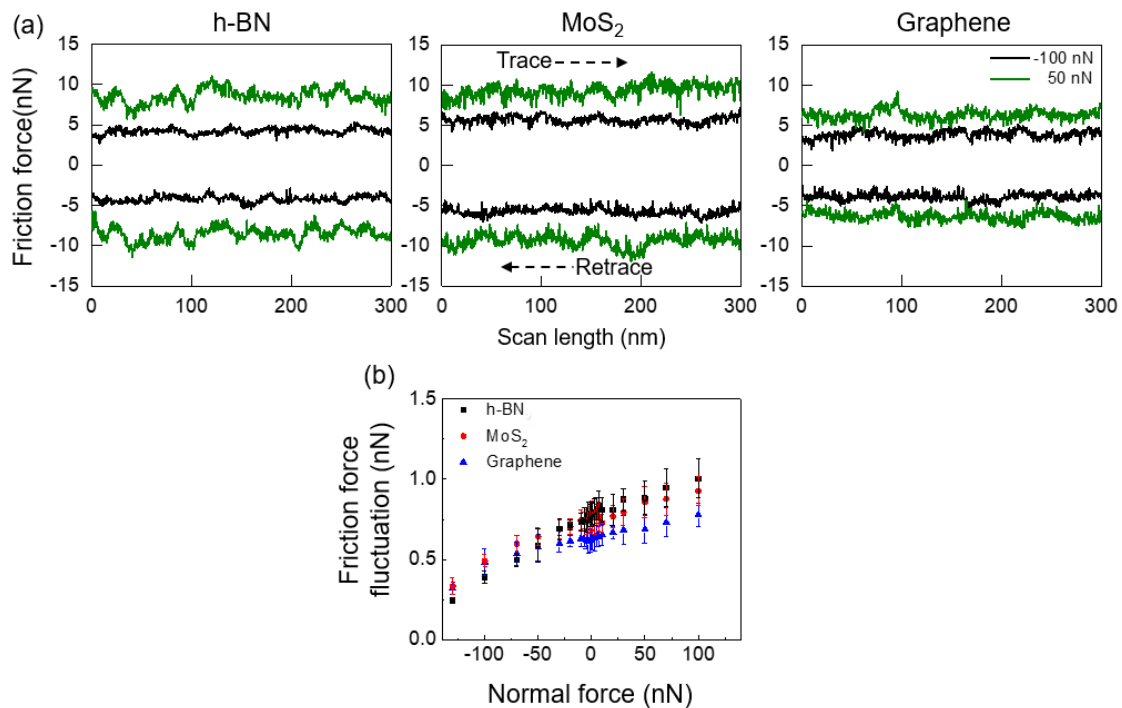


**Fig. 4.7. (a) Friction loops consisting of friction forces measured in both trace (forward scanning) and retrace (backward scanning) directions of single-layer h-BN, MoS<sub>2</sub>, and graphene, under -100 nN and 50 nN normal force. Variation of friction fluctuation in friction loop with respect to normal force. The error bar corresponds to one standard deviation.**

In addition, by using the flat-ended tip, topographic and FFM images of single-layer h-BN, MoS<sub>2</sub>, and graphene obtained simultaneously under various normal force were presented in Figs. 4.8 (a, b), 4.9 (a, b), and 4.10 (a, b), respectively, along with the cross-sectional height profiles and friction loops. Based on the cross-sectional height profile, the curvature of the surface or the

surface roughness of these single-layer materials recorded by the flat-ended tip was found to be smaller than that obtained by sharp tip. Comparing with the actual surface roughness of these single-layer materials, the significantly large contact area of flat-ended tip made it simultaneously slide over multiple asperities rather than sliding up and down an individual asperity like the case of sharp tip. Therefore, the surface roughness obtained by flat-ended tip was reasonably smaller than that obtained by sharp tip. Since the cross-sectional height profile was relatively smooth, the surface slope variation was also not significant as shown in the derivative of the corresponding height profiles, from Figs. 4.8 (d), 4.9 (d), and 4.10 (d). Although the surface slope was not significantly observed, the friction force fluctuation of these single-layer materials was found to be slightly increased with increasing normal force, which indicates that surface slope still affected the friction force measurements, although its influence on friction force was relatively weak. The observed effect surface slope on friction could be due to the effective contact areas in front of the tip, however this surface slope effect was effectively reduced most likely due to its relatively large contact area behind, which hindered the torsion of the cantilever beam when tip ascended or descended the local surface slope. Based on the friction force fluctuation with respect to local slope variation, the effects of topography on nanoscale friction force of these single-layer materials were clearly observed, which were also in agreement with the ratchet mechanism of friction.

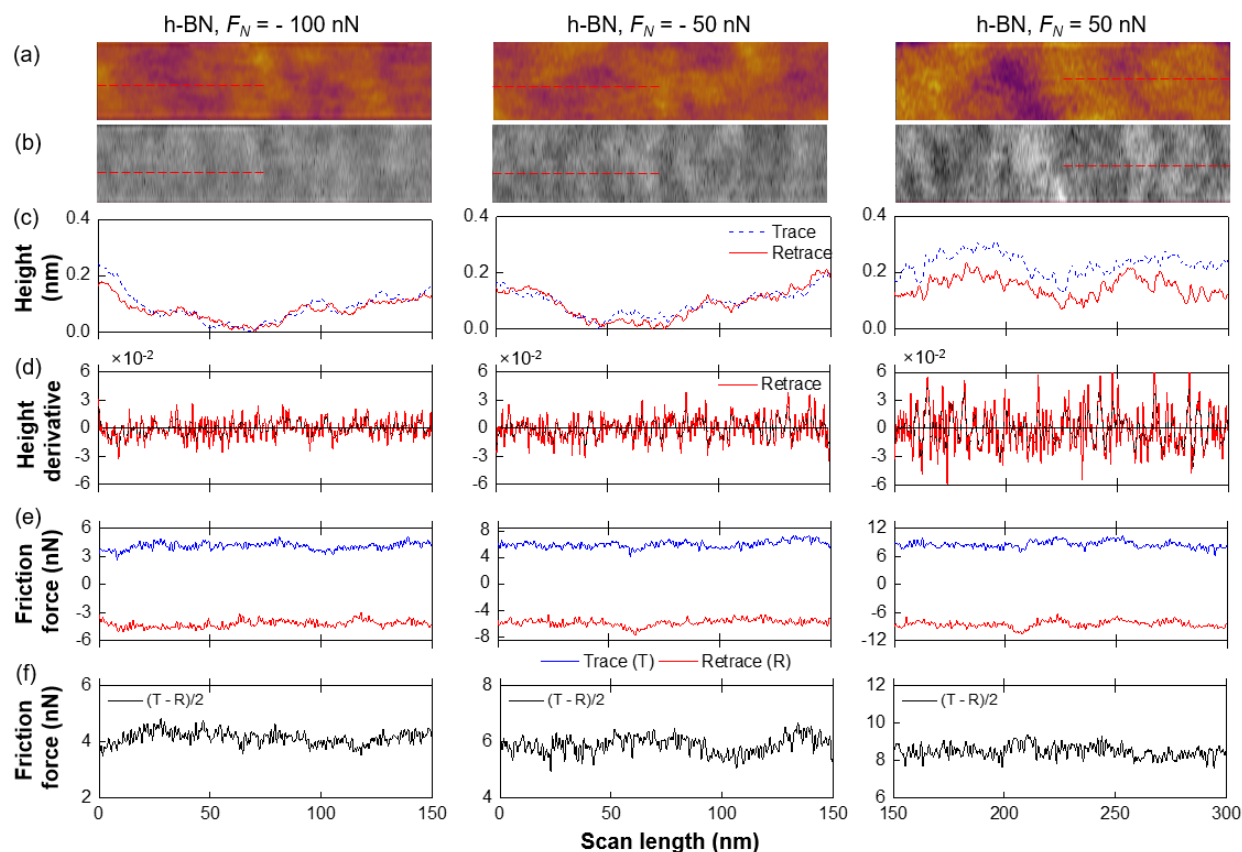


**Fig. 4.8.** (a) Topographic and (b) FFM images of single-layer h-BN obtained simultaneously from the contact mode of AFM under normal force of - 100 nN, - 50 nN, and 50 nN. (c) Cross-sectional height profiles, (d) derivative cross-sectional height profile and, (e) friction loops and (f) half subtracted friction are also included. Red dashed lines indicate the locations where cross-sectional height profiles, height derivatives and friction loops were taken.

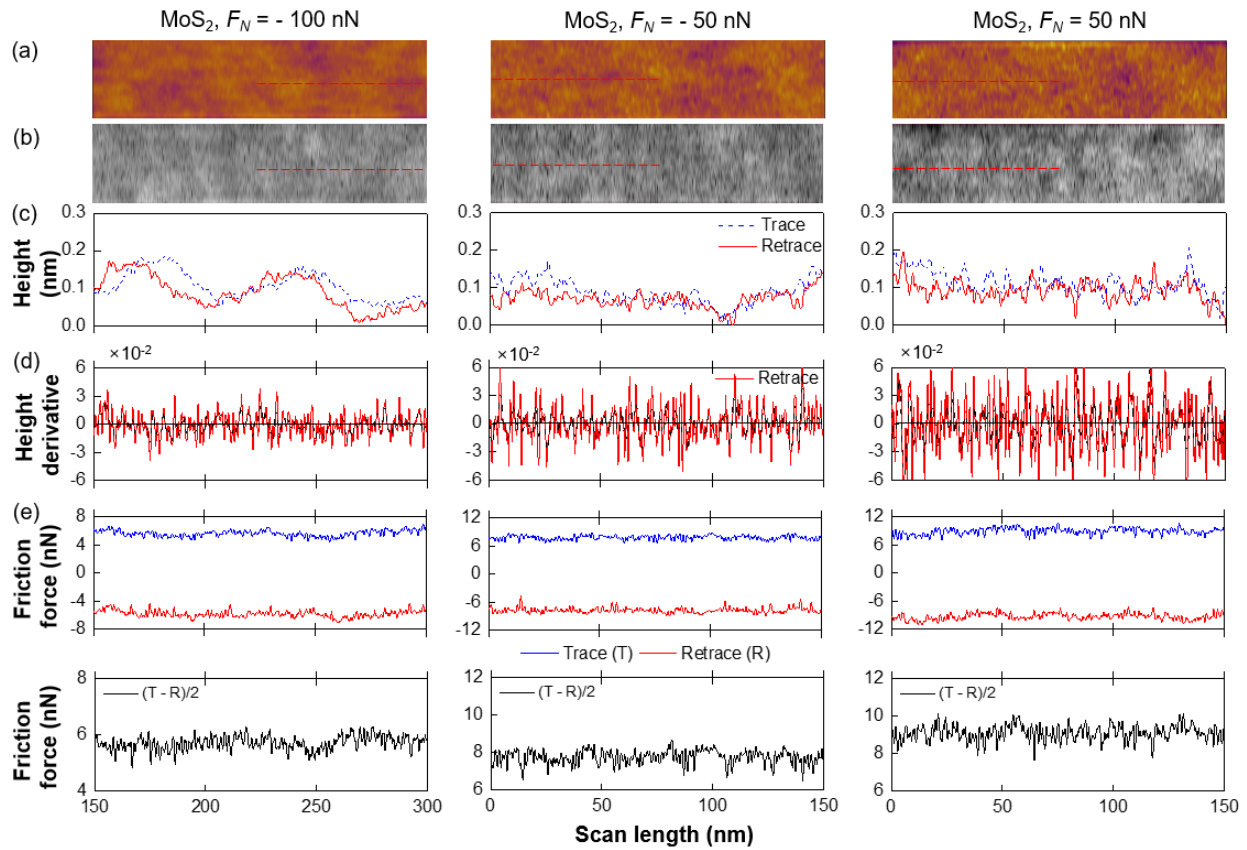


**Fig. 4.9.** (a) Topographic and (b) FFM images of single-layer MoS<sub>2</sub> obtained simultaneously from the contact mode of AFM under normal force of - 100 nN, - 50 nN, and 50 nN. (c) Cross-sectional height profiles, (d) derivative cross-sectional height profile and, (e) friction loops and (f) half subtracted friction are also included. Red dashed lines indicate the locations where cross-sectional height profiles, height derivatives and friction loops were taken.

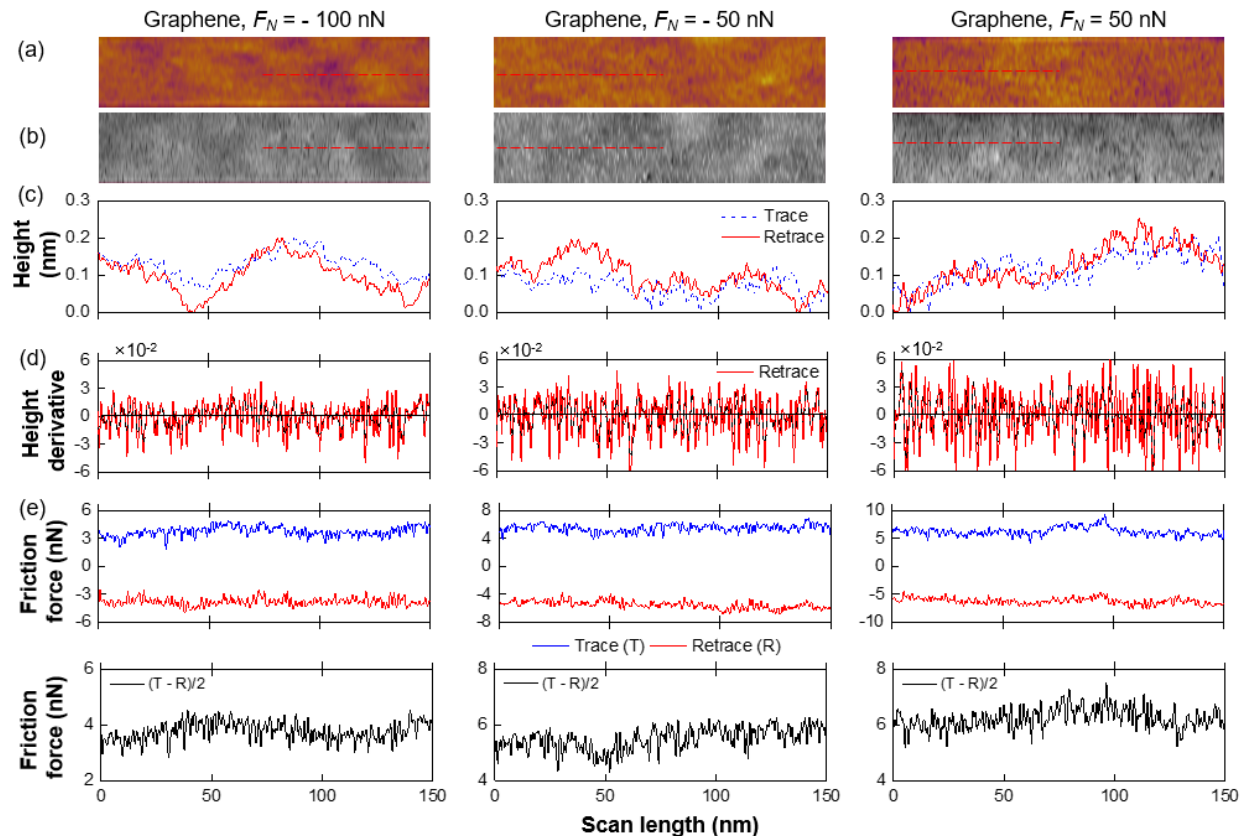


**Fig. 4.10.** (a) Topographic and (b) FFM images of single-layer graphene obtained simultaneously from the contact mode of AFM under normal force of - 100 nN, - 50 nN, and 50 nN. (c) Cross-sectional height profiles, (d) derivative cross-sectional height profile, (e) friction loops and (f) half subtracted friction are also included. Red dashed lines indicate the locations where the cross-sectional height profiles, height derivatives and friction loops were taken.

### 4.3.2 Effect of normal force

In addition to the friction force fluctuation, based on the friction loop, the variation of friction force of single-layer h-BN, MoS<sub>2</sub>, and graphene with respect to normal force was shown in Fig. 4.11 (a). From the results, friction force of these single-layer materials increased from 0.16 nN to 2.22 nN as the normal force increased from 1 nN to 50 nN, which generally demonstrated their low friction force characteristics. In addition, the normal force-dependent friction of single-layer h-BN, MoS<sub>2</sub>, and graphene was found to be slightly different from each other. Particularly, as the normal force increased from 1 nN to 50 nN, single-layer MoS<sub>2</sub> exhibited a slightly larger degree of increase in friction (from 0.16 nN to 2.22 nN) than those of single-layer h-BN (from 0.18 nN to 2.11 nN) and graphene (from 0.34 nN to 2.09 nN). This behavior could be attributed to the difference in mechanical properties of these single-layer materials. For example, friction of fluorinated graphene was recently found to be larger than that of pristine graphene, and the larger out-of-plane bending stiffness of fluorinated graphene was proposed to be the major reason for this enhancement in friction.<sup>90</sup> The out-of-plane bending stiffness of single-layer h-BN, MoS<sub>2</sub>, and graphene was previously determined to be about 0.95 eV,<sup>51</sup> 9.61 eV,<sup>53</sup> 1.40 eV,<sup>55</sup> respectively, therefore the larger bending stiffness of single-layer MoS<sub>2</sub> could be responsible for its larger degree of increase in friction. Fig. 4.11 (b) shows adhesion force between AFM tip and these single-layer materials acquired before and after FFM measurement. The average adhesion force of single-layer h-BN, MoS<sub>2</sub> and graphene was estimated to be about 4.6 nN, 4.7 nN, and 5.3 nN, respectively. From this result, a slightly larger adhesion force of single-layer graphene could be responsible for its larger friction obtained under relatively low normal force, which is agree with previous study.<sup>81</sup> In addition, the change in adhesion force between AFM tip and these single-layer materials obtained before and after FFM measurements was found to be well below 5 %, which



suggests that the tip wear during FFM measurements could be negligible. Overall, the normal force-dependent friction characteristics of single-layer h-BN, MoS<sub>2</sub>, and graphene demonstrated the influence of adhesion characteristics and mechanical properties on their frictional behaviors, in which friction obtained under low normal force was more affected by adhesion, and as the normal force further increased the effect of mechanical properties on friction became more dominant. Such understanding is important when using these single-layer materials as the coating layers for nanoscale devices operated under various contact pressure conditions, such as at low contact pressure situation (e.g. shunt switch)<sup>133</sup> large adhesion force may cause stiction problem in the system, whereas at high contact pressure situation (e.g. anti-wear)<sup>18</sup> large bending stiffness-induced large friction force may deteriorate the lifetime of the nanoscale protective coating layers and eventually cause the severe damage in the system.

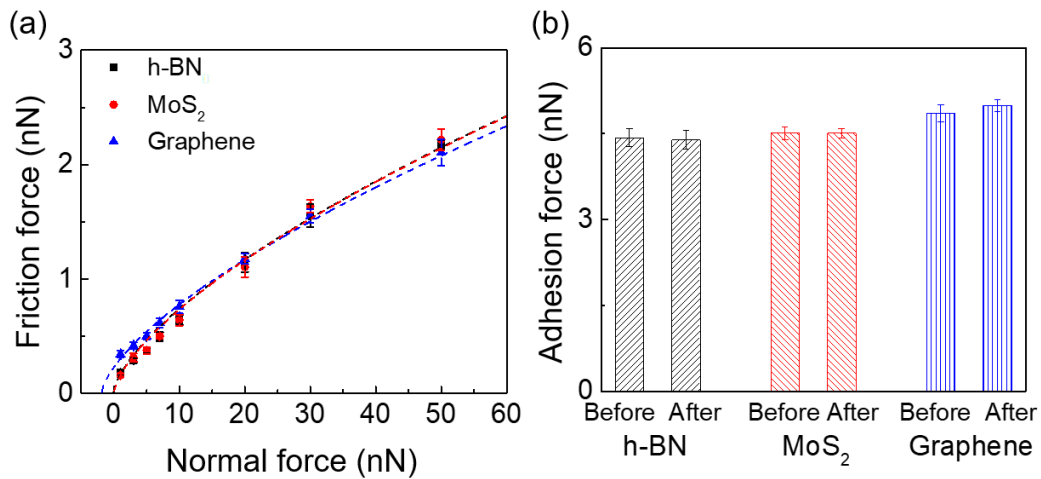


**Fig. 4.11. (a) Variation of friction force as a function of normal force of single layer h-BN, MoS<sub>2</sub> and graphene. (b) Variation of adhesion force between tip and single-layer h-BN, MoS<sub>2</sub>, and graphene obtained before and after FFM measurements. In panel a, friction force data were fitted to Hertz-plus-offset (HPO) model using Eq. 4.1. The error bar corresponds to one standard deviation.**

Furthermore, the variation of friction force of single-layer h-BN, MoS<sub>2</sub>, and graphene as a function of normal force as shown in Fig. 4.11 (a) clearly demonstrated the nonlinear dependence between friction force and normal force, as predicted by several continuum models of the elastic contact in the single asperity regime.<sup>134-136</sup> With an aim to determine the interfacial shear strength of these single-layer materials, which is the stress required to slide the diamond tip across the surface of these single-layer materials, the normal force-dependent friction was fit to the modified theory of Derjaguin-Muller-Toporov (DMT) and Maugis, also referred as the Hertz-plus-offset (HPO) model.<sup>137,138</sup>

$$F_f = \tau A = \tau \pi \left(\frac{R}{K}\right)^{\frac{2}{3}} (F_N + F_A - F_{off})^{\frac{2}{3}} \quad (4.1)$$

In Eq. 4.1,  $F_f$  is the friction force,  $\tau$  is the interfacial shear strength,  $R$  is the radius of the tip,  $K$  is the effective elastic modulus of the contact,  $F_N$  is the normal force,  $F_A$  is the adhesion force, and  $F_{off}$  is the constant offset caused by adhesion and  $|F_{off}|$  should be lower than the adhesion force. The effective elastic modulus of the contact was expressed as:

$$K = \frac{3}{4} \left( \frac{1-\nu_t^2}{E_t} + \frac{1-\nu_s^2}{E_s} \right)^{-1} \quad (4.2)$$

where  $\nu_t$  and  $E_t$  is the Poisson's ratio and elastic modulus of the AFM tip, and  $\nu_s$  and  $E_s$  is the Poisson's ratio and elastic modulus of the atomically thin materials. The Poisson's ratio and elastic modulus of the AFM nanocrystalline diamond tip used for the calculation were 0.2 and 463 GPa,<sup>139</sup> respectively, with the tip radius was estimated to be about 40 nm by using the electron scanning microscopy (SEM). The Poisson's ratio of atomically thin h-BN, MoS<sub>2</sub> and graphene used for the calculation were about 0.20,<sup>140</sup> 0.27,<sup>7</sup> and 0.17,<sup>8</sup> respectively. And the elastic modulus of atomically thin h-BN, MoS<sub>2</sub> and graphene were selected to be about 27 GPa,<sup>50</sup> 57 GPa,<sup>52</sup> and 25 GPa,<sup>141</sup> respectively. It should be noted that the out-of-plane elastic moduli of bulk h-BN, MoS<sub>2</sub>,

and bi-layer graphene was used due to the lack of knowledge of the out-of-plane elastic moduli of these single-layer materials.

Interfacial shear strengths of single-layer h-BN, MoS<sub>2</sub>, and graphene was estimated to be about  $46.4 \pm 1.4$  MPa,  $74.5 \pm 3.3$  MPa, and  $51.8 \pm 1.0$  MPa, respectively. The shear strength for diamond tip sliding against single-layer MoS<sub>2</sub> was slightly larger than the case of single-layer h-BN and graphene, which is in agreement with the observed larger degree of increase in friction with increasing normal force of single-layer MoS<sub>2</sub> than those of single-layer h-BN and graphene. In literature, shear strength between Si<sub>3</sub>N<sub>4</sub> tip and single-layer graphene were recently estimated to be about 23.6 MPa by the work of Deng *et al*,<sup>82</sup> whereas interfacial shear strengths of single-layer h-BN and MoS<sub>2</sub> have not been fully discovered yet. The interfacial shear strength of single-layer graphene estimated in this work was about two times larger than that found by Deng *et al*,<sup>82</sup> which could be due to the different tip materials used in FFM measurements. The availability of C-C bonding with sp<sup>2</sup> configuration in the structure of the nanocrystalline diamond tip may offer the commensurate contact between tip and graphene,<sup>139</sup> whereas Si-N bonding in Si<sub>3</sub>N<sub>4</sub> tip may cause the incommensurate contact with graphene. For the given contact area, the commensurate contact often exhibited larger friction force, and hence, larger interfacial shear strength than the case of incommensurate contact.<sup>142</sup> Macroscale interfacial shear strengths of thin film MoS<sub>2</sub>, and graphite were also determined to be about 25-33 MPa,<sup>143</sup> and 17.6 MPa,<sup>144</sup> respectively, while understanding of the interfacial shear strength of thin film h-BN remains very limited. The estimated interfacial shear strengths of these single-layer materials were found to be relatively larger than those of their bulk forms. The difference could be attributed to the puckering effects on frictional behaviors of these atomically thin materials, which was proposed as one of the major reasons for increase in friction as the number of layers decreased. In addition, these elastic

constants used for estimating the interfacial shear strengths were belong to bulk h-BN, MoS<sub>2</sub>, and bi-layer graphene, which are expectedly larger than those of their single-layer materials, therefore, the interfacial shear strengths of single-layer h-BN, MoS<sub>2</sub>, and graphene could be relatively overestimated. Nonetheless, these estimated interfacial shear strengths of single-layer h-BN, MoS<sub>2</sub>, and graphene clearly demonstrate the low friction characteristics of these single-layer materials.

The variation of friction force of single-layer h-BN, MoS<sub>2</sub>, and graphene with respect to normal force obtained using flat-ended tip was shown in Fig. 4.12 (a). The adhesion force between the tip and these single-layer materials determined before and after FFM measurements was also presented in Fig. 4.12 (b), which show the averaged adhesion force of single-layer h-BN, MoS<sub>2</sub>, and graphene was estimated to be about 154.2 nN, 152.3 nN, and 157 nN, respectively, along with the adhesion force change before and after FFM measurements was found to be smaller than 2 %. The adhesion force of these single-layer materials with the flat-ended tip was significantly larger than those sharp tip, which is likely due to the large contact area of flat-ended tip. In addition, the nonlinear dependence between friction force and normal force of these single-layer materials was clearly observed. Furthermore, friction force of single-layer h-BN, MoS<sub>2</sub>, and graphene increased from 1.7 nN to 9.8 nN as the normal force increased from -130 nN to 100 nN, which clearly show the low friction force characteristics of these single-layer materials. Interestingly, the increase in friction force of these single-layer materials with increasing normal force was found to be different with each other, and different with what was observed from the case of sharp tip. Particularly, among three single-layer materials, MoS<sub>2</sub> exhibited the largest friction force, while graphene exhibited the smallest friction force, and friction force of could be found in the between of those of single-layer MoS<sub>2</sub> and graphene across the range of normal force from -130 nN to 100 nN. Furthermore, the degree of increase in friction of single-layer h-BN with increasing normal force

was found to be larger than those of single layer MoS<sub>2</sub> and graphene. For instance, by roughly fitting the linear part of friction force of these single-layer materials in the range of normal force from -50 nN to 100 nN, friction coefficients of single-layer h-BN, MoS<sub>2</sub>, and graphene were estimated to be about 0.024, 0.019, 0.014, respectively. The larger friction of single-layer MoS<sub>2</sub> or the smaller friction of single-layer graphene could be understood based on their different bending stiffness as previously discussed. However, it is not clearly why the degree of increase in friction force with increasing normal force, or friction coefficient, of single-layer h-BN was slightly larger than those of single-layer MoS<sub>2</sub> and graphene.

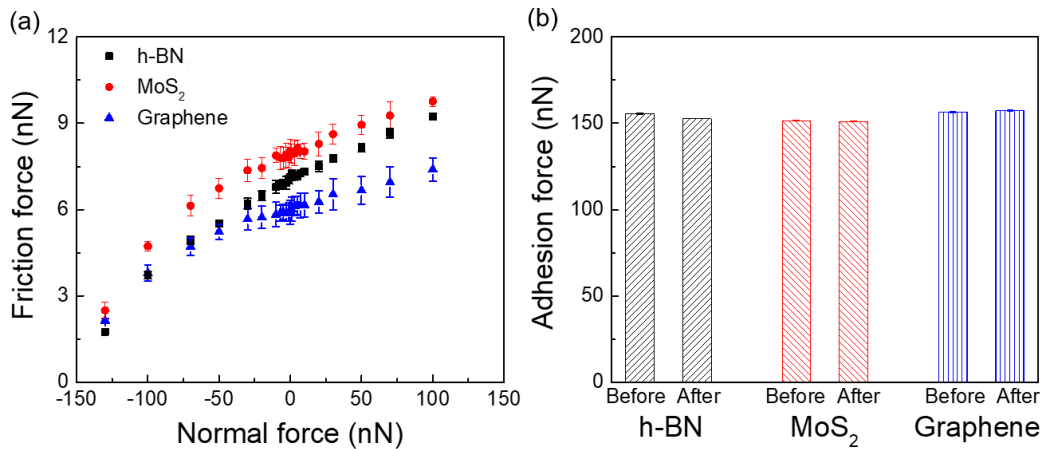


**Fig. 4.12. (a) Variation of friction force as a function of normal force of single layer h-BN, MoS<sub>2</sub> and graphene obtained using flat-ended tip. (b) Variation of adhesion between tip and single-layer h-BN, MoS<sub>2</sub>, and graphene obtained before and after FFM measurements. The error bar corresponds to one standard deviation.**

After careful characterization the correlation between normal force and friction force of single-layer h-BN, MoS<sub>2</sub>, and graphene using two different tip shapes. The effect of sliding speed and environmental conditions on friction force characteristics of these single-layer materials were further investigated. The sharp diamond tip was used due to the availability of theoretical models related to its shape for interpreting the friction data.

### 4.3.3 Effect of sliding speed

Friction force of single-layer h-BN, MoS<sub>2</sub>, and graphene with respect to sliding speed for different normal forces was shown in Fig. 4.13, which clearly demonstrates their speed-dependent friction characteristics. Particularly, based on the results, friction force of single-layer h-BN, MoS<sub>2</sub>, and graphene was found to increase with the increasing sliding speed. The results also show that, after roughly logarithmically increasing with sliding speed, friction force single-layer graphene under 1 nN normal force, or friction force of single-layer MoS<sub>2</sub> under 5 nN and 7 nN normal force reach to the certain values when the sliding speeds were larger than 1,000 nm/s. These behaviors are consistent with the prediction of the thermally activated Prandtl-Tomlinson (PTT) model,<sup>145</sup> which suggested that friction force increased with the increasing sliding speed and decreasing temperature due to the thermal energy.

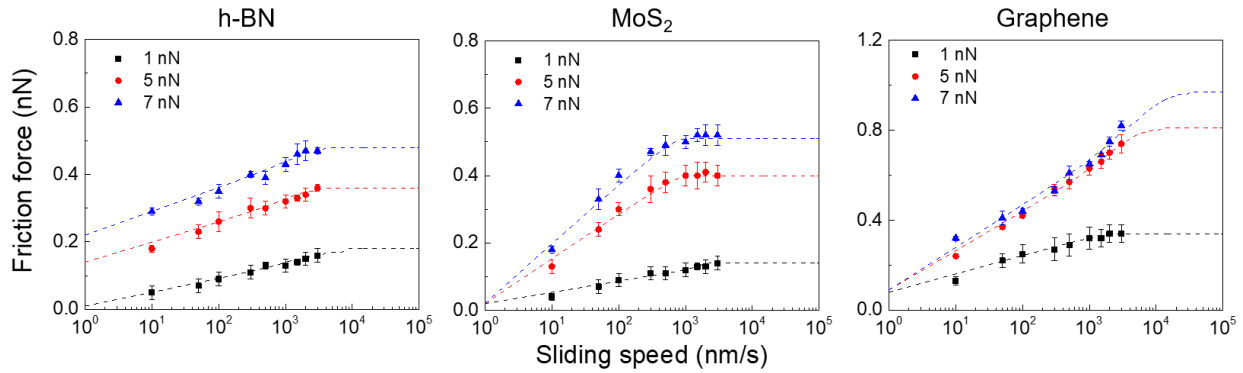


**Fig. 4.13. (a) Variation of friction force as a function of sliding speed for single layer h-BN, MoS<sub>2</sub> and graphene under various normal forces. Friction force data was fitted to the thermally activated Prandtl-Tomlinson (PTT) model using Eq. 4.3. Error bar corresponds to one standard deviation.**

The thermally activated Prandtl-Tomlinson (PTT) model,<sup>145</sup> which described the relationship between friction force and sliding speed as:

$$\frac{1}{\beta k_B T} (F_c - F_f)^{3/2} = \ln \frac{v_0}{v} - \frac{v_0}{v} \frac{1}{2} \ln \left( 1 - \frac{F_f}{F_c} \right), \quad (4.3)$$

In Eq. 4.3,  $\beta$  is the parameter that depends on the shape of the interaction potential,  $k_B$  is Boltzmann's constant,  $T$  is the temperature,  $F_c$  is the friction force at zero temperature, and  $v_0$  is the characteristic speed. Based on PTT model, two different regimes of friction force as a function of sliding speed could be clearly observed, one is the roughly logarithmic increase of friction force with speed when the sliding speed increases up to the critical speed, and the other one is the plateau of friction force when the sliding speed is larger than the critical speed. The above observed sliding speed of about 1,000 nm/s could be considered as the critical speed for friction force of single-layer graphene under 1 nN normal force, and MoS<sub>2</sub> under 5 nN and 7 nN normal force, to reach their plateau regimes, while the critical speed of other cases could not be experimentally observed within the range of sliding speed used in this work. Although this speed-dependent friction characteristic has been often observed on different materials such as mica,<sup>145,146</sup> NaCl (100),<sup>147</sup> Au (111),<sup>148,149</sup> and graphite (0001),<sup>150</sup> however, such observation on single-layer h-BN, MoS<sub>2</sub>, and graphene have not been fully achieved yet.

Hence, to gain better fundamental understanding of the frictional behaviors of these single-layer materials, their speed-dependent friction in Fig. 4.13 was further fit to the PPT model using Eq. 4.3 with  $\beta$ ,  $F_c$ , and  $v_0$  as free parameters.  $\beta$  is the parameter determined by the shape of the lateral interaction potential and is closely related to the rate of increase of friction with sliding speed.  $F_c$  is the friction force at 0 K which is also the friction value at the plateau regime, and  $v_0$  is the characteristic speed. Based on the fitting results, within the range of sliding speed used in FFM measurements, from 10 nm/s to 3,000 nm/s, friction of these single-layer materials could follow the low speed trend very well, which is the logarithmic increase of friction with sliding speed. The fitting also shows that the friction force of single-layer h-BN under 1 nN, 5 nN, and 7 nN normal force could reach to the plateau regime with the critical speed of about 4,000 nm/s, which is similar

to the case of single-layer MoS<sub>2</sub> under 1 nN normal force. While, the critical speed for friction force of single-layer graphene under normal force of 5 nN and 7 nN to reach the plateau is predicted to be in the range 10,000 nm/s to 20,000 nm/s. Although the influence of normal force on critical speed of these single-layer materials was not clearly observed, the critical speed of single-layer MoS<sub>2</sub> were found to be relatively smaller than those of single-layer h-BN, and graphene. According to the PTT model, this result suggests that the sliding friction of AFM tip on surface of single-layer h-BN and graphene could be thermally assisted for larger range of speed than the case of single-layer MoS<sub>2</sub>.

In addition, effects of normal force on the parameters  $\beta$  and  $F_c$  of single-layer h-BN, MoS<sub>2</sub>, and graphene were shown in Figs. 4.14 (a) and (c) respectively, which clearly show that  $\beta$  and  $F_c$  generally increased as the normal force increased. As previously discussed,  $\beta$  is the rate (or slope) of increase in friction with sliding speed, and  $F_c$  is friction force at the plateau regime. As the normal force increased, the increase in  $F_c$  could be expected because of the increase in number of contacting atoms,<sup>151</sup> while the increase in  $\beta$  was proposed to be due to the more corrugated interaction potential with increasing normal force.<sup>145</sup> Particularly, by assuming the interaction potential has a sinusoidal shape, the corrugation of the interaction potential or the effective interaction potential barrier,  $E_0$ , could be determined based on its relationship  $F_c$  as:<sup>145</sup>

$$E_0 = \frac{aF_c}{\pi} \quad (4.4),$$

with the parameter  $\beta_{sin}$ :

$$\beta_{sin} = \frac{3\pi\sqrt{F_c}}{2a\sqrt{2}} \quad (4.5),$$

where  $a$  is the lattice constant. Lattice constants of single-layer h-BN, MoS<sub>2</sub>, and graphene used



for calculation were about 0.25 nm, 0.32 nm, and 0.25 nm respectively. The corrugation amplitude of the interaction potential,  $E_0$ , was estimated using Eq. 4.4 as shown in Fig. 4.14 (d).

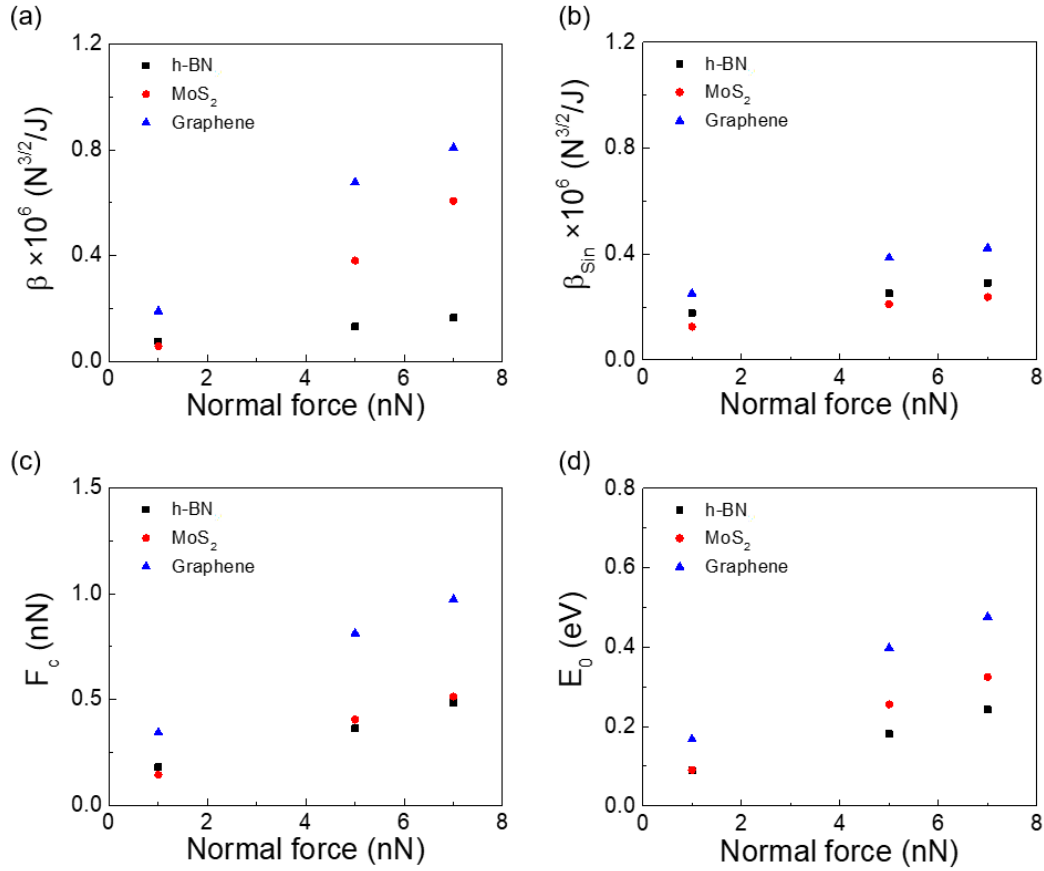


**Fig. 4.14.** Plot of (a)  $\beta$ , (b)  $\beta_{Sin}$ , (c)  $F_c$ , and  $E_0$  as a function of normal force.  $\beta$  is the parameter related to the shape of the lateral interaction potential that govern the rate of increase of friction with sliding speed at low speeds.  $F_c$  is friction force at 0 K.  $\beta$  and  $F_c$  are the results of fitting the sliding speed-dependent friction of single-layer h-BN, MoS<sub>2</sub>, and graphene to PTT model using Eq. 4.3. Assuming the lateral interaction potential exhibit a sinusoidal shape, in which the shape-related parameter  $\beta_{Sin}$  and the corrugation amplitude of the interaction potential  $E_0$  are estimated using Eqs. 4.4 and 4.5, respectively.

The results show that as the normal force increased, the corrugation amplitude of the interaction potential increased. The more corrugated interaction potential was, for a given sliding speed, the more time would be needed to overcome the energy barrier, as the results, the thermal activation

could have stronger influence in the sliding process of atoms leading to the increase in  $\beta$  with increasing normal force.<sup>145</sup> Furthermore, with the assumption the interaction potential of single-layer h-BN, MoS<sub>2</sub>, and graphene have the sinusoidal shapes, the parameter  $\beta_{sin}$  was obtained using Eq. 4.5, and Fig. 4.14 (b) shows the variation of  $\beta_{sin}$  with respect to normal force. By comparing the measured value  $\beta$  with the calculated value  $\beta_{sin}$ , insight into the shape of the interaction potential of these single-layer materials could be achieved. The results show that  $\beta_{sin}$  of single-layer h-BN gradually increased with normal force, which is similar to the behavior of its  $\beta$ . While,  $\beta_{sin}$  of single-layer MoS<sub>2</sub> and graphene were found to increase less rapidly with normal force than the case of their  $\beta$ . These observations clearly suggest that the shape of effective interaction potential of single-layer h-BN was more closed to the sinusoidal shape than those of single-layer MoS<sub>2</sub> and graphene. This finding is important when attempting to understand the fundamental frictional behaviors of these atomically thin materials based on PTT model. For example, with an aim to simplify the contacting interfaces of single-layer MoS<sub>2</sub> and graphene, an act of assuming the sinusoidal shape of the interaction potential without considering the real shape of the interaction potential may lead to the results that are essentially different from the actual friction characteristics of these single-layer materials.

Furthermore, from the practical point of view, the speed-dependent friction of single-layer h-BN, MoS<sub>2</sub> and graphene could further provide useful information of their surface characteristics. For example, based on the dependence between friction force and sliding speed, the surface wettability of these single-layer materials could be characterized. It was found that the partially hydrophilic surface exhibited a logarithmic decrease of friction with increasing speed, and the partially hydrophobic surface showed a logarithmic increase of friction with increasing speed.<sup>152</sup> Hence, according to the logarithmic increase in friction of single-layer h-BN, MoS<sub>2</sub>, and graphene

with increasing sliding speed, surface hydrophobicity of these single-layer materials could be clearly observed. This observation is consistent with these other studies, which recently proved the surface hydrophobicity of single-layer h-BN,<sup>153</sup> MoS<sub>2</sub>,<sup>154</sup> and graphene<sup>155</sup> by using the water contact angle (WCA) measurements. As nanoscale protective and solid lubricant coating layers, these single-layer layer materials with the surface hydrophobicity could help to reduce the effect of water condensation at the contacting interfaces. Apart from the surface wettability, considering wear rate and shear stress of these atomically thin materials could be increased with increasing sliding speed,<sup>156</sup> therefore, the speed-dependent friction characteristics of single-layer h-BN, MoS<sub>2</sub>, and graphene found in this work suggest that the sliding speed of the mechanical moving part coated by these single-layer materials should be reasonably small to reduce the friction generated at the contacting interfaces, and eventually to save the energy and enhance the lifetime of the nanoscale devices.

## **4.4 Effect of environmental conditions**

### **4.4.1 Effect of relative humidity**

The effect of humidity on friction characteristics of single-layer h-BN, MoS<sub>2</sub>, and graphene was further investigated by conducting FFM measurements under various relative humidity, ranging from 5 % to 75 %. The humidity-dependent friction force of these single-layer materials with respect to normal force and sliding speed was shown in Figs. 4.15 (a) and (b), respectively. The friction results shown in Fig. 4.15 (a), the sliding speed was set to 375 nm/s and the normal force was varied in the range from -1 nN to 50 nN. The negative normal forces correspond to the adhesive regime of tip and surface of materials. While friction results shown in Fig. 4.15 (b), the normal force was set to 7 nN and the sliding speed was varied in the range from 10 nm/s to 3,000 nm/s.

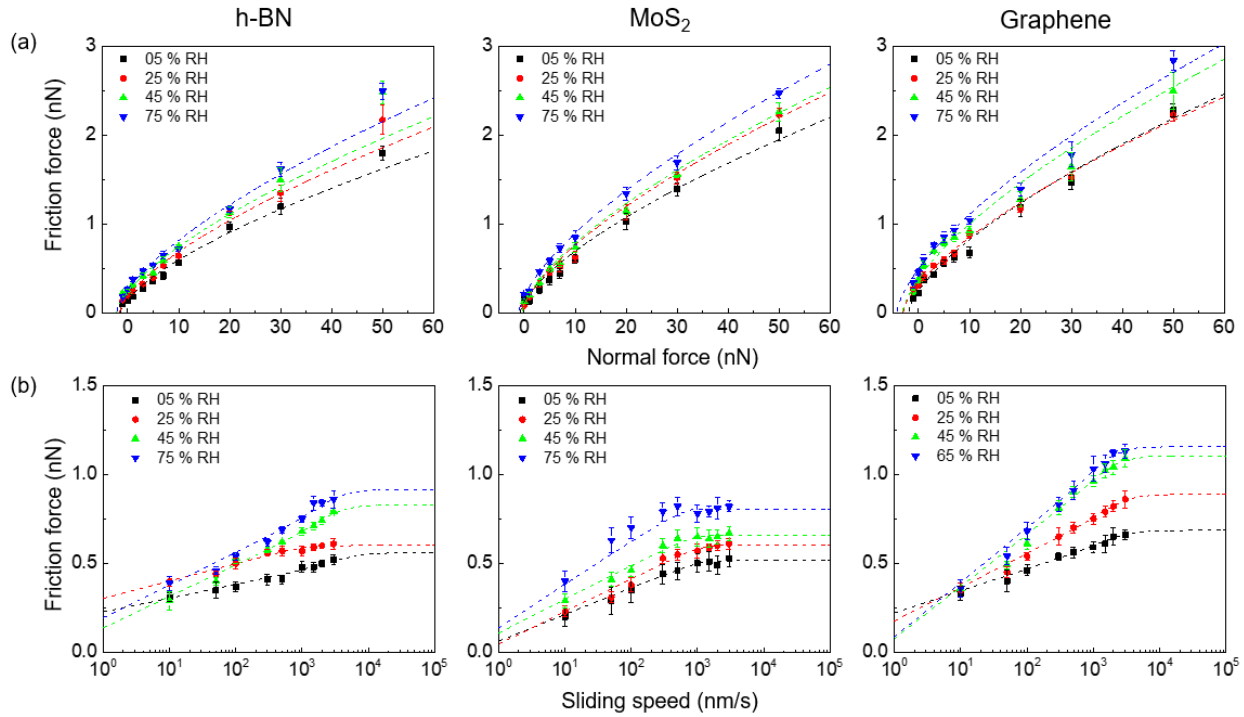


**Fig. 4.15.** Variation of friction as a function of (a) normal force and (b) sliding speed under different relative humidity (5% RH, 25% RH, 45% RH and 75% RH) for single-layer h-BN, MoS<sub>2</sub> and graphene. In panel a, the sliding speed was set to 375 nm/s and the friction force data was fitted to HPO model using Eq. 4.1. In panel b, the normal force was set to 7 nN and friction force data were fitted to PTT model using Eq. 4.3. The error bar corresponds to one standard deviation.

The results show that under given normal force and sliding speed, friction force of these single-layer materials was found to increase with increasing relative humidity, despite having the hydrophobic surfaces based on their speed-dependent friction characteristics found in this work or from the WCA measurements reported in the literature. Fig. 4.15 (a) shows the non-linear dependence between normal force and friction force of these single-layer materials under various relative humidity, and the degree of friction force increased with increasing normal force was also found to generally increase, as the relative humidity increased. In addition, interfacial shear strengths of these single-layer materials were also estimated by fitting the normal force-dependent friction to HPO model using Eq. 4.1 as shown in Fig. 4.16 (a). The results clearly show the

interfacial shear strengths of single-layer h-BN, MoS<sub>2</sub>, and graphene generally increased with increasing relative humidity.

Furthermore, Fig. 4.15 (b) clearly shows the logarithmic increase in friction of single-layer h-BN, MoS<sub>2</sub>, and graphene with increasing sliding speed, and such speed-dependent friction characteristics were observed at all different relative humidity. From the results, only the critical speed of single-layer MoS<sub>2</sub> were experimentally observed within the range of sliding speed used in this work, which was found in the range from 1,000 nm/s to 2,000 nm/s. The speed-dependent friction of these single-layer materials were further fitted to the PTT model using Eq. 4.3. Based on the fitting results, the critical speed of single-layer h-BN and graphene were predicted to be in the range of about 8,000 nm/s-10,000 nm/s and 4,000 nm/s-9,000 nm/s, respectively. This fitting result also showed that critical speed of single-layer MoS<sub>2</sub> was smaller than those of single-layer h-BN and graphene. In addition, no significant change in critical speed of these single-layer materials with respect to relative humidity was clearly observed. In contrast, as shown in Figs. 4.16 (b) and (c), these parameters  $F_c$  and  $\beta$ , respectively, of single-layer h-BN, MoS<sub>2</sub>, and graphene were found to increase with increasing relative humidity, which indicated that the friction at plateau regime and the rate of increase in friction with sliding speed of these single-layer materials increased with increasing relative humidity. Furthermore, considering the proportional relationship between  $F_c$  and  $E_0$  (Eq. 4.4), this increase in  $F_c$  and  $\beta$  implies increase in corrugation of the interaction potential of these single-layer materials with increasing relative humidity.

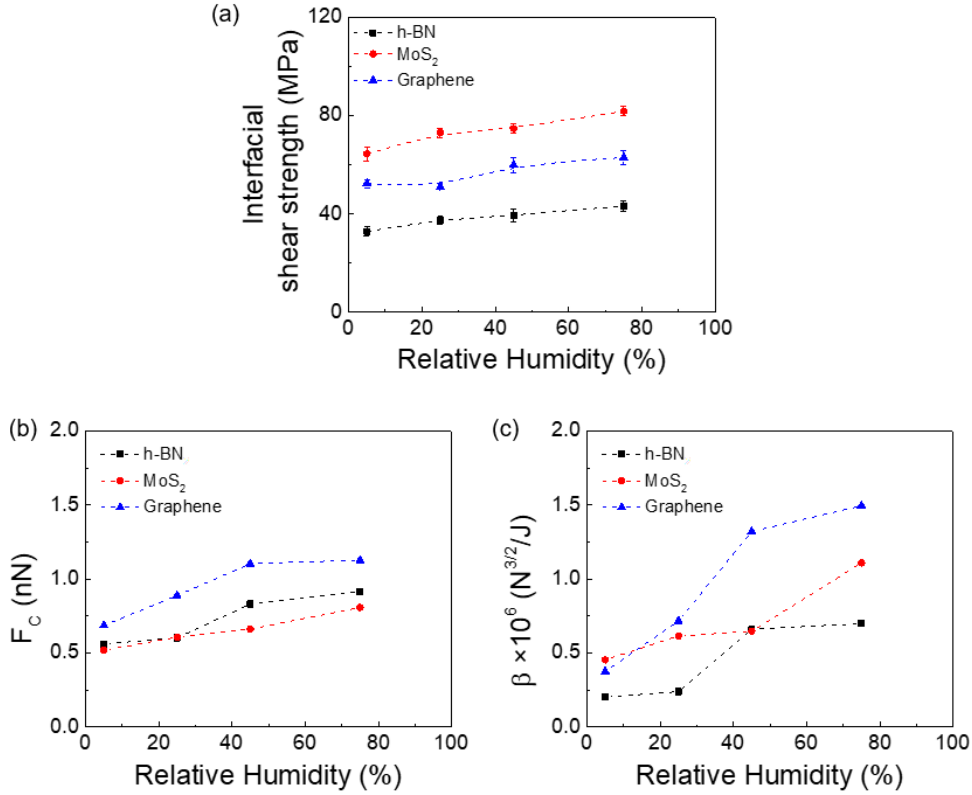


**Fig. 4.16.** Variation of (a) interfacial shear strength, (b)  $F_c$ , and (c)  $\beta$  as a function of relative humidity for single-layer h-BN, MoS<sub>2</sub>, and graphene. Interfacial shear strength was estimated by fitting the normal force-dependent friction data to the HPO model using 4.1.  $F_c$  and  $\beta$  were estimated by fitting the sliding speed-dependent friction data to the PTT model using Eq. 4.3. The dashed line is the guide to eye.

Early research demonstrated that friction force of graphite was high in dry or vacuum environments, while low in humid environment, these behaviors were proposed to be as the results of adsorbed layers of vapors, such as water, at the sliding interfaces.<sup>157</sup> MoS<sub>2</sub>, despite having a very similar lamellar structure, demonstrated the completely different humidity-dependent friction characteristics with those of graphite. Particularly, friction force of MoS<sub>2</sub> was found increased with increasing humidity, while remained low in vacuum environments. The interaction of water between planes of MoS<sub>2</sub> during contact sliding was found to be responsible for this behavior.<sup>158</sup> These observations of the environment-dependent friction of graphite and MoS<sub>2</sub> clearly

highlighted the important and different role of water interactions in friction characteristics of these layered materials. However, the understanding of these water interactions in nanoscale friction characteristics of single-layer materials is still very limited.<sup>159</sup> Assuming that a water layer could be possibly formed on top surface of single-layer h-BN, MoS<sub>2</sub>, and graphene at certain threshold relative humidity, the capillary force at the interface between tip and surface of these single-layer materials due to the formation of water meniscus could significantly affect the friction force measurements. The adhesion force between single-layer h-BN, MoS<sub>2</sub>, and graphene with AFM tip were carefully monitored before and after FFM measurements under various relative humidity as shown in Fig. 4.17. The results show that no significant change in adhesion force was observed at different relative humidity. In addition, from Fig. 4.15 (b) the logarithmic increase in friction with increasing speed of these single-layer materials was consistently observed across the range of relative humidity. Hence, based on these observations, the water adsorption on the top surface of these single-layer materials was not likely occurred and the capillary force may be not responsible for the observed increase in friction force of these single-layer materials with increasing relative humidity.

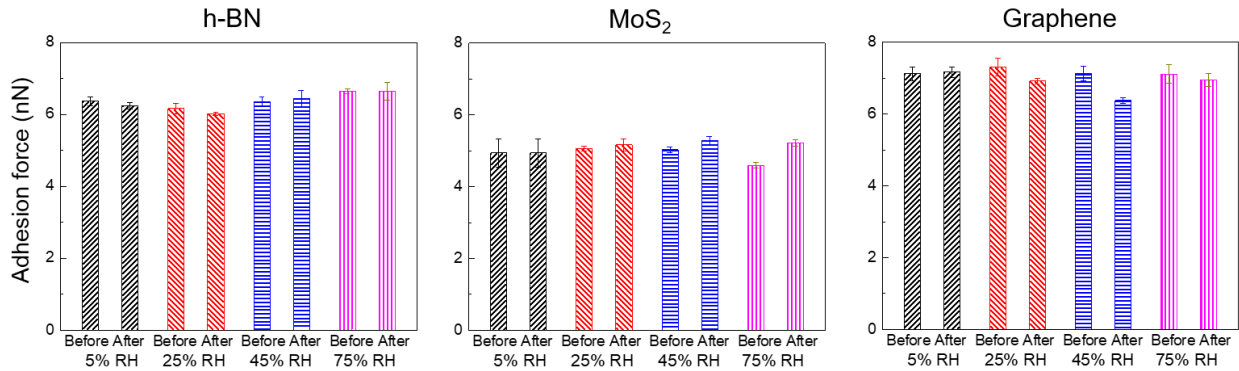


**Fig. 4.17. Variation of adhesion forces between AFM tip and the single-layer h-BN, MoS<sub>2</sub> and graphene materials obtained before and after friction force measurement under various relative humidity.**

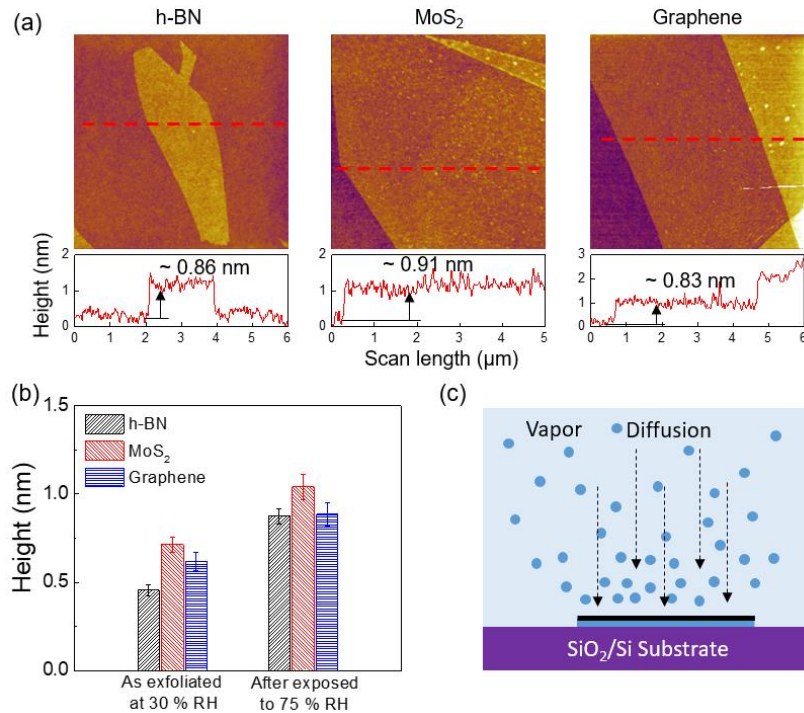


**Fig. 4.18. (a) Topographic images of single-layer h-BN, MoS<sub>2</sub> and graphene after FFM under 75% RH. (b) Estimated thickness of single-layer materials before and after FFM measurements. (c) Schematic of the water diffusion into the interface between the atomically thin material and its underlying substrate. The topographic images were obtained from the intermittent –contact mode AFM, the cross-sectional profiles are included in panels a. The red-dashed lines indicate the location where the cross-sectional profiles are taken.**

Topographic images of single-layer h-BN, MoS<sub>2</sub>, and graphene after FFM measurements at 75 % RH were obtained as shown in Fig. 4.18 (a) along with the cross-section height profiles. Based on the cross-sectional height profile, thickness of single-layer h-BN, MoS<sub>2</sub>, and graphene were determined to be about  $0.88 \pm 0.04$  nm,  $1.04 \pm 0.07$  nm, and  $0.88 \pm 0.07$  nm, respectively. By comparing the thicknesses of these single-layer materials obtained after mechanical exfoliation at about 30 % RH with those obtained again after FFM measurement at 75 % RH, as presented in Fig. 4.18 (b), a significant increase in thickness of these single-layer materials after exposing to humid environment could be clearly observed. This behavior could be because of water diffusion at the interface between these single-layer materials and their underlying SiO<sub>2</sub> substrates, which



was recently found by several studies.<sup>160-162</sup> Particularly, these studies demonstrated that water molecules could diffuse into the interface between single-layer graphene and SiO<sub>2</sub> substrate at humid environment and form an ice-like water adlayer leading to an increase in thickness of these single-layer materials, as shown in Fig. 4.18 (c).<sup>160,161</sup> And a few particles were randomly observed from the topographic images of single-layer MoS<sub>2</sub> and graphene, which were suggested as the formation of the water droplets on SiO<sub>2</sub> substrate through the water diffusion process.<sup>160</sup> In addition, the mechanical properties of multi-layer graphene were found to be significantly affected by relative humidity. Particularly, the loss tangent, closely related to the internal damping, of multi-layer graphene significantly decreased with increasing relative humidity, which was proposed due to the formation of the ice-like water adlayers at the interface between graphene and SiO<sub>2</sub> substrate.<sup>161</sup> Considering the close relationship between mechanical and frictional properties of these single-layer materials, therefore the formation of ice-like water adlayers could also affect their frictional behaviors. In fact, the presence of the ice-like water adlayers at the interface between single-layer materials and their underlying SiO<sub>2</sub> substrates could expectedly increase the distance, and as a result, decrease the adhesion strength between layer and substrate, which could significantly affect friction characteristics of these single-layer materials.<sup>83,86</sup> Particularly, as the adhesion strength to the substrate decreased, these single-layer materials are more easily to snap in the sliding tip and locally pucker, leading to the increasing of friction.<sup>83</sup> Based on these observations from literature, we hypothesize that the humidity-dependent friction of single-layer h-BN, MoS<sub>2</sub>, and graphene is due to the water diffusion at the interface between these single-layer materials and their underlying SiO<sub>2</sub> substrates, which lead to the decrease in adhesion strength to substrate of these single-layer materials, and eventually the puckering effect can have a stronger influence in their frictional behaviors.

#### 4.4.2 Effect of thermal annealing

The effect of thermal annealing on friction force of single-layer h-BN, MoS<sub>2</sub>, and graphene were further investigated. Friction force of these single-layer materials were measured after mechanical exfoliation in ambient conditions (25 °C, 30 % RH), as a function of normal force and sliding speed. These single-layer materials then went through the thermal annealing process as described in Experimental Section. To avoid the possibility that water could diffuse back into the interface between these single-layer materials and their underlying substrates after thermal annealing, FFM measurements of these thermally annealed single-layer materials were conducted once the temperature reach to room temperature, with the relative humidity of about 30 %. Friction force of single-layer h-BN, MoS<sub>2</sub>, and graphene, obtained before and after thermal annealing process, as a function of normal force and sliding speed was shown in Figs. 4.19 (a) and (b), respectively. The results clearly show that the friction force of single-layer h-BN, MoS<sub>2</sub>, and graphene, under given normal force and sliding speed, was effectively reduced after the thermal annealing process. Particularly, the normal force-dependent friction force of these single-layer materials from Fig. 4.19 (a) clearly demonstrated the degree of increase in friction with increasing normal force of these single-layer materials significantly decreased after thermal annealing. By fitting these friction to the HPO model using Eq. 4.1, the interfacial shear strengths of single-layer h-BN, MoS<sub>2</sub> and graphene obtained after thermally annealed were estimated to be about 27.1 MPa, 59.3 MPa, and 22.3 MPa, respectively, which decreased of about 25.4 %, 33.0 %, and 36.7 % compared with those before thermal annealing, respectively. In addition, based on the speed-dependent friction of single-layer h-BN, MoS<sub>2</sub>, and graphene obtained before and after thermal annealing as shown in Fig. 4.19 (b), the rate of increase friction with increasing sliding speed,  $\beta$ , and the friction force at 0 K,  $F_c$ , of these single-layer materials also generally decreased after

thermal annealing. The observed friction decrease after thermal annealing could be attributed to the water diffused out of the interfaces between these single-layer materials and their underlying substrate. It should be noted that the effect of thermal annealing on friction characteristics of single-layer h-BN, MoS<sub>2</sub>, and graphene were investigated using separately prepared set of materials under ambient conditions. Therefore, a small amount of water molecule could be inevitably trapped between these single-layer materials and their substrate.

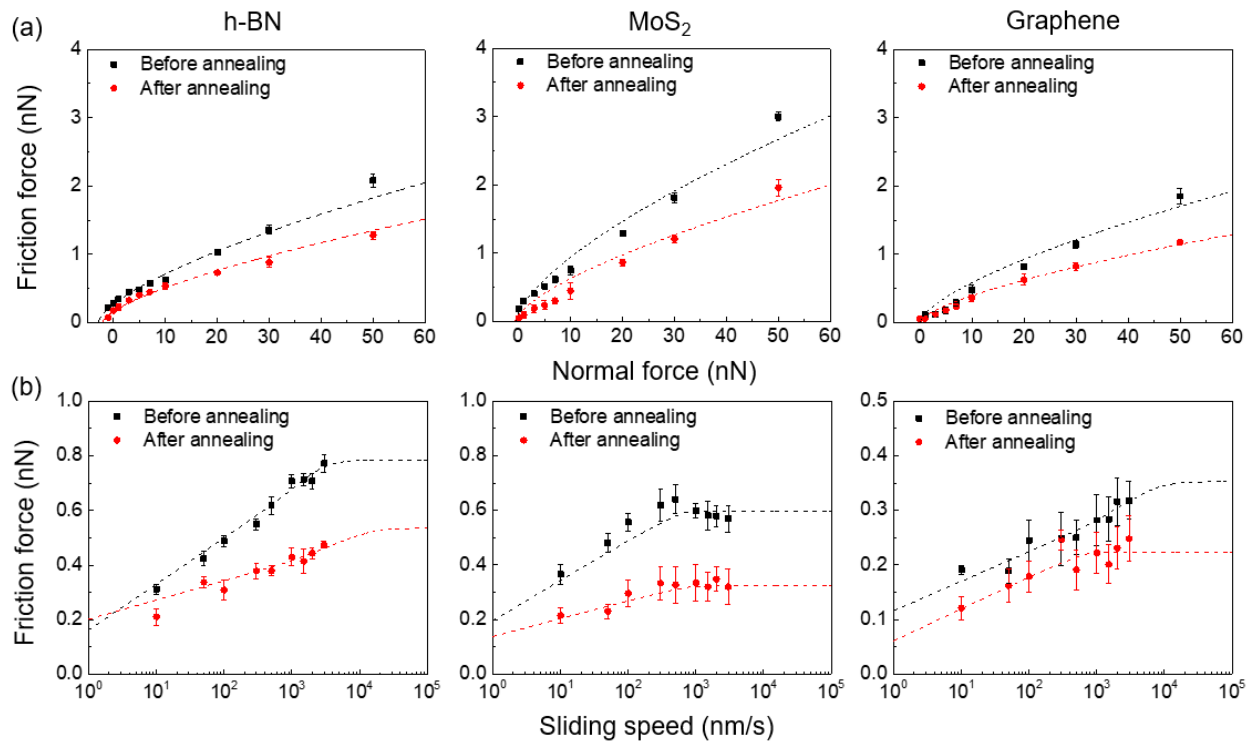


**Fig. 4.19.** Variation of friction force as a function of (a) normal force and (b) sliding speed for single-layer h-BN, MoS<sub>2</sub> and graphene, before and after thermal annealing process. In panel a and b, friction force data was fitted to the HPO model using Eq. 4.1 and the PTT model using Eq. 4.3, respectively. The error bar corresponds to one standard deviation.

### 4.4.3 Effect of temperature

Friction force of single-layer h-BN, MoS<sub>2</sub>, and graphene at given temperature, such as 50 °C, 75 °C, and 100 °C was also determined as shown in Fig. 4.20. However, unlike the effect of relative humidity on friction force with clear trend was observed, temperature-dependent friction force of these single-layer materials was found to be significantly scattered, even with the same material the under different normal force, the temperature affected its friction differently. The effect of temperature on phonon frequencies, and the effect of strain induced by the mismatch of the thermal expansion coefficients between single-layer materials and their underlying substrates on the phonon dispersion should be carefully characterized when the temperature of single-layer materials deposited on substrates was changed.<sup>163</sup> Since the complex effect of temperature on the phononic behaviors of single-layer h-BN, MoS<sub>2</sub>, and graphene, therefore the dependence of their frictional behaviors on temperature is also expected to be complicated.<sup>16</sup> However, due to the importance for fundamental understanding and practical application of these single-layer materials, their temperature-dependent friction characteristics should be further explored.

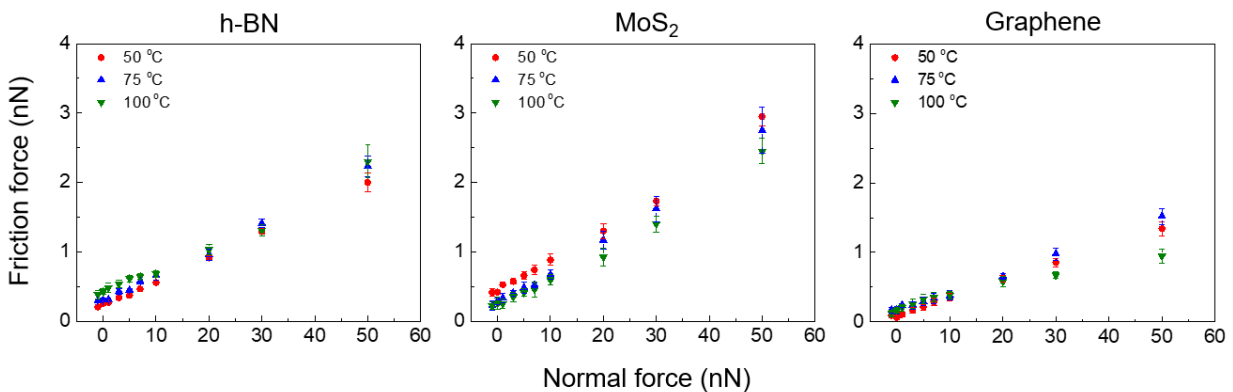


**Fig. 4.20.** Variation of friction force as a function of normal force under different temperature (50 °C, 75 °C, and 100 °C) for single-layer h-BN, MoS<sub>2</sub> and graphene. The sliding speed was set to 375 nm/s. The error bars correspond to one standard deviation.

## 4.5 Summary

In summary, friction characteristics of single-layer h-BN, MoS<sub>2</sub>, and graphene were systematically investigated using FFM measurements under various conditions. From the results, the contributions of topography, normal force, sliding speed, relative humidity, and thermal annealing to frictional behaviors of these single-layer materials were clearly observed. Particularly, it was found that the topography-induced friction fluctuation in friction loops, and this friction fluctuation increased with increasing normal force. In addition, the effect of topography on friction of these single-layer materials could not be eliminated by the subtraction of trace and retrace friction profiles. Furthermore, based on ratchet mechanism, the effect of surface slope on friction force measurements was found to be dominant when the radius of tip was relatively small compared with the surface roughness, therefore this topography-induced contribution on friction of these single-layer materials was effectively reduced when the flat-ended tip with significantly large contact area was used in FFM measurement.

Low friction characteristics of these single-layer materials were observed from the normal force-dependent friction results, based on which their interfacial shear strengths was also estimated using HPO model. The differences in adhesion characteristics and mechanical properties was found to be responsible for different degree of increase in friction with normal force of these single-layer materials. From the speed-dependent friction results, the logarithmic increase in friction with sliding speed of single-layer h-BN, MoS<sub>2</sub>, and graphene were clearly observed. The degree of increase in friction with sliding speed was also found to generally increase as normal force increased. In addition, based on the PTT model, we found that the effective shape of the interaction potential of single-layer h-BN was more similar to the sinusoidal shape than those of single-layer MoS<sub>2</sub> and graphene. Furthermore, for the application as nanoscale protective and solid lubricant

coating layers, the increase in friction with sliding speed suggests that these single-layer materials should be operated at reasonably low speed to primarily reduce the friction generated at contacting interfaces.

The effects of environmental conditions such as relative humidity and thermal annealing on friction characteristics of single-layer h-BN, MoS<sub>2</sub>, and graphene were also investigated. From the humidity-dependent friction results, friction force of these single-layer materials generally increased with increasing relative humidity, while no significant change in adhesion force across the range of relative humidity was clearly observed. As relative humidity increased, the water molecules increasingly diffuse into the interface of single-layer h-BN, MoS<sub>2</sub>, and graphene with their underlying substrates, leading to decrease in adhesion strength to the substrate of these single-layer materials, as a result the influence of puckering effect on frictional behaviors of these single-layer materials increased. This behavior was proposed as the main mechanism for humidity-dependent friction characteristics of these single-layer materials. The effect of thermal annealing on friction of single-layer h-BN, MoS<sub>2</sub>, and graphene was also observed, the results clearly showed the significant decrease in friction of these single-layer materials after being thermally annealed. The water molecules could be effectively diffused out of the interface between these single-layer materials and their substrate because of the thermal annealing process, which is likely responsible for the decrease in friction of the thermally annealed materials. The effects of relative humidity and thermal annealing on friction characteristics of single-layer h-BN, MoS<sub>2</sub>, and graphene clearly highlighted the important role of water interactions on frictional behaviors of these single-layer materials. The humidity-dependent friction results suggest that these single-layer materials as the protective and solid lubricant coating layers for nanoscale devices should be operated in dry conditions to prolong the lifetime of systems. In addition, the simple thermal annealing process

could improve the frictional behaviors of these single-layer materials by reducing the amount of water molecules trapped at the interface. Hence, this thermal annealing process could be used for many practical applications such as stabilization, packaging, and storage of the nanoscale devices-based on these single-layer materials.

## Chapter 5

### Conclusions and Recommendations

#### 5.1 Conclusions of the Research

Atomically thin materials, such as single- and a few-layer h-BN, MoS<sub>2</sub>, and graphene, have been demonstrated to have a great potential as protective and solid lubricant coating layers for nanoscale devices. These coating layers are often used to improve the tribological performance including surface damage resistance, friction force reduction, at the contacting interfaces between these mechanical moving parts in the systems. Therefore, to prolong the lifetime of the high-performance nanoscale mechanical systems, the tribological characteristics of atomically thin h-BN, MoS<sub>2</sub>, and graphene should be fully understood. In this research, the surface damage and friction force characteristics of atomically thin h-BN, MoS<sub>2</sub>, and graphene were systematically investigated using several AFM-based approaches as presented in the previous chapters. Based on these observations, the following conclusions were drawn:

1. Adhesion strength to substrate of the coating layers could be considered as one of the most important factors that greatly influence the tribological performance of the coating layers, in which the stronger the coating layers adhere to the substrate, the better their tribological performances could be. Hence, the adhesion strength to substrate of single- and a few-layer h-BN, MoS<sub>2</sub>, and graphene were carefully evaluated based on their critical forces obtained from the progressive force scratch test. The results suggested that these atomically thin films were strongly adhered to their substrates, which in-turn significantly improve the load carrying capacity of the underlying substrate. In addition, single-layer graphene was found to have stronger adhesion strength to substrate than those of single-layer h-BN and MoS<sub>2</sub>. Furthermore, as the number of layer increased, not only the critical force of these atomically thin materials generally increased, but also their



surface damage resistance was significantly enhanced, which clearly indicated that the tribological performance of atomically thin h-BN, MoS<sub>2</sub>, and graphene could be effectively enhanced by reasonably using the thicker coating layers.

2. Surface damage characteristics of single-layer h-BN, MoS<sub>2</sub>, and graphene were further investigated using the constant force scratch tests. In the constant force scratch test, these single-layer materials were scratched at the defined areas under given normal force, and the scratched areas were then carefully examined using AFM and Raman spectroscopy measurements. Based on the results, the evolutions of surface damage of single-layer h-BN, MoS<sub>2</sub>, and graphene with respect to normal force were clearly observed. In general, the surface damage of these single-layer materials could be defined as the layer removal process, which is initiated from the (i) elastic deformation of the thin film/substrate system under relatively low normal force, to the (ii) defect formation or plastic deformation and propagation in the thin film structure as the normal force increased, and to the (iii) total removal of the thin film when the critical force was reached. The three-stage surface damage characteristics of single-layer h-BN, MoS<sub>2</sub>, and graphene were found to be strongly dependent on their own normal force carrying capacities. In stage (i), these single-layer materials were found to be intact after scratch test under relatively low normal force with no significant defect or plastic deformation was found. Under these condition of normal force, these single-layer materials were expected to offer their best tribological performance in a very long period of time. However, it should be noted that the compressive strains were found to be likely accumulated in the lattice structure of single-layer h-BN and graphene, which could potentially alter their strain-related material properties. In stage (ii), as the normal force increased, defect formation and plastic deformation were found at the scratched areas of these single-layer materials. Although these thin films were not torn-off and the substrate were not exposed yet, the topography,

friction force, as well as crystalline quality and mechanical strengths of these single-layer materials were permanently affected, which may in turn significantly degrade their tribological performances. In stage (iii), as the normal force reached to the critical force of single-layer h-BN, MoS<sub>2</sub>, and graphene, these single-layer materials were found to be totally failed with the exposure of the substrate. The commonly observed residual compressive strains at the scratched areas could further shed the light on the determination of the failure mechanism of these single-layer materials. The residual strains observed at scratched areas may suggest the scratch tests-induced in-plane compressive strains were dominant over tensile strains, thereby leading to the buckling formation of these atomically thin materials mostly in front of the scratching tip and eventually failure with sufficient strains. These behaviors could be considered as the general failure mechanism of these atomically thin materials due to scratch test.

3. As the number of layer increased, the tribological performances of atomically thin h-BN, MoS<sub>2</sub>, and graphene were found to be significantly increased. The adhesion strengths to the substrate, surface damage resistance, and friction force reductions of these atomically thin materials were effectively improved with the increasing number of layers. These observations clearly indicated that the tribological performances of these nanoscale protective and solid lubricant coating layers based on these atomically thin materials could be effectively enhanced by reasonably using the thicker coating layers.

4. Friction characteristics of single-layer h-BN, MoS<sub>2</sub>, and graphene were further investigated using FFM measurements under various conditions without introducing any notable surface damage to these single-layer materials. These conditions were applied in the FFM measurements to investigate the fundamental friction characteristics of single-layer h-BN, MoS<sub>2</sub>, and graphene as a function of normal force, sliding speed, and environmental conditions. Based on the FFM

measurement results obtained using sharp diamond tip, friction force fluctuation of these single-layer materials was found to significantly increase with increasing normal force. While, the friction force fluctuation of these single-layer materials were considerably reduced when the using the flat-ended tip in FFM measurements. These behaviors were likely attributed to the effect of surface slope on nanoscale friction force measurements, in which the friction force increased or decreased, proportionally with normal force, when the tip ascended or descended the surface slope, respectively, such behaviors were known as the ratchet mechanisms of friction. Based on ratchet mechanism, the effect of surface slope on friction force measurements was found to be dominant when the radius of tip was relatively small compared with the surface roughness, therefore the effect of surface slope on friction force of these single-layer materials effectively reduced when the flat-ended tip with significantly large contact area was used in FFM measurement.

5. The variations of friction force as a function of normal force obtained using both sharp tip and flat-ended tip clearly demonstrated the low friction force characteristics of single-layer h-BN, MoS<sub>2</sub>, and graphene. The nonlinear dependence of friction force on normal force of these single-layer materials was also clearly observed. In addition, the normal force-dependent friction of these single-layer materials was found to be slightly different from each other, such differences could be attributed to the difference in adhesion force between tip and surface of materials and the difference in mechanical responses of these single-layer materials during contact sliding.

6. Speed-dependent friction characteristics of single-layer h-BN, MoS<sub>2</sub>, and graphene were further investigated. The results clearly demonstrated the strong dependence of friction of these single-layer materials on sliding speed. Particularly, friction force obtained under relatively slow speed was found to roughly logarithmically increase with speed, while as the speed used for FFM measurements larger than the threshold speed value, or critical speed, the friction force of these

single-layer materials was found to be independent with speed. These behaviors were likely attributed to the effect of thermal activation on the motion of the sliding tip on relatively flat surface, as previously described by PTT model. By fitting the speed-dependent friction force of these single-layer materials to the PTT model, some fundamental parameters such as the critical friction force and the amplitude of the potential energy profile of single-layer h-BN, MoS<sub>2</sub>, and graphene could also be estimated. These parameters could give some insight of the sliding friction characteristics of these single-layer materials. In addition, the observed speed-dependent friction characteristics of single-layer h-BN, MoS<sub>2</sub>, and graphene also indicated the surface hydrophobicity of these single-layer materials.

7. The effect of environmental conditions on friction of these single-layer h-BN, MoS<sub>2</sub> and graphene further demonstrated the strong dependence between their friction force and relative humidity. Particularly, friction force was found to be increased with increasing relative humidity, while adhesion force was not significantly changed across the range of the relative humidity. The water diffusion into the interface between these single-layer materials and underlying substrate was proposed to be responsible for this behavior. Hence, as water effectively diffused out of the interface between single-layer materials and substrates after thermal annealing process, friction was significantly decreased. These observations clearly highlighted the importance role of water interactions on frictional behaviors of these single-layer materials. The increase in friction, and possibly decrease in adhesion strength to the underlying substrates, of these single-layer materials with increasing relative humidity could significantly affect their tribological performances. Hence, the nanoscale protective and solid lubricant coating layers based on these single-layer materials should be operated in dry environments to prolong the lifetime of nanoscale devices.

## 5.2 Recommendations for future work

Overall, the distinctive surface damage characteristics, the general failure mechanism, and several factors that could strongly influence friction characteristics of atomically thin h-BN, MoS<sub>2</sub>, and graphene were systematically found in this research. These findings would be useful for the design of effective and reliable nanoscale protective and solid lubricant coating layers based on these materials. Although significant amount of work on tribological properties of these atomically thin materials has been done in this work, some interesting and important future research topics still remain to further implement these atomically thin materials as protective and solid lubricant coating layers for nanoscale devices, which will be described in following sections:

1. To elucidate the implementation of the atomically thin h-BN, MoS<sub>2</sub>, and graphene as a protective and solid lubricant coating layers for high-performance nanoscale devices, their qualifications of tribological stability are crucial and should be well established. Generally, the tribological stability of these atomically thin materials can be defined as the ability to endure normal force over a long period of time during contact sliding while maintaining their beneficial lubrication. The observation of how long these atomically thin materials will last under various conditions would be useful for the practical design of these nanoscale protective and solid lubricant based on these atomically thin materials.

2. Based on the surface damage characteristics of atomically thin h-BN, MoS<sub>2</sub>, and graphene found in this research, each material exhibited different surface damage behavior, prior to the total failure. Particularly, although single-layer graphene could endure significant amount of normal force during scratch tests, the underlying substrate was found to be easily deformed. While, although single-layer MoS<sub>2</sub> exhibited relatively less endurance than the case of graphene, MoS<sub>2</sub> could prevent the underlying substrate from plastic deformation more effective than graphene.

These observations imply that the effective nanoscale protective and solid lubricant coating layers could not be made of by merely one particular material. With the emergence of the heterostructure structure by stacking these atomically thin materials vertically, the tribological performance of the nanoscale protective and solid lubricant coating layers could be further optimized by combining the advantages and eliminating the disadvantages of tribological performance of these component atomically thin materials.

3. Single- and a few-layer h-BN, MoS<sub>2</sub>, and graphene used in this research were all prepared using the mechanical exfoliation methods, which could be consider as the simplest method for producing atomically thin materials. Although mechanical exfoliation method could produce atomically thin materials with remarkably high quality such as clean surface and defect free, which leading to numerous exciting discoveries regarding their remarkable material properties, this method is significantly limited when the large production efficiency and large material area were needed. Therefore, to commercially implement these atomically thin materials as nanoscale protective and solid lubricant coating layers, other fabrication methods which could effectively overcome these aforementioned limitations of mechanical exfoliation method are inevitable. Several promising approaches, including lithium intercalated-assisted exfoliation, liquid exfoliation, physical vapor deposition, chemical vapor deposition, thermal annealing, laser thinning and plasma, have been proposed. Among these techniques, chemical vapor deposition growth method was found to be the most promising technique to produce large-scale production of these atomically thin materials. Therefore, by using the mechanical exfoliated materials as the references, comprehensive investigating the tribological performances of CVD-grown atomically thin h-BN, MoS<sub>2</sub>, and graphene would be the essential step to further elucidate the implementation of these atomically thin materials as the nanoscale protective and solid lubricant coating layers.

## References

- (1) Lin, Y.; Connell, J. W. Advances in 2D boron nitride nanostructures: nanosheets, nanoribbons, nanomeshes, and hybrids with graphene. *Nanoscale* **2012**, *4*, 6908-6939.
- (2) Novoselov, K. S. Graphene: Materials in the Flatland (Nobel Lecture). *Angewandte Chemie International Edition* **2011**, *50*, 6986-7002.
- (3) Radisavljevic B.; Radenovic A.; Brivio J.; Giacometti V.; Kis A. Single-layer MoS<sub>2</sub> transistors. *Nat Nano* **2011**, *6*, 147-150.
- (4) Spanu, L.; Sorella, S.; Galli, G. Nature and Strength of Interlayer Binding in Graphite. *Phys. Rev. Lett.* **2009**, *103*, 196401.
- (5) Li, H.; Wang, J.; Gao, S.; Chen, Q.; Peng, L.; Liu, K.; Wei, X. Superlubricity between MoS<sub>2</sub> Monolayers. *Adv Mater* **2017**, *29*, 1701474-n/a.
- (6) Falin, A.; Cai, Q.; Santos, E. J. G.; Scullion, D.; Qian, D.; Zhang, R.; Yang, Z.; Huang, S.; Watanabe, K.; Taniguchi, T.; Barnett, M. R.; Chen, Y.; Ruoff, R. S.; Li, L. H. Mechanical properties of atomically thin boron nitride and the role of interlayer interactions. **2017**, *8*, 15815.
- (7) Bertolazzi, S.; Brivio, J.; Kis, A. Stretching and Breaking of Ultrathin MoS<sub>2</sub>. *ACS Nano* **2011**, *5*, 9703-9709.
- (8) Lee, C.; Wei, X.; Kysar, J. W.; Hone, J. Measurement of the Elastic Properties and Intrinsic Strength of Monolayer Graphene. *Science* **2008**, *321*, 385-388.
- (9) Kostoglou, N.; Polychronopoulou, K.; Rebholz, C. Thermal and chemical stability of hexagonal boron nitride (h-BN) nanoplatelets. *Vacuum* **2015**, *112*, 42-45.
- (10) Kim, K.; Regan, W.; Geng, B.; Alemán, B.; Kessler, B. M.; Wang, F.; Crommie, M. F.; Zettl, A. High-temperature stability of suspended single-layer graphene. *physica status solidi (RRL) – Rapid Research Letters* **2010**, *4*, 302-304.
- (11) Chen, S.; Brown, L.; Levendorf, M.; Cai, W.; Ju, S.; Edgeworth, J.; Li, X.; Magnuson, C. W.; Velamakanni, A.; Piner, R. D.; Kang, J.; Park, J.; Ruoff, R. S. Oxidation Resistance of Graphene-Coated Cu and Cu/Ni Alloy. *ACS Nano* **2011**, *5*, 1321-1327.
- (12) Li, L. H.; Cervenka, J.; Watanabe, K.; Taniguchi, T.; Chen, Y. Strong Oxidation Resistance of Atomically Thin Boron Nitride Nanosheets. *ACS Nano* **2014**, *8*, 1457-1462.
- (13) Sen, H. S.; Sahin, H.; Peeters, F. M.; Durgun, E. Monolayers of MoS<sub>2</sub> as an oxidation protective nanocoating material. *J. Appl. Phys.* **2014**, *116*, 083508.

- (14) An, X.; Yao, H.; Ma, F.; Lu, Z. The influence of electronic transfer on friction properties of hexagonal boron nitride. *RSC Adv.* **2015**, *5*, 106239-106244.
- (15) Ataca, C.; Ciraci, S. Functionalization of Single-Layer MoS<sub>2</sub> Honeycomb Structures. *J. Phys. Chem. C* **2011**, *115*, 13303-13311.
- (16) Filleter, T.; McChesney, J. L.; Bostwick, A.; Rotenberg, E.; Emtsev, K. V.; Seyller, T.; Horn, K.; Bennewitz, R. Friction and Dissipation in Epitaxial Graphene Films. *Phys. Rev. Lett.* **2009**, *102*, 086102.
- (17) Saito, T.; Honda, F. Chemical contribution to friction behavior of sintered hexagonal boron nitride in water. *Wear* **2000**, *237*, 253-260.
- (18) Spear, J. C.; Ewers, B. W.; Batteas, J. D. 2D-nanomaterials for controlling friction and wear at interfaces. *Nano Today* **2015**, *10*, 301-314.
- (19) Elinski, M. B.; Liu, Z.; Spear, J. C.; Batteas, J. D. 2D or not 2D? The impact of nanoscale roughness and substrate interactions on the tribological properties of graphene and MoS<sub>2</sub>. *J. Phys. D* **2017**, *50*, 103003.
- (20) Romig, A. D.; Dugger, M. T.; McWhorter, P. J. Materials issues in microelectromechanical devices: science, engineering, manufacturability and reliability. *Acta Materialia* **2003**, *51*, 5837-5866.
- (21) Chung, Y. W. *Micro- and Nanoscale Phenomena in Tribology*; Taylor & Francis, 2011.
- (22) Nine, M. J.; Cole, M. A.; Tran, D. N. H.; Losic, D. Graphene: a multipurpose material for protective coatings. *J. Mater. Chem. A* **2015**, *3*, 12580-12602.
- (23) Alem, N.; Erni, R.; Kisielowski, C.; Rossell, M. D.; Gannett, W.; Zettl, A. Atomically thin hexagonal boron nitride probed by ultrahigh-resolution transmission electron microscopy. *Phys. Rev. B* **2009**, *80*, 155425.
- (24) Li, H.; Wu, J.; Yin, Z.; Zhang, H. Preparation and Applications of Mechanically Exfoliated Single-Layer and Multilayer MoS<sub>2</sub> and WSe<sub>2</sub> Nanosheets. *Acc. Chem. Res.* **2014**, *47*, 1067-1075.
- (25) Schumacher, A.; Kruse, N.; Prins, R.; Meyer, E.; Lüthi, R.; Howald, L.; Güntherodt, H. -; Scandella, L. Influence of humidity on friction measurements of supported MoS<sub>2</sub> single layers. *Journal of Vacuum Science & Technology B* **1996**, *14*, 1264-1267.
- (26) Xu, M.; Sun, H.; Shen, C.; Yang, S.; Que, W.; Zhang, Y.; Song, X. Lithium-assisted exfoliation of pristine graphite for few-layer graphene nanosheets. *Nano Research* **2015**, *8*, 801-807.
- (27) Hernandez, Y.; Nicolosi, V.; Lotya, M.; Blighe, F. M.; Sun, Z.; De, S.; McGovern, I. T.; Holland, B.; Byrne, M.; Gun'Ko, Y. K.; Boland, J. J.; Niraj, P.; Duesberg, G.; Krishnamurthy, S.;



Goodhue, R.; Hutchison, J.; Scardaci, V.; Ferrari, A. C.; Coleman, J. N. High-yield production of graphene by liquid-phase exfoliation of graphite. **2008**, *3*, 563.

(28) Zhou, K.; Mao, N.; Wang, H.; Peng, Y.; Zhang, H. A Mixed-Solvent Strategy for Efficient Exfoliation of Inorganic Graphene Analogues. *Angewandte Chemie International Edition* **2011**, *50*, 10839-10842.

(29) Song, L.; Ci, L.; Lu, H.; Sorokin, P. B.; Jin, C.; Ni, J.; Kvashnin, A. G.; Kvashnin, D. G.; Lou, J.; Yakobson, B. I.; Ajayan, P. M. Large Scale Growth and Characterization of Atomic Hexagonal Boron Nitride Layers. *Nano Lett.* **2010**, *10*, 3209-3215.

(30) Zhan, Y.; Liu, Z.; Najmaei, S.; Ajayan, P. M.; Lou, J. Large-Area Vapor-Phase Growth and Characterization of MoS<sub>2</sub> Atomic Layers on a SiO<sub>2</sub> Substrate. *Small* **2012**, *8*, 966-971.

(31) Kim, K.; Lee, H.; Lee, C.; Lee, S.; Jang, H.; Ahn, J.; Kim, J.; Lee, H. Chemical Vapor Deposition-Grown Graphene: The Thinnest Solid Lubricant. *ACS Nano* **2011**, *5*, 5107-5114.

(32) Li, X.; Zhu, Y.; Cai, W.; Borysiak, M.; Han, B.; Chen, D.; Piner, R. D.; Colombo, L.; Ruoff, R. S. Transfer of Large-Area Graphene Films for High-Performance Transparent Conductive Electrodes. *Nano Lett.* **2009**, *9*, 4359-4363.

(33) Yu, Y.; Li, C.; Liu, Y.; Su, L.; Zhang, Y.; Cao, L. Controlled Scalable Synthesis of Uniform, High-Quality Monolayer and Few-layer MoS<sub>2</sub> Films. *Scientific Reports* **2013**, *3*, 1866.

(34) Virojanadara, C.; Syvajarvi, M.; Yakimova, R.; Johansson, L. I.; Zakharov, A. A.; Balasubramanian, T. Homogeneous large-area graphene layer growth on 6H-SiC (0001). *Phys.Rev.B* **2008**, *78*, 245403.

(35) Dumcenco, D.; Ovchinnikov, D.; Marinov, K.; Lazić, P.; Gibertini, M.; Marzari, N.; Sanchez, O. L.; Kung, Y.; Krasnozhan, D.; Chen, M.; Bertolazzi, S.; Gillet, P.; Fontcuberta, i. M.; Radenovic, A.; Kis, A. Large-Area Epitaxial Monolayer MoS<sub>2</sub>. *ACS Nano* **2015**, *9*, 4611-4620.

(36) Han, G. H.; Chae, S. J.; Kim, E. S.; Gunes, F.; Lee, I. H.; Lee, S. W.; Lee, S. Y.; Lim, S. C.; Jeong, H. K.; Jeong, M. S.; Lee, Y. H. Laser Thinning for Monolayer Graphene Formation: Heat Sink and Interference Effect. *ACS Nano* **2011**, *5*, 263-268.

(37) Castellanos-Gomez, A.; Barkelid, M.; Goossens, A. M.; Calado, V. E.; van, d. Z.; Steele, G. A. Laser-Thinning of MoS<sub>2</sub>: On Demand Generation of a Single-Layer Semiconductor. *Nano Lett.* **2012**, *12*, 3187-3192.

(38) Liu, Y.; Nan, H.; Wu, X.; Pan, W.; Wang, W.; Bai, J.; Zhao, W.; Sun, L.; Wang, X.; Ni, Z. Layer-by-Layer Thinning of MoS<sub>2</sub> by Plasma. *ACS Nano* **2013**, *7*, 4202-4209.

(39) Lu, X.; Utama, M. I. B.; Zhang, J.; Zhao, Y.; Xiong, Q. Layer-by-layer thinning of MoS<sub>2</sub> by thermal annealing. *Nanoscale* **2013**, *5*, 8904-8908.

- (40) Helveg, S.; Lauritsen, J. V.; Lægsgaard, E.; Stensgaard, I.; Nørskov, J. K.; Clausen, B. S.; Topsøe, H.; Besenbacher, F. Atomic-Scale Structure of Single-Layer MoS<sub>2</sub> Nanoclusters. *Phys. Rev. Lett.* **2000**, *84*, 951-954.
- (41) Garlow, J. A.; Barrett, L. K.; Wu, L.; Kisslinger, K.; Zhu, Y.; Pulecio, J. F. Large-Area Growth of Turbostratic Graphene on Ni (111) via Physical Vapor Deposition. **2016**, *6*, 19804.
- (42) Penkov, O.; Kim, H.; Kim, H.; Kim, D. Tribology of graphene: A review. *International Journal of Precision Engineering and Manufacturing* **2014**, *15*, 577-585.
- (43) Zandiatashbar, A.; Lee, G.; An, S. J.; Lee, S.; Mathew, N.; Terrones, M.; Hayashi, T.; Picu, C. R.; Hone, J.; Koratkar, N. Effect of defects on the intrinsic strength and stiffness of graphene. **2014**, *5*, 3186.
- (44) GÃmez-Navarro, C.; Burghard, M.; Kern, K. Elastic Properties of Chemically Derived Single Graphene Sheets. *Nano Lett.* **2008**, *8*, 2045-2049.
- (45) Zhang, P.; Ma, L.; Fan, F.; Zeng, Z.; Peng, C.; Loya, P. E.; Liu, Z.; Gong, Y.; Zhang, J.; Zhang, X.; Ajayan, P. M.; Zhu, T.; Lou, J. Fracture toughness of graphene. **2014**, *5*, 3782.
- (46) Santos, E. J. G.; Riikonen, S.; Sanchez-Portal, D.; Ayuela, A. Magnetism of Single Vacancies in Rippled Graphene. *J. Phys. Chem. C* **2012**, *116*, 7602-7606.
- (47) Shekhawat, A.; Ritchie, R. O. Toughness and strength of nanocrystalline graphene. **2016**, *7*, 10546.
- (48) Mortazavi, B.; Cuniberti, G. Mechanical properties of polycrystalline boron-nitride nanosheets. *RSC Adv.* **2014**, *4*, 19137-19143.
- (49) Ding, N.; Wu, C. L.; Li, H. The effect of grain boundaries on the mechanical properties and failure behavior of hexagonal boron nitride sheets. *Phys.Chem.Chem.Phys.* **2014**, *16*, 23716-23722.
- (50) Bosak, A.; Serrano, J.; Krisch, M.; Watanabe, K.; Taniguchi, T.; Kanda, H. Elasticity of hexagonal boron nitride: Inelastic x-ray scattering measurements. *Phys. Rev. B* **2006**, *73*, 041402.
- (51) Wu, J.; Wang, B.; Wei, Y.; Yang, R.; Dresselhaus, M. Mechanics and Mechanically Tunable Band Gap in Single-Layer Hexagonal Boron-Nitride. *Materials Research Letters* **2013**, *1*, 200-206.
- (52) Peelaers, H.; Van, d. W. Elastic Constants and Pressure-Induced Effects in MoS<sub>2</sub>. *J. Phys. Chem. C* **2014**, *118*, 12073-12076.
- (53) Jiang, J.; Qi, Z.; Park, H. S.; Rabczuk, T. Elastic bending modulus of single-layer molybdenum disulfide (MoS<sub>2</sub>): finite thickness effect. *Nanotechnology* **2013**, *24*, 435705.

- (54) Bosak, A.; Krisch, M.; Mohr, M.; Maultzsch, J.; Thomsen, C. Elasticity of single-crystalline graphite: Inelastic x-ray scattering study. *Phys. Rev. B* **2007**, *75*, 153408.
- (55) Lu, Q.; Arroyo, M.; Huang, R. Elastic bending modulus of monolayer graphene. *J. Phys. D* **2009**, *42*, 102002.
- (56) Lee, B.; Lee, D.; Lee, J. H.; Ryu, H. J.; Hong, S. H. Enhancement of toughness and wear resistance in boron nitride nanoplatelet (BNNP) reinforced Si<sub>3</sub>N<sub>4</sub> nanocomposites. **2016**, *6*, 27609.
- (57) Bansal, N. P.; Hurst, J. B.; Choi, S. R. Boron Nitride Nanotubes-Reinforced Glass Composites. *J Am Ceram Soc* **2006**, *89*, 388-390.
- (58) Wang, W.; Bi, J.; Wang, S.; Sun, K.; Du, M.; Long, N.; Bai, Y. Microstructure and mechanical properties of alumina ceramics reinforced by boron nitride nanotubes. *Journal of the European Ceramic Society* **2011**, *31*, 2277-2284.
- (59) Wang, W.; Bi, J.; Sun, K.; Du, M.; Long, N.; Bai, Y. Thermal Shock Resistance Behavior of Alumina Ceramics Incorporated with Boron Nitride Nanotubes. *J Am Ceram Soc* **2011**, *94*, 2304-2307.
- (60) Chen, Y.; Bi, J.; Wang, W.; Zhao, Y.; You, G.; Yin, C.; Bai, Y. Toughening in boron nitride nanotubes/silicon nitride composites. *Materials Science and Engineering: A* **2014**, *590*, 16-20.
- (61) Cho, D.; Kim, J.; Kwon, S.; Lee, C.; Lee, Y. Evaluation of hexagonal boron nitride nano-sheets as a lubricant additive in water. *Wear* **2013**, *302*, 981-986.
- (62) Watanabe, S.; Miyake, S.; Murakawa, M. Tribological properties of cubic, amorphous and hexagonal boron nitride films. *Surface and Coatings Technology* **1991**, *49*, 406-410.
- (63) Buck, V. Morphological properties of sputtered MoS<sub>2</sub> films. *Wear* **1983**, *91*, 281-288.
- (64) Wahl, K. J.; Singer, I. L. Quantification of a lubricant transfer process that enhances the sliding life of a MoS<sub>2</sub> coating. *Tribology Letters* **1995**, *1*, 59-66.
- (65) Donnet, C.; Le Mogne, T.; Martin, J. M. Superlow friction of oxygen-free MoS<sub>2</sub> coatings in ultrahigh vacuum. *Surface and Coatings Technology* **1993**, *62*, 406-411.
- (66) Martin, J. M.; Pascal, H.; Donnet, C.; Le Mogne, T.; Loubet, J. L.; Epicier, T. Superlubricity of MoS<sub>2</sub>: crystal orientation mechanisms. *Surface and Coatings Technology* **1994**, *68*, 427-432.
- (67) Singer, I. L.; Fayeulle, S.; Ehni, P. D. Wear behavior of triode-sputtered MoS<sub>2</sub> coatings in dry sliding contact with steel and ceramics. *Wear* **1996**, *195*, 7-20.
- (68) Khare, H. S.; Burriss, D. L. The Effects of Environmental Water and Oxygen on the Temperature-Dependent Friction of Sputtered Molybdenum Disulfide. *Tribology Letters* **2013**, *52*, 485-493.

- (69) Vasić, B.; Matković, A.; Ralević, U.; Belić, M.; Gajić, R. Nanoscale wear of graphene and wear protection by graphene. *Carbon* **2017**, *120*, 137-144.
- (70) Shin, Y. J.; Stromberg, R.; Nay, R.; Huang, H.; Wee, A. T. S.; Yang, H.; Bhatia, C. S. Frictional characteristics of exfoliated and epitaxial graphene. *Carbon* **2011**, *49*, 4070-4073.
- (71) Qi, Y.; Liu, J.; Zhang, J.; Dong, Y.; Li, Q. Wear Resistance Limited by Step Edge Failure: The Rise and Fall of Graphene as an Atomically Thin Lubricating Material. *ACS Appl. Mater. Interfaces* **2017**, *9*, 1099-1106.
- (72) Marchetto, D.; Held, C.; Hausen, F.; Wählich, F.; Dienwiebel, M.; Bennewitz, R. Friction and Wear on Single-Layer Epitaxial Graphene in Multi-Asperity Contacts. *Tribology Letters* **2012**, *48*, 77-82.
- (73) Won, M.; Penkov, O. V.; Kim, D. Durability and degradation mechanism of graphene coatings deposited on Cu substrates under dry contact sliding. *Carbon* **2013**, *54*, 472-481.
- (74) Berman, D.; Erdemir, A.; Sumant, A. V. Few layer graphene to reduce wear and friction on sliding steel surfaces. *Carbon* **2013**, *54*, 454-459.
- (75) Berman, D.; Deshmukh, S. A.; Sankaranarayanan, S. K. R. S.; Erdemir, A.; Sumant, A. V. Extraordinary Macroscale Wear Resistance of One Atom Thick Graphene Layer. *Advanced Functional Materials* **2014**, *24*, 6640-6646.
- (76) Wählich, F.; Hoth, J.; Held, C.; Seyller, T.; Bennewitz, R. Friction and atomic-layer-scale wear of graphitic lubricants on SiC (0001) in dry sliding. *Wear* **2013**, *300*, 78-81.
- (77) Barboza, A. P. M.; Chacham, H.; Oliveira, C. K.; Fernandes, T. F. D.; Ferreira, E. H. M.; Archanjo, B. S.; Batista, R. J. C.; de Oliveira, A. B.; Neves, B. R. A. Dynamic Negative Compressibility of Few-Layer Graphene, h-BN, and MoS<sub>2</sub>. *Nano Lett.* **2012**, *12*, 2313-2317.
- (78) Lin, L.; Kim, D.; Kim, W.; Jun, S. Friction and wear characteristics of multi-layer graphene films investigated by atomic force microscopy. *Surface and Coatings Technology* **2011**, *205*, 4864-4869.
- (79) Klemenz, A.; Pastewka, L.; Balakrishna, S. G.; Caron, A.; Bennewitz, R.; Moseler, M. Atomic Scale Mechanisms of Friction Reduction and Wear Protection by Graphene. *Nano Lett.* **2014**, *14*, 7145-7152.
- (80) Li, X.; Yin, J.; Zhou, J.; Guo, W. Large area hexagonal boron nitride monolayer as efficient atomically thick insulating coating against friction and oxidation. *Nanotechnology* **2014**, *25*, 105701.
- (81) Tran Khac, B. C.; Chung, K. Quantitative assessment of contact and non-contact lateral force calibration methods for atomic force microscopy. *Ultramicroscopy* **2016**, *161*, 41-50.

- (82) Deng, Z.; Klimov, N. N.; Solares, S. D.; Li, T.; Xu, H.; Cannara, R. J. Nanoscale Interfacial Friction and Adhesion on Supported versus Suspended Monolayer and Multilayer Graphene. *Langmuir* **2013**, *29*, 235-243.
- (83) Lee, C.; Li, Q.; Kalb, W.; Liu, X.; Berger, H.; Carpick, R. W.; Hone, J. Frictional Characteristics of Atomically Thin Sheets. *Science* **2010**, *328*, 76-80.
- (84) Fang, L.; Liu, D.; Guo, Y.; Liao, Z.; Luo, J.; Wen, S. Thickness dependent friction on few-layer MoS<sub>2</sub>, WS<sub>2</sub>, and WSe<sub>2</sub>. *Nanotechnology* **2017**, *28*, 245703.
- (85) Li, Q.; Lee, C.; Carpick, R. W.; Hone, J. Substrate effect on thickness-dependent friction on graphene. *physica status solidi (b)* **2010**, *247*, 2909-2914.
- (86) Cho, D.; Wang, L.; Kim, J.; Lee, G.; Kim, E. S.; Lee, S.; Lee, S. Y.; Hone, J.; Lee, C. Effect of surface morphology on friction of graphene on various substrates. *Nanoscale* **2013**, *5*, 3063-3069.
- (87) Paolicelli, G.; Tripathi, M.; Corradini, V.; Candini, A.; Valeri, S. Nanoscale frictional behavior of graphene on SiO<sub>2</sub> and Ni (111) substrates. *Nanotechnology* **2015**, *26*, 055703.
- (88) Choi, J. S.; Kim, J.; Byun, I.; Lee, D. H.; Lee, M. J.; Park, B. H.; Lee, C.; Yoon, D.; Cheong, H.; Lee, K. H.; Son, Y.; Park, J. Y.; Salmeron, M. Friction Anisotropy-Driven Domain Imaging on Exfoliated Monolayer Graphene. *Science* **2011**, *333*, 607-610.
- (89) Tran Khac, B. C.; Jeon, K.; Choi, S. T.; Kim, Y. S.; DelRio, F. W.; Chung, K. Laser-Induced Particle Adsorption on Atomically Thin MoS<sub>2</sub>. *ACS Appl. Mater. Interfaces* **2016**, *8*, 2974-2984.
- (90) Kwon, S.; Ko, J.; Jeon, K.; Kim, Y.; Park, J. Y. Enhanced Nanoscale Friction on Fluorinated Graphene. *Nano Lett.* **2012**, *12*, 6043-6048.
- (91) Li, Q.; Liu, X.; Kim, S.; Shenoy, V. B.; Sheehan, P. E.; Robinson, J. T.; Carpick, R. W. Fluorination of Graphene Enhances Friction Due to Increased Corrugation. *Nano Lett.* **2014**, *14*, 5212-5217.
- (92) Byun, I. S.; Yoon, D.; Choi, J. S.; Hwang, I.; Lee, D. H.; Lee, M. J.; Kawai, T.; Son, Y. W.; Jia, Q.; Cheong, H.; Park, B. H. Nanoscale lithography on monolayer graphene using hydrogenation and oxidation. *ACS Nano* **2011**, *5*, 6417-6424.
- (93) Dong, Y.; Wu, X.; Martini, A. Atomic roughness enhanced friction on hydrogenated graphene. *Nanotechnology* **2013**, *24*, 375701.
- (94) Fessler, G.; Eren, B.; Gysin, U.; Glatzel, T.; Meyer, E. Friction force microscopy studies on SiO<sub>2</sub> supported pristine and hydrogenated graphene. *Appl. Phys. Lett.* **2014**, *104*, 041910.
- (95) Ko, J.; Kwon, S.; Byun, I.; Choi, J.; Park, B.; Kim, Y.; Park, J. Nanotribological Properties of Fluorinated, Hydrogenated, and Oxidized Graphenes. *Tribology Letters* **2013**, *50*, 137-144.

- (96) Gorbachev, R. V.; Riaz, I.; Nair, R. R.; Jalil, R.; Britnell, L.; Belle, B. D.; Hill, E. W.; Novoselov, K. S.; Watanabe, K.; Taniguchi, T.; Geim, A. K.; Blake, P. Hunting for Monolayer Boron Nitride: Optical and Raman Signatures. *Small* **2011**, *7*, 465-468.
- (97) Li, H.; Zhang, Q.; Yap, C. C. R.; Tay, B. K.; Edwin, T. H. T.; Olivier, A.; Baillargeat, D. From Bulk to Monolayer MoS<sub>2</sub>: Evolution of Raman Scattering. *Advanced Functional Materials* **2012**, *22*, 1385-1390.
- (98) Ferrari, A. C.; Meyer, J. C.; Scardaci, V.; Casiraghi, C.; Lazzeri, M.; Mauri, F.; Piscanec, S.; Jiang, D.; Novoselov, K. S.; Roth, S.; Geim, A. K. Raman Spectrum of Graphene and Graphene Layers. *Phys. Rev. Lett.* **2006**, *97*, 187401.
- (99) Goossens, A. M.; Calado, V. E.; Barreiro, A.; Watanabe, K.; Taniguchi, T.; Vandersypen, L. M. K. Mechanical cleaning of graphene. *Appl. Phys. Lett.* **2012**, *100*, 073110.
- (100) Tocci, G.; Joly, L.; Michaelides, A. Friction of Water on Graphene and Hexagonal Boron Nitride from Ab Initio Methods: Very Different Slippage Despite Very Similar Interface Structures. *Nano Lett.* **2014**, *14*, 6872-6877.
- (101) Luan, B.; Zhou, R. Wettability and friction of water on a MoS<sub>2</sub> nanosheet. *Appl. Phys. Lett.* **2016**, *108*, 131601.
- (102) Hao, R.; Tedstone, A. A.; Lewis, D. J.; Warrens, C. P.; West, K. R.; Howard, P.; Gaemers, S.; Dillon, S. J.; Oâ€™Brien, P. Property Self-Optimization During Wear of MoS<sub>2</sub>. *ACS Appl. Mater. Interfaces* **2017**, *9*, 1953-1958.
- (103) Najmaei, S.; Liu, Z.; Ajayan, P. M.; Lou, J. Thermal effects on the characteristic Raman spectrum of molybdenum disulfide (MoS<sub>2</sub>) of varying thicknesses. *Appl. Phys. Lett.* **2012**, *100*, 013106.
- (104) Hutter, J. L.; Bechhoefer, J. Calibration of atomic-force microscope tips. *Rev. Sci. Instrum.* **1993**, *64*, 1868-1873.
- (105) Chung, K. H.; Reitsma, M. G. Note: Lateral force microscope calibration using multiple location pivot loading of rectangular cantilevers. *Rev. Sci. Instrum.* **2010**, *81*, 026104.
- (106) Derjaguin, B. V.; Muller, V. M.; Toporov, Y. P. Effect of contact deformations on the adhesion of particles. *J. Colloid Interface Sci.* **1975**, *53*, 314-326.
- (107) Vidano, R. P.; Fischbach, D. B.; Willis, L. J.; Loehr, T. M. Observation of Raman band shifting with excitation wavelength for carbons and graphites. *Solid State Communications* **1981**, *39*, 341-344.
- (108) Ollivier, B.; Matthews, A. Adhesion of diamond-like carbon films on polymers: an assessment of the validity of the scratch test technique applied to flexible substrates. *J. Adhes. Sci. Technol.* **1994**, *8*, 651-662.

- (109) Morozov, O.; Postnikov, A. Mechanical strength study of SiO<sub>2</sub> isolation blocks merged in silicon substrate. *J Micromech Microengineering* **2015**, *25*, 015014.
- (110) Singh, S. K.; Neek-Amal, M.; Costamagna, S.; Peeters, F. M. Thermomechanical properties of a single hexagonal boron nitride sheet. *Phys. Rev. B* **2013**, *87*, 184106.
- (111) Ahlberg, P.; Johansson, F. O. L.; Zhang, Z.; Jansson, U.; Zhang, S.; Lindblad, A.; Nyberg, T. Defect formation in graphene during low-energy ion bombardment. *APL Materials* **2016**, *4*, 046104.
- (112) Slotman, G. J.; Fasolino, A. Structure, stability and defects of single layer hexagonal BN in comparison to graphene. *Journal of Physics: Condensed Matter* **2013**, *25*, 045009.
- (113) Jin, C.; Lin, F.; Suenaga, K.; Iijima, S. Fabrication of a Freestanding Boron Nitride Single Layer and Its Defect Assignments. *Phys. Rev. Lett.* **2009**, *102*, 195505.
- (114) Nayak, A. P.; Pandey, T.; Voiry, D.; Liu, J.; Moran, S. T.; Sharma, A.; Tan, C.; Chen, C.; Li, L.; Chhowalla, M.; Lin, J.; Singh, A. K.; Akinwande, D. Pressure-Dependent Optical and Vibrational Properties of Monolayer Molybdenum Disulfide. *Nano Lett.* **2015**, *15*, 346-353.
- (115) Nan, H.; Wang, Z.; Wang, W.; Liang, Z.; Lu, Y.; Chen, Q.; He, D.; Tan, P.; Miao, F.; Wang, X.; Wang, J.; Ni, Z. Strong Photoluminescence Enhancement of MoS<sub>2</sub> through Defect Engineering and Oxygen Bonding. *ACS Nano* **2014**, *8*, 5738-5745.
- (116) Windom, B.; Sawyer, W. G.; Hahn, D. A Raman Spectroscopic Study of MoS<sub>2</sub> and MoO<sub>3</sub>: Applications to Tribological Systems. *Tribology Letters* **2011**, *42*, 301-310.
- (117) Kim, Y.; Jhon, Y. I.; Park, J.; Kim, C.; Lee, S.; Jhon, Y. M. Plasma functionalization for cyclic transition between neutral and charged excitons in monolayer MoS<sub>2</sub>. *Scientific Reports* **2016**, *6*, 21405.
- (118) Childres, I.; Jauregui, L. A.; Chen, Y. P. Raman spectra and electron-phonon coupling in disordered graphene with gate-tunable doping. *J. Appl. Phys.* **2014**, *116*, 233101.
- (119) Anonymous Raman Spectrum of Graphite. *J. Chem. Phys.* **1970**, *53*, 1126-1130.
- (120) Lucchese, M. M.; Stavale, F.; Ferreira, E. H. M.; Vilani, C.; Moutinho, M. V. O.; Capaz, R. B.; Achete, C. A.; Jorio, A. Quantifying ion-induced defects and Raman relaxation length in graphene. *Carbon* **2010**, *48*, 1592-1597.
- (121) Chen, J.; Cullen, W. G.; Jang, C.; Fuhrer, M. S.; Williams, E. D. Defect Scattering in Graphene. *Phys. Rev. Lett.* **2009**, *102*, 236805.
- (122) Cancado, L. G.; Jorio, A.; Ferreira, E. H. M.; Stavale, F.; Achete, C. A.; Capaz, R. B.; Moutinho, M. V. O.; Lombardo, A.; Kulmala, T. S.; Ferrari, A. C. Quantifying Defects in

Graphene via Raman Spectroscopy at Different Excitation Energies. *Nano Lett.* **2011**, *11*, 3190-3196.

(123) Proctor, J. E.; Gregoryanz, E.; Novoselov, K. S.; Lotya, M.; Coleman, J. N.; Halsall, M. P. High-pressure Raman spectroscopy of graphene. *Phys. Rev. B* **2009**, *80*, 073408.

(124) Ferrari, A. C.; Robertson, J. Interpretation of Raman spectra of disordered and amorphous carbon. *Phys. Rev. B* **2000**, *61*, 14095-14107.

(125) Zhang, Y.; Liu, F. Maximum asymmetry in strain induced mechanical instability of graphene: Compression versus tension. *Appl. Phys. Lett.* **2011**, *99*, 241908.

(126) Peng, Q.; De, S. Outstanding mechanical properties of monolayer MoS<sub>2</sub> and its application in elastic energy storage. *Phys.Chem.Chem.Phys.* **2013**, *15*, 19427-19437.

(127) Björkman, T.; Gulans, A.; Krashennnikov, A. V.; Nieminen, R. M. van der Waals Bonding in Layered Compounds from Advanced Density-Functional First-Principles Calculations. *Phys. Rev. Lett.* **2012**, *108*, 235502.

(128) Li, J.; Luo, J. Nonlinear Frictional Energy Dissipation between Silica-Adsorbed Surfactant Micelles. *J. Phys. Chem. Lett.* **2017**, *8*, 2258-2262.

(129) Kim, G.; Jang, A.; Jeong, H. Y.; Lee, Z.; Kang, D. J.; Shin, H. S. Growth of High-Crystalline, Single-Layer Hexagonal Boron Nitride on Recyclable Platinum Foil. *Nano Lett.* **2013**, *13*, 1834-1839.

(130) Shearer, C. J.; Slattery, A. D.; Stapleton, A. J.; Shapter, J. G.; Gibson, C. T. Accurate thickness measurement of graphene. *Nanotechnology* **2016**, *27*, 125704.

(131) Sundararajan, S.; Bhushan, B. Topography-induced contributions to friction forces measured using an atomic force/friction force microscope. *J. Appl. Phys.* **2000**, *88*, 4825-4831.

(132) Holscher, H.; Ebeling, D.; Schwarz, U. D. Friction at Atomic-Scale Surface Steps: Experiment and Theory. *Phys. Rev. Lett.* **2008**, *101*, 246105.

(133) Li, P.; You, Z.; Cui, T. Molybdenum disulfide dc contact MEMS shunt switch. *J Micromech Microengineering* **2013**, *23*, 045026.

(134) Maugis, D. Adhesion of spheres: The JKR-DMT transition using a dugdale model. *J. Colloid Interface Sci.* **1992**, *150*, 243-269.

(135) Carpick, R. W.; Ogletree, D. F.; Salmeron, M. A General Equation for Fitting Contact Area and Friction vs Load Measurements. *Journal of Colloid and Interface Science* **1999**, *211*, 395-400.

(136) Carpick, R. W.; Salmeron, M. Scratching the Surface: Fundamental Investigations of Tribology with Atomic Force Microscopy. *Chem. Rev.* **1997**, *97*, 1163-1194.



- (137) Schwarz, U. D.; Zwörner, O.; Köster, P.; Wiesendanger, R. Quantitative analysis of the frictional properties of solid materials at low loads. I. Carbon compounds. *Phys.Rev.B* **1997**, *56*, 6987-6996.
- (138) Schwarz, U. D. A generalized analytical model for the elastic deformation of an adhesive contact between a sphere and a flat surface. *Journal of Colloid and Interface Science* **2003**, *261*, 99-106.
- (139) Mohr, M.; Caron, A.; Herbeck-Engel, P.; Bennewitz, R.; Gluche, P.; Bruhne, K.; Fecht, H. Young's modulus, fracture strength, and Poisson's ratio of nanocrystalline diamond films. *J. Appl. Phys.* **2014**, *116*, 124308.
- (140) Lebedev, A. V.; Lebedeva, I. V.; Knizhnik, A. A.; Popov, A. M. Interlayer interaction and related properties of bilayer hexagonal boron nitride: ab initio study. *RSC Adv.* **2016**, *6*, 6423-6435.
- (141) Hajgató, B.; Güryel, S.; Dauphin, Y.; Blairon, J.; Miltner, H. E.; Van Lier, G.; De Proft, F.; Geerlings, P. Out-of-plane shear and out-of plane Young's modulus of double-layer graphene. *Chemical Physics Letters* **2013**, *564*, 37-40.
- (142) Onodera, T.; Morita, Y.; Nagumo, R.; Miura, R.; Suzuki, A.; Tsuboi, H.; Hatakeyama, N.; Endou, A.; Takaba, H.; Dassenoy, F.; Minfray, C.; Joly-Pottuz, L.; Kubo, M.; Martin, J.; Miyamoto, A. A Computational Chemistry Study on Friction of h-MoS<sub>2</sub>. Part II. Friction Anisotropy. *J Phys Chem B* **2010**, *114*, 15832-15838.
- (143) Singer, I. L.; Bolster, R. N.; Wegand, J.; Fayeulle, S.; Stupp, B. C. Hertzian stress contribution to low friction behavior of thin MoS<sub>2</sub> coatings. *Appl. Phys. Lett.* **1990**, *57*, 995-997.
- (144) Langlade, C.; Fayeulle, S.; Olier, R. New insights into adhesion and lubricating properties of graphite-based transfer films. *Wear* **1994**, *172*, 85-92.
- (145) Riedo, E.; Gnecco, E.; Bennewitz, R.; Meyer, E.; Brune, H. Interaction Potential and Hopping Dynamics Governing Sliding Friction. *Phys. Rev. Lett.* **2003**, *91*, 084502.
- (146) Chen, J.; Ratera, I.; Park, J. Y.; Salmeron, M. Velocity Dependence of Friction and Hydrogen Bonding Effects. *Phys. Rev. Lett.* **2006**, *96*, 236102.
- (147) Gnecco, E.; Bennewitz, R.; Gyalog, T.; Loppacher, C.; Bammerlin, M.; Meyer, E.; Güntherodt, H. Velocity Dependence of Atomic Friction. *Phys. Rev. Lett.* **2000**, *84*, 1172-1175.
- (148) Li, Q.; Dong, Y.; Perez, D.; Martini, A.; Carpick, R. W. Speed Dependence of Atomic Stick-Slip Friction in Optimally Matched Experiments and Molecular Dynamics Simulations. *Phys. Rev. Lett.* **2011**, *106*, 126101.
- (149) Liu, X.; Ye, Z.; Dong, Y.; Egberts, P.; Carpick, R. W.; Martini, A. Dynamics of Atomic Stick-Slip Friction Examined with Atomic Force Microscopy and Atomistic Simulations at Overlapping Speeds. *Phys. Rev. Lett.* **2015**, *114*, 146102.

- (150) Jansen, L.; Holscher, H.; Fuchs, H.; Schirmeisen, A. Temperature Dependence of Atomic-Scale Stick-Slip Friction. *Phys. Rev. Lett.* **2010**, *104*, 256101.
- (151) Mo, Y.; Turner, K. T.; Szlufarska, I. Friction laws at the nanoscale. *Nature* **2009**, *457*, 1116-1119.
- (152) Riedo, E.; Levy, F.; Brune, H. Kinetics of Capillary Condensation in Nanoscopic Sliding Friction. *Phys. Rev. Lett.* **2002**, *88*, 185505.
- (153) Li, X.; Qiu, H.; Liu, X.; Yin, J.; Guo, W. Wettability of Supported Monolayer Hexagonal Boron Nitride in Air. *Advanced Functional Materials* **2017**, *27*, 1603181.
- (154) Gaur, A. P. S.; Sahoo, S.; Ahmadi, M.; Dash, S. P.; Guinel, M. J. -.; Katiyar, R. S. Surface Energy Engineering for Tunable Wettability through Controlled Synthesis of MoS<sub>2</sub>. *Nano Lett.* **2014**, *14*, 4314-4321.
- (155) Raj, R.; Maroo, S. C.; Wang, E. N. Wettability of Graphene. *Nano Lett.* **2013**, *13*, 1509-1515.
- (156) Sandoz-Rosado, E. J.; Tertuliano, O. A.; Terrell, E. J. An atomistic study of the abrasive wear and failure of graphene sheets when used as a solid lubricant and a comparison to diamond-like-carbon coatings. *Carbon* **2012**, *50*, 4078-4084.
- (157) Yen, B. K.; Schwickert, B. E.; Toney, M. F. Origin of low-friction behavior in graphite investigated by surface x-ray diffraction. *Appl. Phys. Lett.* **2004**, *84*, 4702-4704.
- (158) Zhao, X.; Perry, S. S. The Role of Water in Modifying Friction within MoS<sub>2</sub> Sliding Interfaces. *ACS Appl. Mater. Interfaces* **2010**, *2*, 1444-1448.
- (159) Levita, G.; Righi, M. C. Effects of Water Intercalation and Tribochemistry on MoS<sub>2</sub> Lubricity: An Ab Initio Molecular Dynamics Investigation. *ChemPhysChem* **2017**, *18*, 1475-1480.
- (160) Lee, M. J.; Choi, J. S.; Kim, J.; Byun, I.; Lee, D. H.; Ryu, S.; Lee, C.; Park, B. H. Characteristics and effects of diffused water between graphene and a SiO<sub>2</sub> substrate. *Nano Research* **2012**, *5*, 710-717.
- (161) Jinkins, K.; Camacho, J.; Farina, L.; Wu, Y. Examination of humidity effects on measured thickness and interfacial phenomena of exfoliated graphene on silicon dioxide via amplitude modulation atomic force microscopy. *Appl. Phys. Lett.* **2015**, *107*, 243107.
- (162) Song, J.; Li, Q.; Wang, X.; Li, J.; Zhang, S.; Kjems, J.; Besenbacher, F.; Dong, M. Evidence of Stranski-Krastanov growth at the initial stage of atmospheric water condensation. **2014**, *5*, 4837.
- (163) Yoon, D.; Son, Y.; Cheong, H. Negative Thermal Expansion Coefficient of Graphene Measured by Raman Spectroscopy. *Nano Lett.* **2011**, *11*, 3227-3231.